

# POLITECNICO DI TORINO

Facoltà di Ingegneria

Corso di Laurea Magistrale in  
Ingegneria Energetica e Nucleare



Tesi di Laurea Magistrale

**Experimental and numerical analysis of thermochemical cycles  
using cerium oxides and iron oxides**

**Relatori**

Dr. Davide Papurello

Dr. Domenico Ferrero

Prof. Massimo Santarelli

**Candidato**

Francesco Orsini

4 Dicembre 2020



*A mio padre,  
la cui mano invisibile continua  
ogni giorno a guidarmi,  
e a mia madre,  
il mio più luminoso punto di riferimento.  
Alla mia famiglia,  
e a tutti coloro che mi sono stati vicino  
in questo percorso fatto di sacrifici,  
ma anche di grandi soddisfazioni.*



*To my father,  
whose invisible hand continues  
to guide me every day,  
and to my mother,  
my brightest point of reference.*

*To my family,  
and to all those who have been close to me  
in this path made of sacrifices,  
but also of great satisfactions.*



# Contents

<b>Nomenclature</b>	<b>9</b>
<b>List of Figures</b>	<b>13</b>
<b>List of Tables</b>	<b>17</b>
<b>Abstract</b>	<b>18</b>
<b>0 Preliminaries</b>	<b>19</b>
0.1 Motivation and objectives . . . . .	19
0.2 Structure of the work and how to read it . . . . .	19
<b>1 Introduction</b>	<b>20</b>
1.1 Climate change and decarbonization. The role of hydrogen in the energy framework	20
<b>2 Concentrating solar power (CSP) technologies</b>	<b>26</b>
2.1 Receivers for CSP . . . . .	27
2.2 Fundamentals on CSP technologies . . . . .	29
2.2.1 Thermodynamic generalities . . . . .	29
2.2.2 Thermodynamic and optical limits on concentration . . . . .	31
2.2.3 Thermal and optical losses . . . . .	34
2.3 Typologies of CSP facilities . . . . .	37
<b>3 Solar thermochemical processes for hydrogen and syngas production</b>	<b>41</b>
3.1 A general overview . . . . .	41
3.2 CSP-fed solar reactors for solar fuels production through thermochemical cycles . . .	46
<b>4 Literature review on thermochemical cycles</b>	<b>50</b>
4.1 Cerium oxides based thermochemical cycles . . . . .	50
4.2 Iron oxides based thermochemical cycles . . . . .	64
<b>5 Experimental activity</b>	<b>72</b>
5.1 Test bench description . . . . .	72
5.1.1 Thermogravimetric analysis (TGA) . . . . .	72
5.2 Experimental procedure and results . . . . .	73
5.2.1 TGA on cerium oxides . . . . .	73
5.2.2 TGA on iron oxides . . . . .	83
5.2.2.1 First part. Thermal reduction and air-based oxidation cycle . . . . .	83
5.2.2.2 Second part. H <sub>2</sub> -aided reduction and CO <sub>2</sub> -based oxidation cycle . . . . .	88
5.2.2.3 Third part. <i>Mixed</i> equivalent cycle . . . . .	93
<b>6 Numerical modeling</b>	<b>95</b>
6.1 Kinetic analysis and data-fitting . . . . .	95
6.2 Geometry and materials . . . . .	97
6.3 Physics . . . . .	98
6.3.1 Models and governing equations . . . . .	98
6.3.2 Boundary and initial conditions . . . . .	101
6.4 Mesh and computational optimization procedures . . . . .	102

6.5	Results and discussion . . . . .	103
<b>7</b>	<b>Conclusions</b>	<b>107</b>
7.1	Summarizing . . . . .	107
7.2	Possible further development of the work . . . . .	107
	<b>References</b>	<b>109</b>

# Nomenclature

## Acronyms

CC	Carbon capture
CCUS	Carbon capture, storage and utilization
CDS	Carbon dioxide splitting
CoE	Co-electrolysis
CR	Central receiver
CSP	Concentrating solar power
CSR	Circumsolar ratio
CT	Central tower
DIR(s)	Directly irradiated receiver(s)
DNI	Direct Normal Irradiance
DR	Dry reforming
HTF	Heat transfer fluid
HTM	Heat transfer medium
LF	Linear Fresnel
MORP	Metal oxide redox pair
MS	Multi-step
NG	Natural gas
NGSR	Natural gas steam reforming
GHG(s)	Greenhouse gas(es)
IIR(s)	Indirectly irradiated receiver(s)
IPCC	Intergovernmental Panel on Climate Change
LCOE	Levelised cost of electricity
NIST	National Institute of Standards and Technology
ODE	Ordinary differential equation
P2G	Power-to-gas
P2L	Power-to-liquid
PCM	Phase change material
POX	Partial oxidation
PSA	Pressure swing adsorption
PT	parabolic trough
RES	Renewable energy source(s)
RMSE	Root-mean-square error
RPC	Reticulated porous ceramic
SD	Solar dish
SE	Simple electrolysis
SNG	Synthetic natural gas
SR	Steam reforming
SSE	Sum of squared estimate of errors
STE	Solar thermal electricity
TES	Thermal energy storage
TGA	Thermogravimetric analysis
WGS	Water gas shift
WS	Water splitting

## Symbols

$A_c$	Concentrator aperture area [m <sup>2</sup> ]
$A_{\text{ext}}$	External surface of the receiver [m <sup>2</sup> ]
$A_r$	Receiver aperture area [m <sup>2</sup> ]
$C, C_g$	Geometric concentration ratio [-]
$C_{\text{max,opt,linear,cyl}}$	Maximum optical linear concentration ratio for cylindrical geometry [-]
$C_{\text{max,opt,linear,flat}}$	Maximum optical linear concentration ratio for flat geometry [-]
$C_{\text{max,opt,point,flat}}$	Maximum optical point concentration ratio for flat geometry [-]
$C_{\text{max,opt,point,spher}}$	Maximum optical point concentration ratio for spherical geometry [-]
$C_{\text{max,th,linear}}$	Maximum thermodynamic linear concentration ratio [-]
$C_{\text{max,th,point}}$	Maximum thermodynamic point concentration ratio [-]
$C_{\text{opt}}$	Local optical concentration ratio [-]
$\bar{C}_{\text{opt}}$	Surface-averaged optical concentration ratio [-]
$c_{p,i}$	Molar or mass specific heat capacity of the $i$ species [J mol <sup>-1</sup> K <sup>-1</sup> ] [J kg <sup>-1</sup> K <sup>-1</sup> ]
$D, d$	Diameter [m]
$D_{\text{ext}}$	External diameter [m]
$D_i$	Diffusion coefficient of the $i$ species [m <sup>2</sup> s <sup>-1</sup> ]
$E_a$	Activation energy [J mol <sup>-1</sup> ]
$E_{\text{Ar}}$	Energy separation for argon [J mol <sup>-1</sup> ]
$\dot{E}_{\text{losses}}$	Thermal losses [W]
$F$	Generalized body force [kg m <sup>-2</sup> s <sup>-2</sup> ]
$f$	Differential form of the kinetic model function [-]
$G$	Reference irradiance [W m <sup>-2</sup> ]
$G_{\text{const}}$	Solar constant [W m <sup>-2</sup> ]
$G_{\text{cs}}$	Integral solar intensity in the external angular annulus [W m <sup>-2</sup> ]
$G_s$	Integral solar intensity on the solar disc [W m <sup>-2</sup> ]
$g$	Integral form of the kinetic model function [-]
$g$	Gravitational acceleration [m s <sup>-2</sup> ]
$h$	Convective heat transfer coefficient [W m <sup>-2</sup> K <sup>-1</sup> ]
$HHV_i$	Molar higher heating value of the $i$ species [J mol <sup>-1</sup> ]
$HV_i$	Heating value of the $i$ species [J mol <sup>-1</sup> ]
$I$	Local irradiance on the receiver [W m <sup>-2</sup> ]
$\mathbf{I}$	Identity matrix
$I_{\text{solar}}$	Solar irradiance [W m <sup>-2</sup> ]
$\mathbf{j}_i$	Mass flux of the $i$ species [kg m <sup>-2</sup> s <sup>-1</sup> ]
$K$	Permeability [m <sup>2</sup> ]
$k_0$	Pre-exponential factor [s <sup>-1</sup> ]
$k$	Arrhenius form of the rate constant [s <sup>-1</sup> ]
$k$	Boltzmann constant [m <sup>2</sup> kg s <sup>-2</sup> K <sup>-1</sup> ]
$k_i$	Thermal conductivity of the $i$ species [W m <sup>-1</sup> K <sup>-1</sup> ]
$M_i$	Molar mass of the $i$ species [kg mol <sup>-1</sup> ]
$M_n$	Function of mass fractions and molar masses [kg mol <sup>-1</sup> ]
$m_i$	Mass of the $i$ species [kg]
$m_0$	Initial mass [kg]
$\tilde{m}$	Mass of the oxygen released [kg]
$m_\infty$	Final mass [kg]

$\dot{m}_i$	Mass flow rate of the $i$ species [kg s <sup>-1</sup> ]
$n_i$	Moles of the $i$ species [mol]
$\dot{n}_i$	Molar flow rate of the $i$ species [mol s <sup>-1</sup> ]
$Nu$	Nusselt number [-]
$p$	Pressure [Pa]
$p_i$	Partial pressure of the $i$ species [Pa]
$P_s$	Emitted power [W]
$P_{th}$	Thermal power [W]
$Pr$	Prandtl number [-]
$\dot{Q}_{abs}$	Absorbed radiation [W]
$\dot{Q}_{br}$	Mass source or sink [kg m <sup>-3</sup> s <sup>-1</sup> ]
$\dot{Q}_c$	Radiant power on the collector [W]
$\dot{Q}_{conc}$	Concentrated thermal power [W]
$\dot{Q}_{cond}$	Thermal power losses by conduction [W]
$\dot{Q}_{conv}$	Thermal power losses by convection [W]
$\dot{Q}_{furnace}$	Thermal power by the furnace [W]
$\dot{Q}_{input}$	Net radiation on the receiver [W]
$\dot{Q}_{loss}$	Overall thermal power losses [W]
$\dot{Q}_{net}''$	Net energy flux [W m <sup>-2</sup> ]
$\dot{Q}_r$	Radiant power emitted by the receiver [W]
$\dot{Q}_{rad}$	Thermal power losses by radiation [W]
$\dot{Q}_{refl}$	Reflected thermal power [W]
$\dot{Q}_{sink}$	Heat sink [W m <sup>-3</sup> ]
$\dot{Q}_{spil}$	Spilled thermal power [W]
$Q_{th}$	Thermal energy [J]
$\dot{Q}_{useful}$	Useful thermal power [W]
$\mathbf{q}$	Thermal flux [W m <sup>-2</sup> ]
$Ra$	Rayleigh number [-]
$R$	Gas constant [J mol <sup>-1</sup> K <sup>-1</sup> ]
$R^2$	Coefficient of determination [-]
$R_{cond}$	Conductive resistance of the receiver [m <sup>2</sup> K W <sup>-1</sup> ]
$r$	Reaction rate [s <sup>-1</sup> ]
$r_s$	Sun radius [m]
$r_{se}$	Mean distance between the sun and the Earth [m]
$\dot{S}_{O_2}$	Oxygen source function [kg m <sup>-3</sup> s <sup>-1</sup> ]
$T_0$	Reference temperature [K]
$T$	Temperature [K]
$T_{amb}$	Ambient temperature [K]
$\bar{T}_{ext}$	Temperature of the external surface of the receiver [K]
$T_r$	Temperature of the receiver [K]
$T_{sun}$	Equivalent absolute black body temperature of the sun [K]
$t$	Time [s]
$\mathbf{u}$	Velocity (or Darcy velocity) field [m s <sup>-1</sup> ]
$V_i$	Volume of the $i$ species [m <sup>3</sup> ]
$\dot{V}_i$	Volume flow rate of the $i$ species [m <sup>3</sup> s <sup>-1</sup> ]
$V_{mol}$	Molar volume of an ideal gas [m <sup>3</sup> mol <sup>-1</sup> ]
$y_i$	Molar fraction of the $i$ species [-]

## Greek Letters

$\alpha$	Receiver absorptivity [-]
$\alpha$	Temporal conversion function [-]
$\alpha$	Thermal diffusivity [ $\text{m}^2 \text{s}^{-1}$ ]
$\alpha_{\text{eff}}$	Effective receiver absorptivity [-]
$\beta$	Volumetric thermal expansion coefficient [ $\text{K}^{-1}$ ]
$\Delta h, \Delta H$	Enthalpy variation, enthalpy of reaction [ $\text{J mol}^{-1}$ ]
$\Delta G$	Gibbs free energy variation [ $\text{J mol}^{-1}$ ]
$\Delta m$	Mass variation [kg]
$\Delta t$	Time interval [s]
$\Delta T$	Temperature difference [K]
$\delta, \Delta\delta$	Nonstoichiometry, oxygen exchange capacity, oxygen storage capacity [-]
$\delta_{\text{red}}, \delta_{\text{ox}}$	Nonstoichiometry after reduction and after oxidation [-]
$\epsilon$	Receiver emissivity [-]
$\epsilon$	Thermal efficiency [-]
$\epsilon$	Relative error [-]
$\epsilon_i$	Characteristic energy for the $i$ species [ $\text{m}^2 \text{kg s}^{-2}$ ]
$\eta_c$	Carnot cycle efficiency [-]
$\eta_{\text{conversion}}$	Conversion efficiency [-]
$\eta_{\text{optical}}$	Optical efficiency [-]
$\eta_{\text{receiver}}$	Receiver efficiency [-]
$\eta_{\text{solar-to-fuel}}$	Solar-to-fuel efficiency [-]
$\eta_{\text{storage}}$	Storage efficiency [-]
$\eta_{\text{system}}$	System efficiency [-]
$\eta_{\text{th}}$	Thermal efficiency [-]
$\eta_{\text{thermochemical}}$	Thermochemical efficiency [-]
$\eta_{\text{thchem,CO}}$	Thermochemical efficiency in terms of CO production [-]
$\eta_{\text{transport}}$	Transport efficiency [-]
$\mu_i$	Dynamic viscosity of the $i$ species [Pa s]
$\nu$	Momentum diffusivity [ $\text{m}^2 \text{s}^{-1}$ ]
$\rho_i$	Density of the $i$ species [ $\text{kg m}^{-3}$ ]
$\sigma$	Stefan-Boltzmann constant [ $\text{W m}^{-2} \text{K}^{-4}$ ]
$\sigma_i$	Characteristic length for the $i$ species [ $\text{\AA}$ ]
$\theta$	Angular displacement [rad]
$\theta_s$	Solar cone angular displacement [rad]
$\phi$	Porosity [-]
$\Omega_D$	Diffusion collision integral [-]
$\omega_i$	Mass fraction of the $i$ species [-]

## List of Figures

1.1	Scenarios of global mean surface temperature rising according to IPCC report 2018 [1]. . . . .	21
1.2	Temperature impact from several sectors [2]. (a) Horizon of 20 years; (b) Horizon of 100 years. . . . .	21
1.3	A possible classification of hydrogen production processes [5]. . . . .	22
1.4	Possible listing of solar-aided routes for solar fuels production [6]. . . . .	25
1.5	Possible listing of solar-aided thermochemical routes for solar fuels production from carbonaceous feedstocks [6]. . . . .	25
2.1	CSP technologies currently available at commercial level [22]. . . . .	27
2.2	Tubular receivers in (a) external and (b) cavity configurations. . . . .	28
2.3	(a) Overall ideal efficiency $\eta_{\text{system}}$ as function of T, for different values of $C_g \equiv C$ (rearranged from [21]); (b) Maximum temperature $T_s$ achievable at the receiver, as function of the geometric concentration ratio $C$ . . . . .	30
2.4	Visualization of the solar radiation conical aperture [17]. (a) Aperture $\theta_s$ ; (b) Incident and reflected cones. . . . .	31
2.5	(a) Maximum temperature $T_s$ achievable at the receiver, as function of the geometric concentration ratio $C$ (Günther approach [23]); (b) $T_s(C)$ - Comparison of the two procedures used. . . . .	33
2.6	(a) Geometrical parameters describing parabolas and paraboloids [17]; (b) Interaction of the real angular width of the sun radiation with a parabolic concentrator [17]. . . . .	34
2.7	(a) Scheme of a parabolic trough system [21]; (b) PT geometry and ideal path followed by the incoming rays [24]. . . . .	37
2.8	(a) Scheme of a central tower system [21]; (b) CT geometry and radiation path. . . . .	38
2.9	(a) Linear Fresnel mirror (bottom) approximating a parabolic trough mirror (top) [25]; (b) Compound parabolic shaped secondary concentrator [25]. . . . .	38
2.10	Solar dish systems: (a) Diagram of EURODISH system, as reported in [27]; (b) Solar dishes at White Cliffs [28]. . . . .	39
2.11	Scheme of external (left) and cavity (right) receivers for SD systems [29]. . . . .	40
3.1	Classification of solar thermochemical processes [30]. . . . .	41
3.2	Main routes for CSP-aided thermochemical solar fuels production [4]. . . . .	42
3.3	High flux solar simulator, German Aerospace Center (DLR), Germany [30]. . . . .	47
3.4	Solar furnaces in (a) on-axis and (b) off-axis configurations [30]. . . . .	47
4.1	Crystal structure of fully oxidized ceria at normal pressure and temperature [33]. . . . .	51
4.2	Experimental reactors used in the work by Abanades and Flamant [37] for (a) reduction and (b) oxidation steps. . . . .	53
4.3	Kinetics of hydrogen production for different temperatures vs. time [37]. (a) $T_{\text{gas}} = 600^\circ\text{C}$ , 1.123 g of $\text{CeO}_{1.64}$ ; (b) $T_{\text{gas}} = 515^\circ\text{C}$ , 1.585 g of $\text{CeO}_{1.59}$ ; (c) $T_{\text{gas}} = 440^\circ\text{C}$ , 1.954 g of $\text{CeO}_{1.715}$ . . . . .	54
4.4	(a) $\text{O}_2$ and $\text{H}_2$ production rates and productivities, for $T_{\text{H}} = 1773\text{ K}$ (top) and $T_{\text{H}} = 1873\text{ K}$ (bottom) [33]; (b) $\text{CO}$ production rate vs. time using SDC15 at 1073 K, $\delta_{\text{red}} = 0.05$ , $p_{\text{CO}_2} = 0.032\text{ atm}$ [33]. . . . .	56
4.5	Aerosol reactor tested by Scheffe et al. [38]. . . . .	57
4.6	Total $\dot{m}_{\text{CeO}_{2-\delta}}$ on the balance and $\text{O}_2$ volume fraction vs. time, with: $T_{\text{f}} = 1873\text{ K}$ , $\dot{V}_{\text{Ar}} = 800\text{ sccm}$ , $D_{\text{v}50} = 21\ \mu\text{m}$ , $\delta_{\text{measured}} = 0.035$ , $p_{\text{O}_2, \text{baseline}} = 6.1 \times 10^{-5}\text{ atm}$ [38]. . . . .	58

4.7	(a) $\delta_{\text{measured}}$ as function of $m_{\text{CeO}_{2-\delta}}$ , with $T_f = 1773$ K, $\dot{V}_{\text{Ar}} = 500$ sccm, $D_{v50} = 12$ $\mu\text{m}$ , $p_{\text{O}_2, \text{baseline}} = (5 \times 10^{-5}) - (1.2 \times 10^{-4})$ atm; (b) $\delta_{\text{measured}}$ as function of $T_f$ , $D_{v50}$ , $m_{\text{CeO}_{2-\delta}}$ ranging from 15 to 110 mg (as reported by the authors) and $\dot{V}_{\text{Ar}}$ , with values of 200, 500 and 800 sccm respectively for the three points centered around each temperature value) [38]. . . . .	59
4.8	Total $\dot{m}_{\text{CeO}_{2-\delta}}$ on the balance and $\text{O}_2$ volume fraction vs. time, in case of continuous feeding [38]. . . . .	60
4.9	(a) $\eta_{\text{thermochemical}}$ vs. time for $\dot{m}_{\text{CeO}_2}$ of 61 mg s <sup>-1</sup> , 128 mg s <sup>-1</sup> and 462 mg s <sup>-1</sup> . Top two curves: $\dot{V}_{\text{Ar}} = 800$ sccm, $T_f = 1823$ K. Bottom curve: $\dot{V}_{\text{Ar}} = 500$ sccm, $T_f = 1818$ K. For all data, $D_{v50} = 12$ $\mu\text{m}$ ; (b) Average $\eta_{\text{thermochemical}}$ and $\delta_{\text{measured}}$ vs. $\dot{m}_{\text{CeO}_{2-\delta}}$ . Experimental conditions are the same as in Figure 4.9a [38]. . . . .	61
4.10	Solar reactor tested in the experimental demonstration by Welte et al. (readapted from [39]). . . . .	62
4.11	Experimental results from Welte et al. [39]. . . . .	63
4.12	TGA results from Furler et al. [48]. RPC-0 and RPC-50 samples were compared. Reduction was conducted at $T = 1773$ K and $p_{\text{O}_2} < 1.8 \times 10^{-4}$ atm. Oxidation was conducted at $T = 1273$ K and $p_{\text{CO}_2} = 0.385$ atm. . . . .	64
4.13	(a) Experimental set-up used by Charvin et al. [49] for performing (a) the reduction and (b) the oxidation steps. . . . .	65
4.14	Equilibrium compositions involving iron oxides. (a) Equilibrium composition for the Fe/O/H system, starting from 3 mol of FeO and 1 mol of H <sub>2</sub> O, at 1 bar in N <sub>2</sub> atmosphere [49]; (b) Equilibrium composition for the Fe/O/C system, starting from 3 mol of FeO and 1 mol of CO <sub>2</sub> , at 1 bar in N <sub>2</sub> atmosphere [50]. . . . .	66
4.15	H <sub>2</sub> molar fraction and temperature in time, measured by Charvin et al. [49] (sample mass: 2 g of FeO; particles size: $30 < d_p < 50$ $\mu\text{m}$ ; argon volume flow rate: 220 Nml/min). . . . .	68
4.16	Solar reactor used by Abanades et al. [50] for performing the reduction step from hematite towards wüstite under controlled atmosphere. . . . .	69
4.17	Experimental results in terms of chemical conversion vs. time from Abanades et al. [50] concerning the oxidation step. (a) Results in isothermal conditions, for the solar-reduced samples, for temperatures in the range 600-800°C and different particles diameter, and for a CO <sub>2</sub> concentration of 50%; (b) Results in dynamic conditions, for both the samples analysed, and for different CO <sub>2</sub> concentrations and particles diameter (this latter in the range 30-80 $\mu\text{m}$ when not specified). . . . .	70
5.1	TGA results for the cycle 1, together with the temperature evolution vs. time. (a) Relative mass (with respect to the initial value) vs. time for the three samples; (b) First derivative of the relative mass vs. time for the three samples; (c) Detail of (a) in the first minutes; (d) Detail of (b) during the oxidation phase. . . . .	75
5.2	TGA results for the cycles 2 and 3, together with the temperature evolution vs. time. (a) Relative mass (with respect to the initial value) vs. time for the three samples; (b) First derivative of the relative mass vs. time for the three samples; (c) Detail of (b) during the oxidation phase; (d) Detail of (b) during the reduction phase. . . . .	76
5.3	O <sub>2</sub> and CO <sub>2</sub> (a) production rates and (b) productivities resulting from TGA for cycles 2 and 3, and for the three samples analyzed; (c) Detail of (a); (d) Detail of (b). . . . .	77
5.4	(a) O <sub>2</sub> and (b) CO <sub>2</sub> standard volumes and average volume flowrates resulting from TGA for cycles 2 and 3, and for the three samples analyzed. . . . .	77
5.5	Nonstoichiometry $\Delta\delta$ resulting from TGA, for cycles 2 and 3, and for the three samples analyzed. . . . .	78

5.6	Thermochemical efficiencies resulting from TGA, for cycles 2 and 3, and for the three samples analyzed. . . . .	80
5.7	(a) $\alpha(t)$ for the reduction reactions; (b), (c) Details of (a); (d) $\alpha(t)$ for the oxidation reactions; (e), (f) Details of (d). . . . .	82
5.8	Reaction rates for the oxidized, reduced and virgin samples: (a), (b) and (c) Reduction phases; (d), (e) and (f) Oxidation phases. . . . .	82
5.9	Relative mass representations of (a) all the 10 cycles performed and of (b) the last 5 cycles performed, i.e., the ones studied. . . . .	83
5.10	Cycles representation: (a) plot from Bush and Loutzenhiser [53]; plots from the present analysis, respectively (b) with and (c) without full conversion reference level. . . . .	84
5.11	Temporal conversion function $\alpha(t)$ for (a) reduction and (b) oxidation phase, for the 5 cycles studied. . . . .	85
5.12	Experimental reaction rates $r(t)$ for (a) reduction and (b) oxidation phase, for the 5 cycles studied and for the first 5 minutes over a total of 15 min of each phase. . . . .	86
5.13	Details on the reaction rates curves: initial time instant, highest value detected and tail of the curve, respectively for (a, b, c) reduction and (d, e, f) oxidation phases. . . . .	86
5.14	Parity plots for reduction (left) and oxidation (right) phases from the reference work [53]. . . . .	87
5.15	Parity plots for (a) reduction and (b) oxidation phase of the 5 cycles studied; (c) Detail of (a); (d) Detail of (b). . . . .	87
5.16	O <sub>2</sub> results for the 5 cycles studied: (a) Standard volumes and average standard volume flow rates; (b) Productivities; (c) Production rates. . . . .	88
5.17	Relative mass representations of (a) all the 5 cycles performed and of (b) the last 4 cycles performed, i.e., the ones studied. . . . .	89
5.18	Cycles representation: plots from the present analysis, respectively (a) with and (b) without full conversion reference level. . . . .	90
5.19	Experimental reaction rates $r(t)$ for (a) reduction and (b) oxidation phase, for the 4 cycles studied and respectively for the 15 minutes of reduction and for 10 minutes over a total of 30 min of oxidation; (c) Detail of (a); (d) Detail of (b). . . . .	91
5.20	Parity plots for (a) reduction and (b) oxidation phase of the 4 cycles studied. . . . .	91
5.21	Standard volumes and standard volume flow rates for (a) O <sub>2</sub> released and (b) CO produced. . . . .	92
5.22	(a) O <sub>2</sub> and CO productivities; (b) O <sub>2</sub> production rates; (c) CO production rates. . . . .	92
6.1	Data-fitting of the experimental data from thermal reduction of test#1 through different kinetic models with the theoretical line. . . . .	96
6.2	Cylindrical geometry implemented in the model: (a) Whole geometry; (b) Alumina tube; (c) Free-flow regions; (d) Porous medium region. . . . .	97
6.3	Space convergence results after 1000 s in terms of relative errors, respectively (a) for the temperature in the most exposed point and (b) for the oxygen mass flux across the outlet section of the porous medium. . . . .	103
6.4	Mesh selected for the final simulation: (a) Uniform mesh in the whole domain; (b) Detail of the inlet cross section. . . . .	103
6.5	(a) Detail of the velocity field in the porous region; (b) Pressure field on the outer surface (the pressure is basically uniform on a given cross section, since gravity effects were neglected). . . . .	104

6.6	(a) Temperature distribution on the outer surface at $t_{\text{final}}$ ; (b) Temperature distribution on the central cross section at $t_{\text{final}}$ ; (c) Temperature profile on the most exposed edge of the receiver at $t_{\text{final}}$ ; (d) Temperature evolution in time in the most exposed point of the receiver. . . . .	105
6.7	O <sub>2</sub> molar fraction field: (a) $t = 60$ s; (b) $t = t_{\text{final}}$ ; (c) Detail of (b); (d) Time evolution of the surface-averaged O <sub>2</sub> molar fraction on the outlet section. . . . .	105
6.8	Kinetic results from the model: (a) Temporal conversion function $\alpha(t)$ and $\tilde{m}(t)$ ; (b) Reaction rate $r(t)$ and $\frac{d\tilde{m}}{dt}$ . . . . .	106

## List of Tables

3.1	Solar reactors employed for performing WS/CDS thermochemical cycles [6]	49
4.1	Experimental results from Welte et al. [39]	63
4.2	Experimental results from Charvin et al. [49] for the high temperature reduction step at 1700°C	67
4.3	Experimental results from Charvin et al. [49] for the low temperature oxidation step: the solar-reduced wüstite (subscript <i>s</i> ) and a commercial one (subscript <i>c</i> ) are compared in terms of volume of hydrogen produced, chemical conversion (based on stoichiometric FeO) of the initial sample and mole of hydrogen produced per gram of FeO	68
5.1	Technical data of the thermogravimetric analyzer STA 2500 Regulus [47].	72
5.2	Thermal program of the experimental TGA procedure on cerium oxides.	73
5.3	Summary and comparison among the literature results and the outcomes of the present work, as concerns nonstoichiometric ceria.	79
5.4	Thermal program of the test#1 experimental TGA procedure on iron oxides.	83
5.5	Thermal program of the test#2 experimental TGA procedure on iron oxides.	89
5.6	Comparison of the CO productivities among Abanades et al. [50] and the present work.	93
5.7	Comparison of the CO productivities among Farooqui et al. [54] and the present work.	93
5.8	Summarizing table of the results obtained in terms of O <sub>2</sub> and CO yields with cerium oxides and iron oxides.	93
5.9	Thermal program for an equivalent mixed cycle based on test#1 and test#2, with the same structure of the cerium oxides based cycles.	94
5.10	Thermochemical efficiencies obtained in the present experimental analyses, through the formula and with the hypotheses proposed.	94
6.1	Results of the two best models among the ones tested.	96
6.2	Kinetic models used for gas-solid reactions [54]	96
6.3	Geometric data used in the model.	98
6.4	Properties of the materials used in the model.	98

## Abstract

The present work deals with experimental and numerical analyses of thermochemical cycles. This technological pathway aims at producing hydrogen or synthesis gas starting from water or water/carbon dioxide mixture, respectively. In case both of these latter feeds are supplied to the process, the resulting synthesis gas mixture, made up of hydrogen and carbon monoxide, can be further treated downstream to obtain higher complexity chemicals, e.g. through Fischer-Tropsch processing. Nowadays, the importance of developing processes capable to treat and valorise carbon dioxide emissions lies in the possibility to face as effectively as possible climate changes and global warming, in the framework of a global decarbonization policy. It is noteworthy that such thermochemical path should be powered by renewable energy sources, typically concentrating solar power (CSP), for ensuring ideally a zero-impact as regards carbon dioxide net emissions. Under the experimental point of view, thermogravimetric analysis (TGA) was conducted with a CO<sub>2</sub> feeding on two different well-known materials, namely cerium oxides and iron oxides, to experimentally characterize their behaviour and performances in the given working conditions and select the most appropriate one for a CSP-driven cycle. Both these metal oxides were already extensively studied so far for thermochemical cycles applications, and several previous works from the literature review will be reported herein for sake of comparison and completeness. The TGA procedures allowed to conclude that using iron oxides leads to higher productivities and higher production rates in terms of oxygen released during the reduction phase, and of fuel produced during the following oxidation phase. Besides this, also higher thermochemical conversion efficiencies were proved. Thus, iron oxides were selected for performing a numerical simulation in COMSOL Multiphysics<sup>®</sup> environment as a further step of the workflow. The numerical model simulates the cylindrical solar receiver-reactor of the CSP system installed at the Energy Center research pole, Turin (Italy), and in particular the iron oxide transient reduction reaction that takes place with the given boundary conditions imposed. In the real system, the receiver is placed in the focus of the paraboloidal concentrator to absorb as much solar radiation as possible. The concentrator was not considered inside the numerical simulation, apart from a thermal flux boundary condition imposed on the external walls of the cylinder. Starting from the TGA experimental outcomes, the kinetic parameters of interest were estimated through a data-fitting procedure and were used in the model as a thermochemical *boundary* condition. The functional form for the reaction rate, in which the parameters were implemented, was retrieved from literature, where the same mathematical expression was used with similar materials. The model allowed to obtain as a main output the evolution in time of the oxygen concentration at the outflow section. A possible future work will focus on the numerical model validation on field, through direct experimental runs on the real CSP system just described.

## 0 Preliminaries

### 0.1 Motivation and objectives

The interest in the topic discussed in this work, both general in the scientific community and personal one, comes from the awareness of how it is so important nowadays to search for valid solutions in all directions viable, as concerns, for instance, the energy engineering field as well as the chemical and sustainable process engineering one, in order to build a strong carbon-free *way-of-thinking* at all the levels of the human society. Such a *greener and greener* process is not so easy to perform, being the present infrastructure based mostly on carbon containing fuels feeding. As will be mentioned later in this work, thermochemical cycles could be a viable solution to mitigate the deleterious effects coming from using carbon-containing molecules and to feed anyway the present anthropic activities, without necessarily replace all the existing infrastructure, that would be actually a not negligible effort at all, and basically impossible to perform in relatively short time horizons. Thus, the objective of the present analysis lies in proving the practical feasibility of such thermochemical processes, making use also of authoritative literature sources.

### 0.2 Structure of the work and how to read it

The work is organized in 6 Sections:

*i.* **Section 1** will introduce the reader to the present global framework, with particular emphasis on the role of hydrogen in the energy sector;

*ii.* **Section 2** will give a background on the concentrating solar power (CSP) facilities, since the solar energy is foreseen to play an important role in the future energy systems and processes;

*iii.* **Section 3** will go deeper into the solar-driven thermochemical processes aimed at producing hydrogen or syngas, this latter typically furtherly processed downstream in the chemical industry sector;

*iv.* **Section 4** will enter the core of the analysis, through a literature review on the thermochemical cycles of interest for the present work;

*v.* **Section 5** will present the experimental activity that was conducted at Politecnico di Torino and all the results obtained, with both cerium oxides and iron oxides samples. An approach based on thermogravimetric analysis (TGA) is proposed;

*vi.* **Section 6** will close the discussion proposing a numerical model for simulating a part of a thermochemical cycle, namely the higher temperature thermal reduction of the iron oxides based cycle.

The introductory Sections 1 to 3 are useful if the reader is interested in having a background on the topic before going deeper into the analysis. In particular, Section 2 can be skipped if CSP technologies are already well known, since it represents just a wide discussion on the concentrated solar source, and it is not needed for getting the results obtained in the last two sections. For a full understanding of the core topic, it is sufficient just to have a look to Section 4, before going on towards the last two ones.

# 1 Introduction

## 1.1 Climate change and decarbonization. The role of hydrogen in the energy framework

One of the most demanding challenges for the human society in the current years is dealing for sure with the decarbonization path that should be followed in order to reduce as much as possible the environmental impact of the anthropic activities as a whole. The greenhouse gases (GHG or GHGs) emissions e.g. coming from the conventional power production systems are intimately connected with the climate change effects and thus with the global warming. In this framework, a role of importance is played by the carbon dioxide emissions, besides other GHGs such as methane ( $\text{CH}_4$ ) or nitrous oxide ( $\text{N}_2\text{O}$ ). It is important to look at the impact not only in terms of rising of the atmosphere temperature, but also at the timescale. GHGs will have different persistency in the atmosphere.  $\text{CO}_2$  is actually the most severe GHG: this is not because it affects mostly the radiative properties of the atmosphere, but because it will live up there a longer time once it is emitted. It is chemically very stable: once emitted, it will stay in the atmosphere for centuries. On the other hand, for instance the methane is more reactive, and once emitted it will have a higher probability to be converted in something else. The environmental impact issues are being strongly debated recently: the main goal of the Paris agreement (2015) was indeed to strengthen the effort of the involved countries worldwide for keeping the temperature rising well below  $2^\circ\text{C}$  with respect to the preindustrial level at the end of the current century, possibly even less than  $1.5^\circ\text{C}$ . Figure 1.1 shows the global warming effects with respect to the second half of the nineteenth century, according to the Intergovernmental Panel on Climate Change (IPCC) report published in 2018 [1]. The orange arrow and the horizontal bar show respectively the estimated mean value and the likely interval of the time instant at which a warming of  $1.5^\circ\text{C}$  will be reached with the present (i.e., 2017) slope. The temperature the plot refers to is, as indicated, the observed monthly global mean surface one. The grey trend shows the projection of the likely interval for the temperature rising in the case of linear decreasing from 2020 on of the  $\text{CO}_2$  emissions until a zero is reached in 2055, and considering a radiative forcing not linked to  $\text{CO}_2$  (i.e., change in the soil use, emissions of aerosols, etc.) reaching its maximum in 2030. The blue trend shows a similar scenario, but in which the  $\text{CO}_2$  emissions are supposed to reach a zero value in 2040 after the linear decreasing phase. Finally, the purple scenario is the one in which the  $\text{CO}_2$  emissions reach the zero in 2055, with a constant radiative forcing not linked to  $\text{CO}_2$  being constant from 2030 on. Observing the blue curve, it is clear that a faster reduction of the  $\text{CO}_2$  emissions leads to a higher probability to contain the global warming below the threshold of  $1.5^\circ\text{C}$  at the end of the century (i.e., the blue confidence interval is almost completely below the threshold level). It is worth to highlight which are actually the main sources of  $\text{CO}_2$  and other relevant GHGs. Figure 1.2 shows the temperature impact of several sectors in terms of different gas emissions [2]. Data refer to two different horizons, respectively 20 years and 100 years from the moment in which the analysis was performed, and for a 1-year pulse of emissions [2]. Looking at the net global mean temperature change by source sector after 20 years (Figure 1.2a), the most relevant contributions are those of industry and energy sectors. The cumulated impact is of 40 mK/y over all sectors analyzed [2]. There are some aerosols and particulates that instead will reflect back the incoming radiation from the Sun, and so they will actually have a positive effect on the Earth's temperature. Looking at the same diagram but on a timescale of 100 years (Figure 1.2b), some contributions will disappear, while  $\text{CO}_2$  is the only one that is still surviving, producing about the same impact, because of the higher lifetime in the atmosphere. The cumulated impact in this case is of 25-30 mK/y [2]. Summarizing, the driving force of the climate change is the burning of fuels: the main contributors are the energy sector,

the industry sector, the biomass burning, road transport and household fossil fuel and biofuel. As an yearly average, the carbon increase in the atmosphere is of roughly  $15 \text{ Gt}_{\text{CO}_2}/\text{y}$ , that is, the corresponding  $\text{CO}_2$  concentration is increasing with a rate of  $2 \text{ ppmv}/\text{y}$  [2]. It is reported that, at present, the levels in the atmosphere are more than  $412 \text{ ppmv}$  [3].

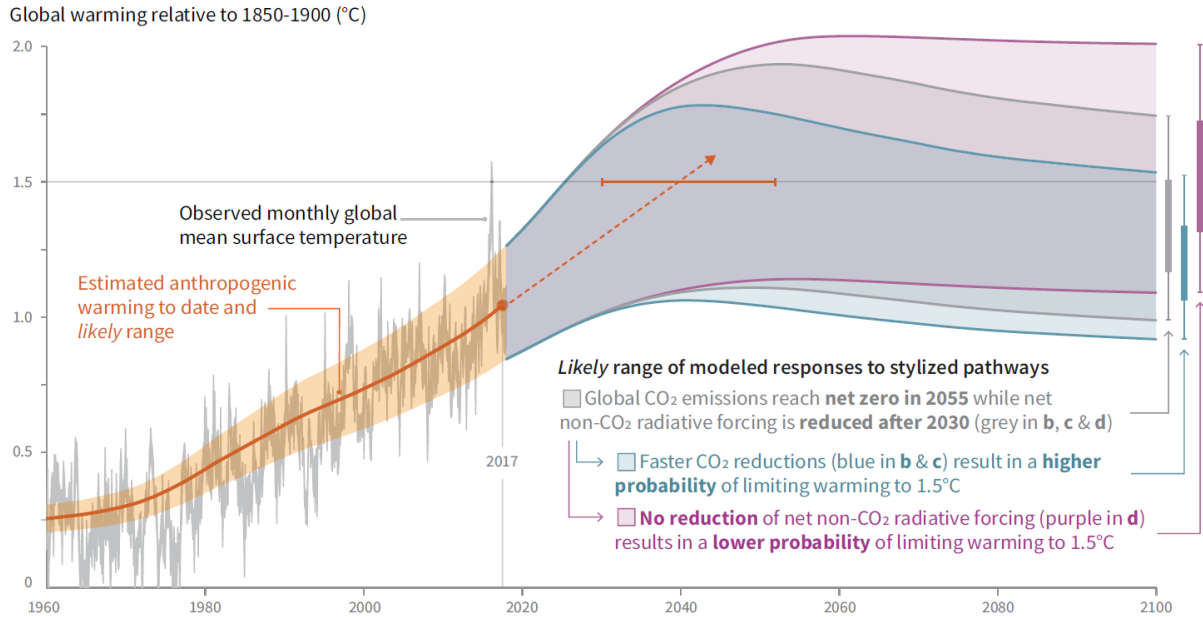


Figure 1.1: Scenarios of global mean surface temperature rising according to IPCC report 2018 [1].

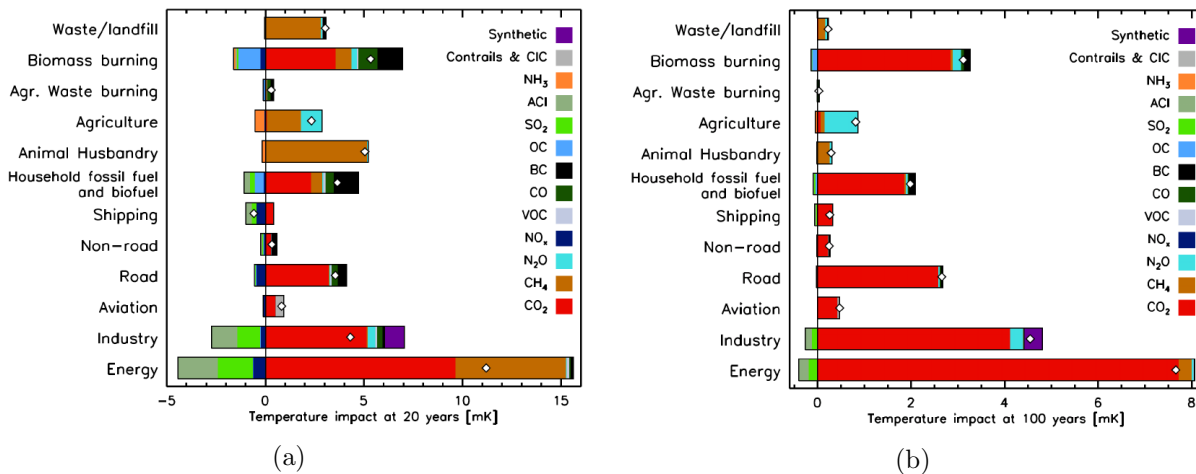


Figure 1.2: Temperature impact from several sectors [2]. (a) Horizon of 20 years; (b) Horizon of 100 years.

Thus, decarbonization policies are strongly needed. Being the society today still mostly based on fossil fuels (let's think about the road transport sector), then it follows that it will take years, or decades, to completely decarbonize our way of living. Although the final goal would be the transition to a totally carbon-free era, it is obvious that some *interim solutions* are needed in the meanwhile. Carbon capture, utilization and storage (CCUS) technologies are going in this direc-

tion. In particular, CCUS facilities are all those technical solutions aimed at capturing/isolating and possibly using a given stream of  $\text{CO}_2$  in order to avoid it to enter the atmosphere. Abundant literature is available as concerns this topic [11, 12, 13, 14, 15, 16]. The importance of dealing with such a possibility is that, starting from water and carbon dioxide, it is possible to run renewable processes (e.g. solar driven ones) in order to synthesize several fuels and chemicals, that otherwise would imply the use of fossil carbon. This can assure a sort of circular carbon economy as an intermediate solution towards a completely carbon-free era. However, CCUS technologies, in particular carbon capture (CC) dedicated sections in the existing power plants, imply important additional energy and economic costs, and this is the reason why the  $\text{CO}_2$  capture is not performed unless there is a law that imposes it. On the other hand, together with the CCUS path, a promising solution seems to consider the hydrogen as one of the new leading actors in the worldwide energy framework, even because its combustion does not lead to any pollutant emission, since just water is produced. Hydrogen is a promising energy carrier in several key sectors, such as transportation, domestic use or various industrial applications [4]. Nowadays, around 300 billion of liters of  $\text{H}_2$  per year are produced, and the most massive consumer is the chemical industry, e.g. for producing fertilizers or ammonia [4]. There exist several technological pathways for producing hydrogen. Figure 1.3 [5] shows a possible classification of hydrogen production processes from several energy sources, both fossil and renewable, although it does not pretend here to be definitively complete and exhaustive. The picture shows how different paths are viable in order to obtain eventually hydrogen that can be used for several end-use applications.

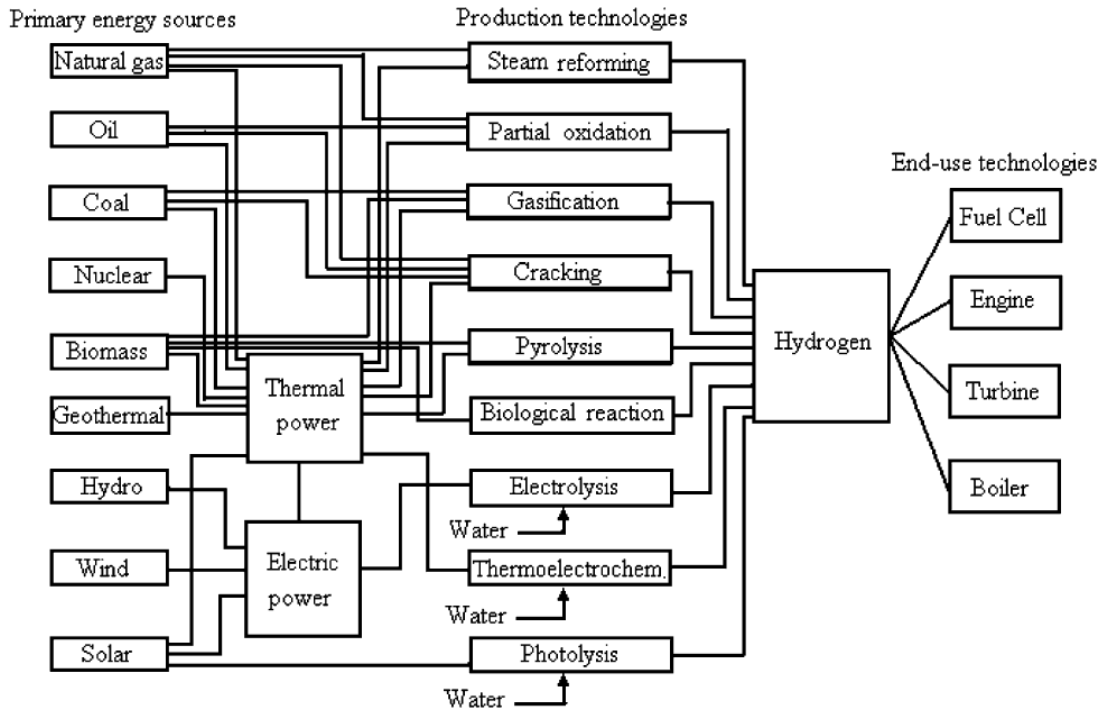
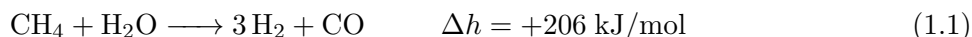


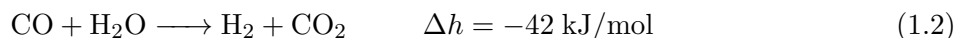
Figure 1.3: A possible classification of hydrogen production processes [5].

The possible routes nowadays are thus in a large number. A coarse classification of the typologies of processes available is the subdivision in thermochemical, electrochemical, photochemical or biochemical pathways, according to if high temperature heat, electric power, photons energy or biological reactions are respectively involved, or even hybrid combinations of these main items [6].

There exist completely renewable processes, in which both the energy input and the mass input processed are both renewable by definition, as happens e.g. for solar driven biomass gasification, and only partially renewable processes, as happens e.g. for solar driven coal gasification [7], in which the energy input is solar-derived high temperature heat, but the feedstock processed has a fossil origin, and thus the process is not 100% clean. A fairly wide category of processes for H<sub>2</sub> production is the one involving steam reforming (SR) reactions, that can be achieved starting from several possible feeds. The SR processes involve both fossil feedstocks, such as natural gas or other hydrocarbons (e.g. ethanol), and renewable feedstocks, such as biomass or biogas. Comprehensive studies about SR processes for hydrogen production are widely available in literature [8]. Nowadays, a major fraction of the total amount of H<sub>2</sub> produced, namely more than 50% according to Kaiwen et al. [8], comes from steam methane reforming of natural gas (NGSR), because of its abundance and the maturity of the process, that leads on its turn to a convenient economics for such plants and to a relatively low installed capital cost [8]. The fraction of total H<sub>2</sub> produced worldwide from fossil fuels is around 96%, being the remaining 4% coming from water electrolysis [4]. The NGSR process is thus the most diffuse way to produce hydrogen e.g. for industrial purposes at present. The process involves typically a first desulphurization stage to remove the S-compounds contained in the NG coming from the grid (usually 3 to 4 ppm), before reaching the actual reforming reactor, in which the following steam methane reforming endothermic reaction takes place at temperatures between 500°C and 950°C, at a pressure of around 30 bar and using Ni as catalyst [5]:



Then, a water gas shift (WGS) step is typically foreseen to convert the carbon monoxide still present in the resulting gas mixture into hydrogen and carbon dioxide, according to the following exothermic reaction:



Reaction 1.2 is typically carried out at lower temperatures and in several stages. Higher temperature shifts at around 350°C use iron-based catalysts, while lower temperature shifts at around 205°C use copper-based catalysts [5]. Last two conceptual steps are the condensation for the water removal and a clean-up pressure swing adsorption (PSA) unit for obtaining high purity (99.99%) H<sub>2</sub> and removing the residual water, methane, CO<sub>2</sub>, N<sub>2</sub> and CO [5]. The process can reach conversion efficiencies of the order of 60 to 85%, according to the plant size considered [2]. In such process, high temperature heat and water have thus to be supplied, and the heat is typically provided via burning natural gas [5]. Let's precise that a gas mixture composed of H<sub>2</sub> and CO, as the one resulting from Reaction 1.1, is usually referred to as syngas (i.e., synthesis gas). It is easily understandable that processes such as the SR ones imply a heavy depletion of fossil fuels and thus important GHGs emissions, and it is for this reason that both these drawbacks could and should be mitigated and possibly overcome by the viable option of RES-based hydrogen production methods. As concerns photochemical and biochemical processes, they are not of interest for the present work, and thus will not be covered here in detail. However, deeper information about them can be found in dedicated literature [9, 10]. Not even electrochemical processes are of direct interest for this analysis, but some information about that will be anyway reported in the lines below, being electrolysis holding nowadays some percentage points in worldwide H<sub>2</sub> production, as said above. Electrochemical processes are based on electrolysis non-spontaneous reactions fed by electric power, that in the cases of interest here will be coming from RES, both through direct conversion units (solar photovoltaic, hydro power, wind power) or through indirect conversion units (thermoelectric cycles fed e.g. by solar or geothermal sources). It is possible to obtain as output both just hydrogen

or a syngas, and thus to deal with two sub-possibilities:

i. *Simple electrolysis* (SE) is referred to as the electrolysis reaction of water alone, leading to pure hydrogen:



ii. *Co-electrolysis* (CoE) is referred to as the electrolysis of both water and  $\text{CO}_2$ , leading to a syngas as output mixture. The additional reaction related to the  $\text{CO}_2$  that adds to Reaction 1.3 is the following:



Such processes can be properly coupled with thermocatalytic stages in the framework of power-to-gas (P2G) and power-to-liquid (P2L), for the production of synthetic natural gas (SNG) or further precursor molecules, such as methanol or dimethylethere [2].

Section 3 will be devoted to  $\text{H}_2$  production through *solar thermochemical* processes. In the thermochemical framework, the route of solar-fed thermochemical processes is the one in which the high temperature heat is typically delivered through concentrating solar power (CSP) facilities. Being the solar energy one the most abundant RES on the Earth, its use for hydrogen production seems to be a virtuous solution. A comment of importance is that not just hydrogen can be produced, but even a syngas, composed, as said, mainly of  $\text{H}_2$  and CO in different possible amounts. Both these energy carriers, when obtained through thermochemical solar processing, are referred to as *solar fuels* (or *solar syngas* and *solar hydrogen* if only  $\text{H}_2$  is produced). In the broad sense, solar fuels are also all those fuels such as synthetic liquid hydrocarbons and alcohols produced through reactions between  $\text{H}_2$  and CO coming from solar-aided processes [6]. In this work, however, the expression *solar fuels* will refer mainly to solar hydrogen or solar syngas, unless otherwise stated. The thermochemical mechanisms according to which these molecules are obtained will be properly covered. The reason why even the production of a syngas could be a pursuable solution is that it is possible to couple such processes to CCUS systems, thereby reducing the impact of  $\text{CO}_2$  emissions. Further comprehensive reference classifications are given in Figures 1.4 and 1.5 [6]. In particular, Figure 1.4 shows a possible listing of various solar-aided processes for solar fuels (hydrogen, syngas or derived synthetic fuels) production, namely of thermochemical, photochemical/photobiological or electrochemical nature. Figure 1.5 gives finally a possible picture of solar fuels production paths from carbonaceous feedstocks: in this case, just thermochemical methods are considered, namely reforming reactions, splitting (e.g. through chemical cycles) and gasification. However, since Section 3 will be devoted to a more comprehensive treatment on the thermochemical pathways viable, further details are not reported here.

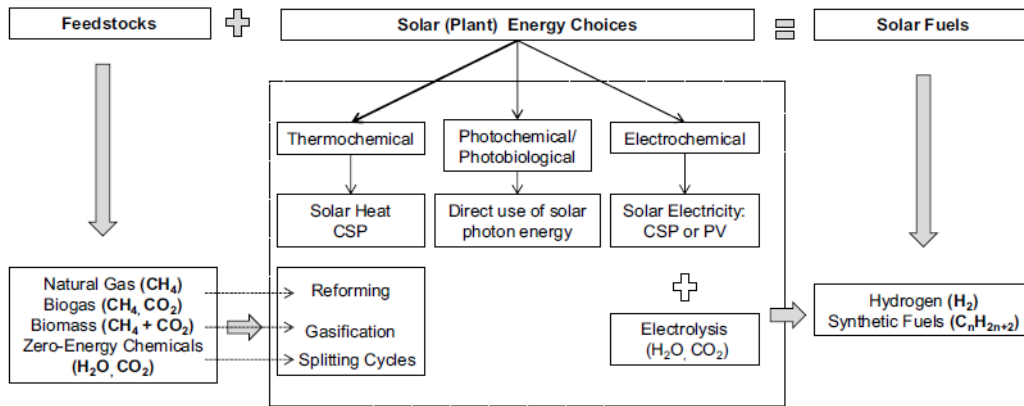


Figure 1.4: Possible listing of solar-aided routes for solar fuels production [6].

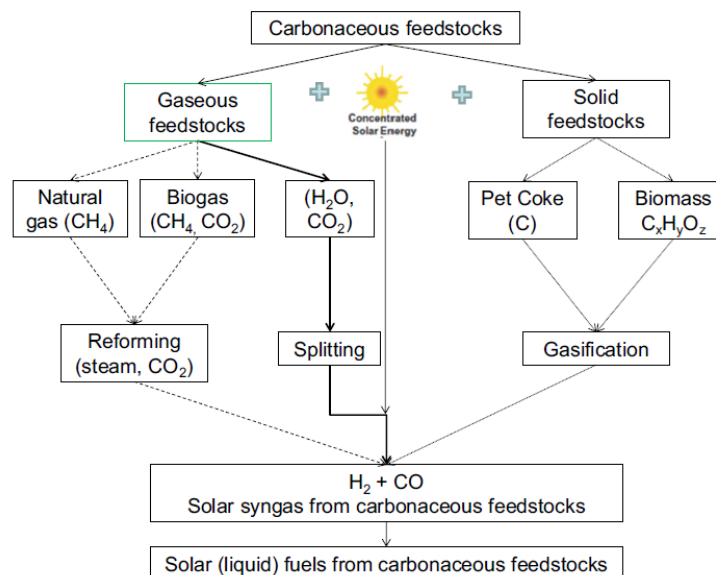


Figure 1.5: Possible listing of solar-aided thermochemical routes for solar fuels production from carbonaceous feedstocks [6].

## 2 Concentrating solar power (CSP) technologies

Since the solar source is being considered at present one of the most promising renewable sources under a decarbonization perspective, it is useful to report here some hints on this type of facilities. A concentrating solar power (CSP) plant is a system able to capture the solar radiation, to concentrate it and to deliver high temperature heat to a downstream application. The interest in CSP in these last years is growing because of the relevant potential role of the solar energy source in the framework of a wholly sustainable global development and of a more and more renewable energy supply searched for, as consequence of the decarbonization path needed to face climate changes and global warming, as discussed in Subsection 1.1 above. After a first phase of commercial development around the 1980s and 1990s, then no further strong interest was seen until 2005 [17, 18], when climate changes have become a more concrete and understood reality and solar resource started to be considered as an important player in this context among the several renewable alternatives. Besides the most diffuse application nowadays for electricity production, CSP can be a solution even in other fields, for instance as a source of process heat for several industrial sectors, power input for desalination plants in areas with freshwater deficit or as thermal power input for solar fuels production processes [18], with all the environmental benefits that come from not using fossil fuels as primary energy source. It has been estimated that one square meter of concentrator for electricity production can lead to a reduction of 200 to 300 kilograms of carbon dioxide each year [18]. Although the interest for the present work lies in exploiting the solar resource for solar fuels production through thermochemical cycles, since the importance of such systems is of interest at present, as said, even for electricity production (indeed, CSP is sometimes referred to also as solar thermal electricity, STE), it is worth to mention some general information about this possibility. Besides the environmental upsides, even the economics of such installations is getting better: at 2016, the generation costs for solar generated electricity are around 12 UScents/kWh in locations reached by high solar irradiation [18]. The global weighted average levelised cost of electricity (LCOE) at a utility scale has decreased instead from 0.346 2019USD/kWh to 0.182 2019USD/kWh between 2010 and 2019, against e.g. values of 0.378 to 0.068 2019USD/kWh for solar photovoltaics [19]. Adding stronger and stronger contribution of STE could also stabilize costs at a grid level, against the fossil fuels derived variability [18]. The global STE capacity at 2018 amounts at almost 5.5 GW, with 550 MW having come online in 2018, with China and Morocco as leading actors in the capacity additions in this year, both with 200 MW added [20]. The global leaders remained however Spain and United States, with respectively 2.3 GW and roughly 1.7 GW installed at the end of the year [20]. The most suitable locations for a CSP installation are located in the belt between 40° of latitude north or south [18], as the European Mediterranean countries, because of the higher solar availability and intensity. As a comparison, a CSP plant located in such a suitable area could produce more than 100 GWh of solar electricity per year, equivalent to the energy produced by a 50 MW coal-fired or gas-fired conventional power plant [18]. Although a CSP facility can be coupled with several downstream applications, the solar-related core of the system remains the same. CSP systems collect the so-called *Direct Normal Irradiation* (DNI), or *beam radiation* (i.e., the direct beam component of solar radiation, defined as the direct radiation coming from the sun and measured on a flat plane normal to the sun's rays [17]), that is the portion of the solar radiation managing to reach the Earth's surface without being deviated by clouds or atmospheric dust. The general working principle of a CSP system is the following: the solar radiant energy is first concentrated through reflecting mirrors, called *concentrators* (sometimes called otherwise *collectors* or *heliostats*), and then reflected/redirected towards a *receiver* (or *absorber*), aimed at (i) absorbing the radiant power and at (ii) transferring it to a heat transfer medium passing through it. In case of electricity production applications, the power cycle integration is performed in different

ways according to the typology of plant considered. In general, however, a common solution is to use an intermediate heat transfer fluid (HTF) to collect the thermal power in the solar field and transport it to the power block. The power cycle fluid is typically steam, used downstream for the production of electricity through conventional solutions implementing steam turbines, with the possibility of intermediate thermal storage such as solid media (e.g. concrete), molten salts or phase change materials (PCM) [18, 21]. Alternatively, some configurations can implement direct steam generation, without intermediate fluids. The possibility of the storage is not a negligible option at all, since even during night the turbine can be run in case of demand matching needs. Such type of plants are thus well suited for instance in all those countries where the summer cooling demand is relevant, such as Spain or California [18]. At the end of 2018, almost 17 GWh of thermal energy storage (TES) was operational at a global level [20]. The thermal storage opportunity has as consequence the dispatchability of such plants, that is for sure a further added value with respect e.g. to wind power or solar photovoltaics, a higher capacity factor and a source of grid flexibility. Currently, the commercial-level CSP technologies are parabolic trough, central tower, linear Fresnel and paraboloidal dish systems (see Figure 2.1 [22]). Parabolic troughs and linear Fresnel belong to the linear-focus concentrators, being the radiation concentrated according to a linear geometry, while the central towers and paraboloidal dishes belong to the point-focus concentrators, being the radiation concentrated - ideally - in a single point. The radiation concentration can reach factors of 50 to 100 for linear-focus systems and even several hundreds or thousands for point-focus systems [17].

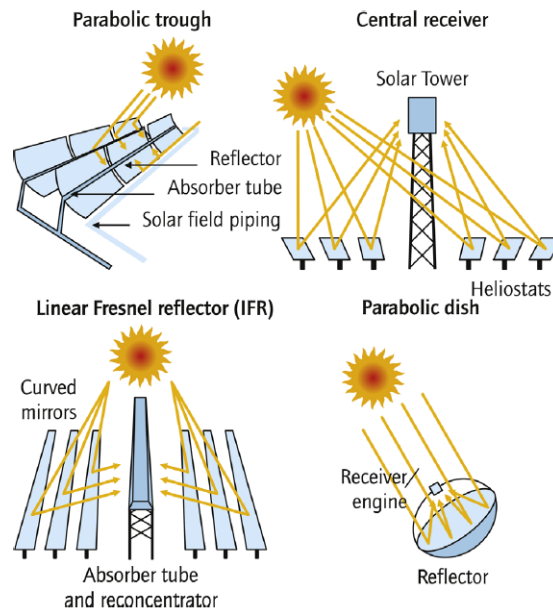


Figure 2.1: CSP technologies currently available at commercial level [22].

## 2.1 Receivers for CSP

As already mentioned, the receiver in a CSP facility is the connection point between the concentrators, that collect and concentrate the solar radiation, and the rest of the plant. The main two functions of a receiver, already cited above, are to (i) absorb the concentrated radiation, that will convert into thermal power, and to (ii) transfer it to a proper heat transfer medium. Being the receiver the *hot spot* of the plant, since the highest temperatures are reached here, then it follows

that this component is definitely the most affected one as concerns the thermal losses towards the environment. Loss items will be treated in Subsection 2.2.3. It is precised from now that a receiver can consist either in (i) a pure heat transfer unit, aimed at transferring thermal power downstream, or in (ii) a so called *solar reactor* (or *receiver-reactor*), in which solar-derived thermal power is used to thermocatalyze endothermic chemical reactions, as happens in solar fuels production facilities and in general in solar-aided thermochemical processes. Receivers can be broadly classified according to several criteria and in several ways, as briefly reported below [6, 21]:

**i.** According to the *heat transfer mechanism* involved, five categories can be identified. (1) In *tubular* receivers, the HTF flows in one or more tubes, and these ones are the most diffused; in (2) *volumetric* receivers, the heat is absorbed within the entire volume of the absorber, being the heat transfer medium directly exposed to radiation, thus allowing for a very efficient heat transfer and for high temperatures achievable. The absorber can be a stationary matrix (such as foam or honeycomb [6]) or moving solid particles [6] (in this case, the particles transport dynamics and residence times have to be taken into account); (3) *plate* (or *channel*) receivers use micro-flow channels for the fluid to pass through, while in (4) *heat pipe* receivers the heat is transferred to the working fluid through an intermediate boiling or condensing fluid;

**ii.** According to the *geometrical configuration*, the subdivision is among *external* receivers and *cavity* receivers. External receivers are hit by radiation on their external surface, while cavity receivers allow the beams to enter in a cavity, in which they can be even reabsorbed or re-emitted through multiple reflection paths. Due to this particular geometry, in a cavity receiver the effective absorptive surface is higher than the aperture area seen by radiation, and radiative losses are reduced at high temperatures with respect to an external one, since the surface exposed to the external environment is smaller. These two typologies are shown in Figure 2.2, in which both cases tubular panels are used for the fluid flow. In particular, from Figure 2.2b it is clear how the receiver aperture area, available for the radiation to pass, is much smaller than the actual surface that will absorb it.

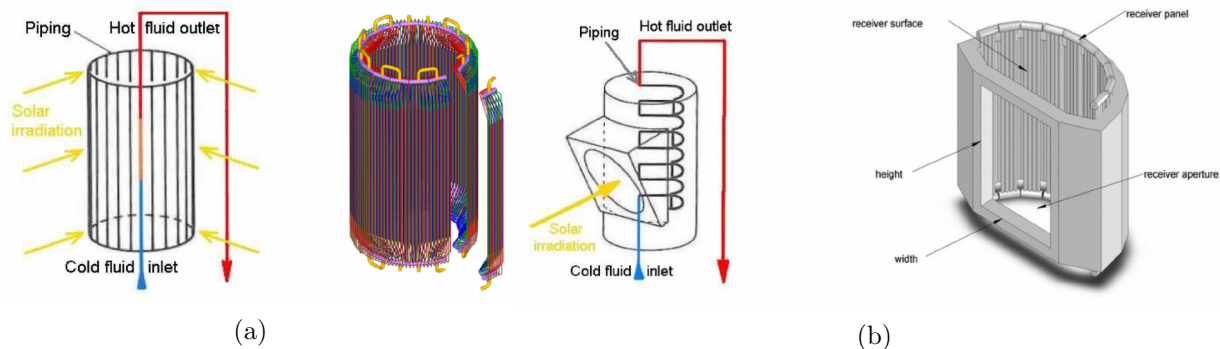


Figure 2.2: Tubular receivers in (a) external and (b) cavity configurations.

**iii.** According purely to the interaction with solar radiation, the two receiver typologies are the *Indirectly Irradiated Receivers* (IIRs) and the *Directly Irradiated Receivers* (DIRs) [6]. This way of classifying receivers partially superimposes with the heat transfer mechanism one reported as first bullet. IIRs use absorbing surfaces exposed to solar radiation, and heat is transported towards the heat transfer fluid through their walls (it is what happens e.g. in tubular receivers). DIRs use instead fluid streams, solid particles or other structures directly exposed to solar radiation, allowing the heat to penetrate inside the entire volume of the absorber. This group corresponds to the volumetric receivers one described in the previous lines;

iv. According to the *heat transfer medium* used, the viable options are multiphase fluids (e.g. in direct steam generation), gas phase (e.g. air, helium, CO<sub>2</sub>), liquid phase (e.g. heat transfer oil, molten salts) or solid phase (e.g. solid particles as mentioned above);

v. According to the *application* of interest, several possibilities are available, such as power generation (steam Rankine cycle, Brayton cycle using a gas turbine, Stirling cycle), thermochemical processing (solar gasification, solar fuels production) or process heat (industry purposes).

In general, however, the receiver has to be designed in order to approach the black body behaviour in trapping the incident radiation, e.g. through cavity geometries, black painting or porous volumetric absorbers [6]. While in this subsection just some general information on receivers have been reported, more focused details on solar chemical reactors can be found in Subsection 3.2.

## 2.2 Fundamentals on CSP technologies

In this subsection, a theory background on CSP technologies will be given, in order to get the physics that lies behind such systems.

### 2.2.1 Thermodynamic generalities

Looking at the overall solar-to-electric conversion efficiency of a CSP system, this can be generally defined as the product of the several efficiencies relating to the single blocks, as follows [17]:

$$\eta_{\text{system}} = \eta_{\text{optical}} \cdot \eta_{\text{receiver}} \cdot \eta_{\text{transport}} \cdot \eta_{\text{storage}} \cdot \eta_{\text{conversion}} \quad (2.1)$$

This definition, that can be evaluated both in a precise time instant or as time-averaged, relates to a general STE plant: more suitable definitions for the efficiencies in case of CSP-fed solar fuels production processes will be reported later. The only piece of information to be fixed now is that some items of losses will characterize all the steps in the conversion chain, either optical ones such as the ones occurring at the concentrator level or strictly thermal ones, such as the ones that prevail at the receiver level. To better understand the performances evaluation for a CSP system, some deeper considerations will be now mentioned.

For simplicity, let's define from now on  $G$  as a reference irradiance equal to 1000 W/m<sup>2</sup> (or "1 sun"),  $A_c$  as the concentrator (or collector) aperture area and  $A_r$  as the receiver aperture area, onto which the collector is redirecting the concentrated sunlight. The *aperture area* is defined as the area *seen* by the incoming radiation along the direction of its path. Let's abstract to a case in which the collector has a perfect optics, in the sense that the radiation is optically, perfectly re-projected on the receiver, without reflection-related or slope-related errors. Furthermore, let  $C_g \equiv C = \frac{A_c}{A_r}$  be the - geometric - *concentration ratio* characterizing the system,  $\alpha$  the receiver absorptivity and  $\epsilon$  the receiver emissivity. Then, the energy balance on the receiver can be written as in Equation 2.2 [21], where the net output energy flux results from the difference between the entering absorbed flux and the exiting re-emitted flux:

$$\dot{Q}_{\text{net}}'' = \alpha GC - \epsilon \sigma T^4 \quad (2.2)$$

$T$  is the equilibrium temperature of the receiver. The Stefan-Boltzmann law has been used, with  $\sigma = 5.67 \cdot 10^{-8} \frac{W}{m^2 K^4}$  as it is known. The thermal efficiency of such a system can thus be evaluated through Equation 2.3 as the ratio between the net energy output and the total radiant energy input:

$$\eta_{\text{th}} = \frac{\dot{Q}_{\text{net}}'' A_r}{GC A_r} = \alpha - \epsilon \frac{\sigma T^4}{GC} \quad (2.3)$$

In the limit of the receiver being a black-body cavity, then  $\alpha = \epsilon = 1$  and the expression becomes the following:

$$\eta_{\text{th}} = 1 - \frac{\sigma T^4}{GC} \quad (2.4)$$

If  $\eta_{\text{th}}$  is multiplied by the efficiency of a Carnot engine that ideally operates between the temperature  $T$  (at which the heat is delivered from the receiver) and a reference temperature  $T_0 = 300$  K, the overall system efficiency can be defined as follows:

$$\eta = \eta_c \cdot \eta_{\text{th}} = \left(1 - \frac{T_0}{T}\right) \left(1 - \frac{\sigma T^4}{GC}\right) \quad (2.5)$$

The efficiency behaviour as function of  $T$  and for different values of the concentration ratio  $C$  (reported in the vicinity of the corresponding curves) is shown in Figure 2.3a below: it is clear that there exists an optimal theoretical value of temperature, for a given concentration ratio, that maximizes the efficiency, as well as that the higher the concentration ratio, the higher the efficiency for a given temperature. The efficiency has a zero value for  $T = T_0$  and for  $T = T_s = \sqrt[4]{\frac{GC}{\sigma}}$  referred to as *stagnation temperature*, at which the system reaches the thermal equilibrium with the heat source and thus the maximum theoretical temperature. The maximum efficiency and the corresponding temperature for a given  $C$  can be found solving numerically the equation  $\frac{d\eta}{dT} = 0$  [21]. A step further can be done searching for the explicit behaviour of the maximum temperature achievable,  $T_s$ , as function of the concentration ratio  $C$ , as shown in Figure 2.3b. This latter picture refers actually to a value of  $G = G_{\text{const}} = 1367 \text{ W/m}^2$ , referred to as the *solar constant* and corresponding to the solar irradiance that reaches the outer atmosphere. The reason for this choice is that, in the following paragraph, the same result will be obtained through a different approach and using the value  $G_{\text{const}}$ , thus some more comments will be reported in a while.

Although high concentration ratios are desirable, the maximum concentration achievable in a real CSP system is upper bounded by both thermodynamic and optical limits. In the following paragraphs, something more on this will be mentioned.

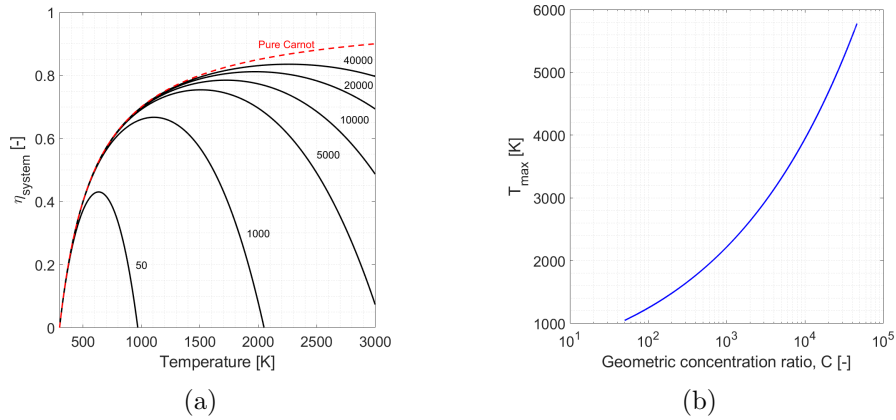


Figure 2.3: (a) Overall ideal efficiency  $\eta_{\text{system}}$  as function of  $T$ , for different values of  $C_g \equiv C$  (rearranged from [21]); (b) Maximum temperature  $T_s$  achievable at the receiver, as function of the geometric concentration ratio  $C$ .

## 2.2.2 Thermodynamic and optical limits on concentration

For the discussion that will follow, it is useful to introduce still some more theoretical recaps. The first information to be kept is that the solar radiation reaches the Earth not as perfectly parallel rays, but as distributed in a conical fashion with an aperture  $\theta_s \approx 4.65$  mrad, as shown in Figure 2.4 [17], due to the finite diameter of the sun.

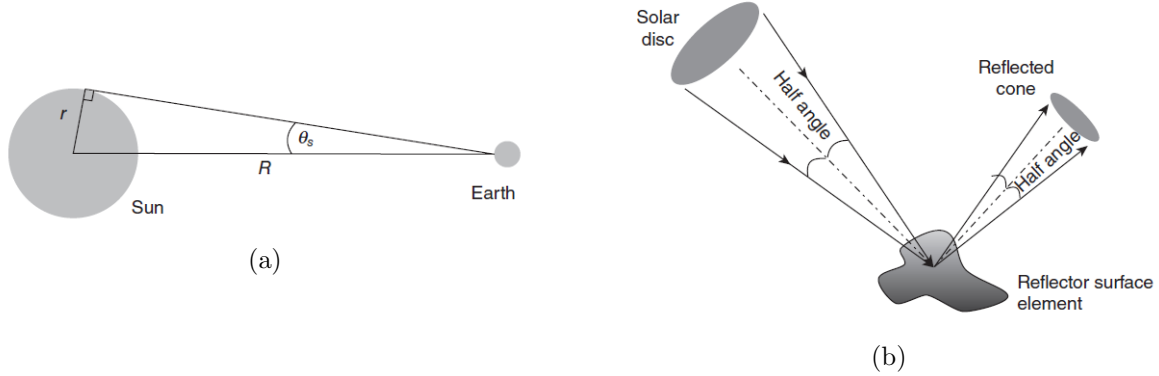


Figure 2.4: Visualization of the solar radiation conical aperture [17]. (a) Aperture  $\theta_s$ ; (b) Incident and reflected cones.

However, radiation comes actually from a wider angular range, being the intensity distribution at the edges not a perfect *step function* (*solar intensity* is here used as synonymous of irradiance, thus as a radiant power per unit area). The distribution of the solar radiation intensity as function of the angular displacement is referred to as the sun shape [17]. The parameter used in this sense is the circumsolar ratio (CSR), defined as  $CSR = \frac{G_{cs}}{G_{cs} + G_s}$ .  $G_s$  is the integral solar intensity just on the solar disc, while  $G_{cs}$  is the integral solar intensity in the annulus going from  $\theta = \theta_s = 4.65$  mrad to  $\theta = 43.6$  mrad, this latter being chosen conventionally [17]. The sun shape distribution is a function of the atmospheric conditions, such as presence of moisture or particulate matter [17]. The importance of introducing this notions is that the CSR value can affect the concentration efficiency of a CSP system, because the higher the circumsolar fraction of the overall radiation, the higher the spillage and thus radiation losses [17].

Turning now to the concentration limits, it is possible to prove that the highest values of geometric concentration ratios achievable according to the second law of thermodynamics assume the following values reported in Equations 2.6 and 2.7, respectively for point-focus and linear-focus concentrators [17]:

$$C_{\max, \text{th}, \text{point}} = \frac{A_c}{A_r} = \frac{1}{\sin^2 \theta} \Big|_{\theta = \theta_s} \approx 46250 \quad (2.6)$$

$$C_{\max, \text{th}, \text{linear}} = \frac{A_c}{A_r} = \frac{1}{\sin \theta} \Big|_{\theta = \theta_s} \approx 215 \quad (2.7)$$

It is worth to stress that these values correspond theoretically to the maximum, thermodynamic upper bound for the concentration ratio of any solar concentrator. Further details about the proof of such expressions are not reported here for sake of conciseness, but they can be found in the references [17]. The angle  $\theta$  in the equations above is the acceptance angle, defined as the maximum angle at which the incoming solar radiation is capable to be captured by the given solar

concentrator, and the limits are calculated as indicated for  $\theta = \theta_s$ . Indeed, the acceptance angle in real concentrators will be typically very close to the sun's angular width  $\theta_s$  [17]. Having defined the thermodynamic limits, it is possible now to return back to what has been said in the previous paragraph regarding the behaviour of  $T_s$  against the concentration ratio  $C$ . The second approach, proposed by Günther [23], is here quickly shown. Let's define at this aim some quantities: let  $r_s \approx 696000$  km [23] be the sun radius,  $r_{se} \approx 1.496 \cdot 10^{11}$  m the mean distance between the sun and the Earth and  $T_{\text{sun}} \approx 5777$  K the equivalent black body temperature of the sun (i.e., the solar radiation intensity and spectrum are well approximated by the black body spectrum at 5777 K). Then, the emitted power  $P_s$  and the aforementioned solar constant  $G_{\text{const}}$  are evaluated as follows:

$$P_s = 4\pi r_s^2 \sigma T_{\text{sun}}^4 \quad (2.8)$$

$$G_{\text{const}} = \frac{P_s}{4\pi r_{se}^2} \quad (2.9)$$

Neglecting the atmospheric attenuation effects, that is actually a strong hypothesis, the radiant power that reaches the collector aperture area  $A_c$ , using also the expressions above, is written as

$$\dot{Q}_c = A_c \frac{P_s}{4\pi r_{se}^2} = A_c \frac{4\pi r_s^2 \sigma T_{\text{sun}}^4}{4\pi r_{se}^2} = A_c \sigma T_{\text{sun}}^4 \frac{r_s^2}{r_{se}^2} \quad (2.10)$$

The radiant power emitted by the receiver, if the receiver aperture area of interest for the re-emission is  $A_r$  and its temperature is  $T_r$ , is written as

$$\dot{Q}_r = A_r \sigma T_r^4 \quad (2.11)$$

The maximum temperature is reached when the radiant power incident on the collector aperture area is balanced by the radiant power re-emitted by the absorber, as follows:

$$\dot{Q}_c = \dot{Q}_r \longrightarrow A_c \sigma T_{\text{sun}}^4 \frac{r_s^2}{r_{se}^2} = A_r \sigma T_r^4 \quad (2.12)$$

If a maximum concentration ratio  $C_{\text{max}}$  is defined such that  $\frac{r_s^2}{r_{se}^2} = \frac{1}{C_{\text{max}}} \approx \frac{1}{46200}$  through some approximations [23], and  $C = \frac{A_c}{A_r}$  is the already defined geometric concentration ratio, then making some simple algebra the following expression is obtained:

$$T_r = T_{\text{sun}} \left( \frac{C}{46200} \right)^{\frac{1}{4}} \quad (2.13)$$

Equation 2.13 expresses once again the maximum temperature reachable by the receiver/absorber at the thermal equilibrium as a function of the geometric concentration ratio. Let's notice that  $C_{\text{max}}$  and  $C_{\text{max,th,point}}$  previously defined in Equation 2.6 are *exactly* the same quantity: the very little difference comes from some round off approximations used in the two methods, and they have been maintained separate just to be faithful to the references. Figure 2.5a below shows the trend obtained for  $T_s(C)$  through this second Günther approach, while Figure 2.5b shows both the results coming from the first, energy-balance-based procedure (i.e., the one already shown in Figure 2.3b above) and the results coming from this second, Günther approach: the output is practically the same, being the two curves completely superimposed.

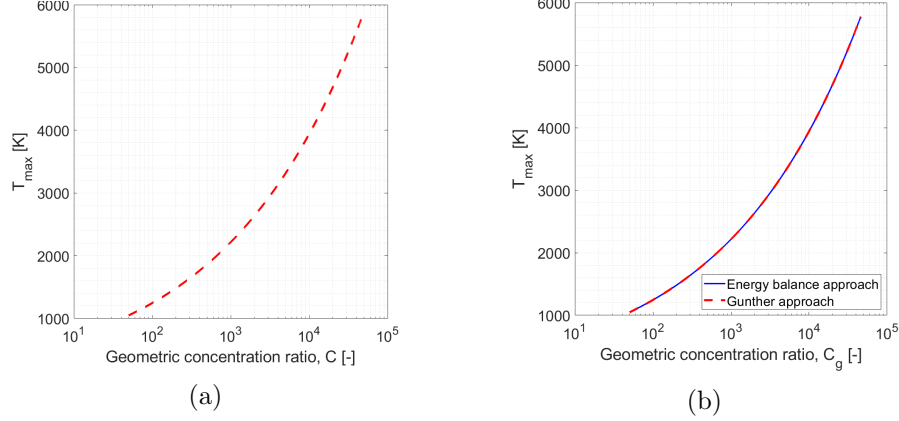


Figure 2.5: (a) Maximum temperature  $T_s$  achievable at the receiver, as function of the geometric concentration ratio  $C$  (Günther approach [23]); (b)  $T_s(C)$  - Comparison of the two procedures used.

Round off approximations do not affect the comparison shown in Figure 2.5b above. Some last considerations have to be mentioned. The equilibrium temperature for the maximum concentration ratio achievable (as said equal to  $C_{\max}$  or  $C_{\max,th,point}$ , interchangeably) corresponds to the sun's temperature, as expected from the second law. What is again observed is that the receiver  $T_{\max}$  increases as the concentration increases, and this further confirms that it is better to have higher values for  $C$ . However, as it is known, these results are purely theoretical: from the Günther equations above, it can be well seen that both the sun and the absorber are considered to be black bodies, and this never happens in reality; moreover, just radiation is taken into account, while in general even conductive and convective heat transfer could develop, and this would reduce the maximum temperature achievable. Another idealization that was made is to neglect all the atmospheric interferences during the radiation path towards the collector, as already said. This concludes the part related to thermodynamic limits.

To introduce now the optical limits of concentration, some recaps on parabolic (in two dimensions) and paraboloidal (in three dimensions) geometries are mentioned. Figure 2.6a taken from [17] summarizes the most important notions to deal with. These geometries are exploited in CSP concentrators, respectively in parabolic trough and in solar dish ones, because of the property to redirect - i.e., reflect - the incident radiation parallel to the axis towards a single point, defined as the *focus*. As it is known, the way to describe the two geometries are mathematically exactly the same, being a paraboloid the natural extension of a parabola. If  $x$ ,  $y$  and  $z$  define the cartesian coordinates system, being the  $y$  axis and the  $z$  axis respectively the axes of the parabola and of the paraboloid, and defining  $f$  as the distance between the focus and the vertex, and  $W$  and  $z_R$  as represented in the figure, then the functional shape for the two geometries can be described as in equations below [17]:

$$y = \frac{x^2}{4f} \quad (2.14)$$

$$z = \frac{x^2 + y^2}{4f} \quad (2.15)$$

The *rim angle*  $\phi_R$  in the figure is the angular aperture from the axis to the edge of the concentrator. According to Equation 2.16, the rim angle  $\phi_R$  and the focal length  $f$  completely define the geometry.

$$\tan \phi_R = \frac{W/2}{f - z_R} = \frac{4fW/2}{4f^2 - (W/2)^2} \quad (2.16)$$

Whilst Figure 2.6a shows the ideal case of perfectly parallel incident radiation, Figure 2.6b reports the real situation, in which the conical aperture  $\theta_s$  of the beams coming from the sun has to be taken into account.

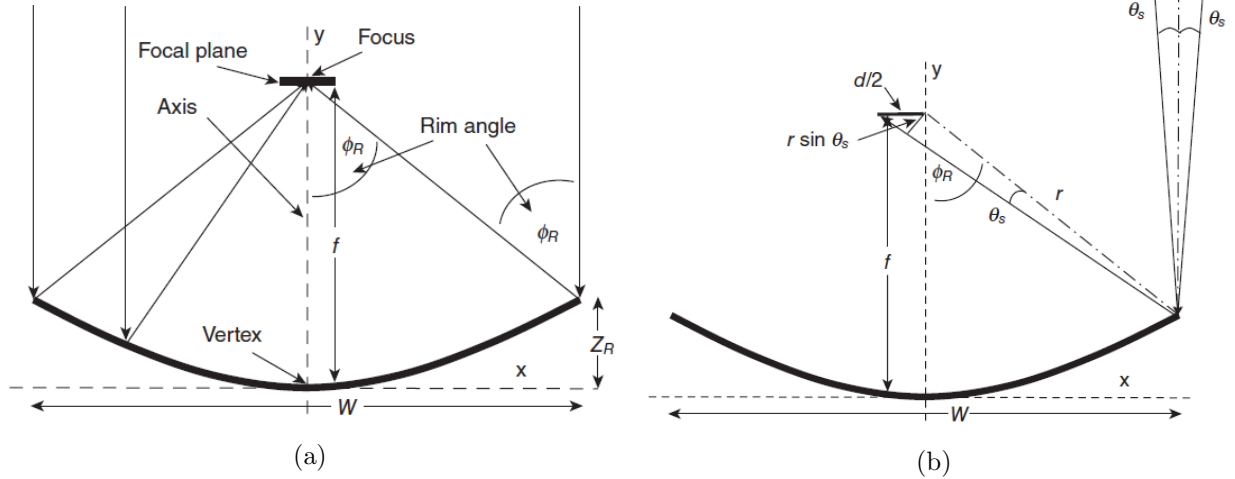


Figure 2.6: (a) Geometrical parameters describing parabolas and paraboloids [17]; (b) Interaction of the real angular width of the sun radiation with a parabolic concentrator [17].

The angular width  $\theta_s$  is the reason for the reduction of the maximum concentration achievable under a purely optical point of view. Once again, it is possible to prove making some algebra that the maximum *optical* limits achievable for the concentration ratio are the one reported in the Equations below (corresponding, in the order, to: trough with flat receiver, trough with cylindrical cross section receiver, dish with flat receiver, dish with spherical receiver):

$$C_{\max,\text{opt},\text{linear},\text{flat}} = \frac{1}{2}C_{\max,\text{th},\text{linear}} = \frac{1}{2\sin\theta_s} \approx 108 \quad (2.17)$$

$$C_{\max,\text{opt},\text{linear},\text{cyl}} = \frac{1}{\pi}C_{\max,\text{th},\text{linear}} = \frac{1}{\pi\sin\theta_s} \approx 68.5 \quad (2.18)$$

$$C_{\max,\text{opt},\text{point},\text{flat}} = \frac{1}{4}C_{\max,\text{th},\text{point}} = \frac{1}{4\sin^2\theta_s} \approx 11600 \quad (2.19)$$

$$C_{\max,\text{opt},\text{point},\text{spher}} = \frac{1}{4}C_{\max,\text{th},\text{point}} = \frac{1}{4\sin^2\theta_s} \approx 11600 \quad (2.20)$$

Thus, optics further reduces the thermodynamic limits found out before. It is actually possible to get closer to the thermodynamic limits, but with the drawback of having spilled rays and so a lower optical efficiency [21].

What has been found out so far is thus a theoretical background concerning an ideal situation in which the maximum concentration ratios could be reached, taking into account both thermodynamics and optics. Anyway, it is obvious that real systems will be subjected to several items of losses distributed all along the energy conversion chain, and both of thermal and optical nature. Some information about this are reported in the following paragraph.

### 2.2.3 Thermal and optical losses

Optical losses, as expected, are of interest mainly in dealing with the concentrators, and so for the first step in the energy conversion chain, that is, the capture and concentration of the solar

radiation. Thermal losses are instead interesting to be analysed mainly at the receiver level, where the radiant energy is actually converted into heat and the system reaches very high temperatures. Both these issues are presented in this paragraph.

An exhaustive classification of possible optical losses can be attained thinking about a CSP central tower system, as listed below [21]:

**i.** *Cosine losses* occur when the heliostat (i.e., the reflecting mirror) is not perfectly oriented in the normal direction with respect to the sun. This implies that the solar radiation *sees* a smaller reflecting area, and the overall sunlight that is actually reflected reduces. The item of error concerning these losses are the *tracking errors*, i.e., the mirror has a wrong orientation with respect to the ideal one;

**ii.** *Blocking losses* occur when the reflected radiation is blocked by another mirror and cannot reach the receiver;

**iii.** *Shading losses* occur when a fraction of the heliostat is shadowed by another heliostat;

**iv.** *Reflection losses* relate to the imperfect reflectivity of the mirrors. This item of optical losses is due both to *slope errors* in the mirrors, that is, local waviness with characteristic length of roughly 1 cm to 1 m, and to *specularity errors*, that is, very local roughness effects, of much smaller length scale, due to the mirror production process;

**v.** *Spillage losses* occur when the reflected radiation does not hit the receiver, as a consequence of the abovementioned tracking errors, slope errors or specularity errors;

**vi.** *Atmospheric attenuation losses* are due to atmospheric scattering phenomena in the path from the mirror to the receiver;

**vii.** *Receiver reflection losses*, related this time not to the heliostats field, but to the imperfect absorptivity of the receiver surface.

Further items of losses could be mentioned, such as the ones related to secondary optics systems [21], but they are not of interest for the present work. Furthermore, it should be noticed that not all of these loss items are useful in dealing with a solar dish CSP system, as the one that will be used later in the experimental activity, but it was worth to report a fairly comprehensive list for having a relatively complete idea about that.

For dealing now with the thermal losses, the attention should be focused on the receiver, where the concentrated sunlight is absorbed and released towards a heat transfer medium (HTM). The different existing types of receivers have been briefly described in the previous subsection.

At steady state, the incoming radiation on the receiver will be balanced by the increase in enthalpy of the HTM and by several item of losses, namely conductive, convective and radiative losses, besides the aforementioned reflective losses. Thus, the energy balance can be written as follows:

$$\dot{Q}_{\text{useful}} = \dot{Q}_{\text{conc}} - \dot{Q}_{\text{spil}} - \dot{Q}_{\text{refl}} - \dot{Q}_{\text{cond}} - \dot{Q}_{\text{conv}} - \dot{Q}_{\text{rad}} \quad (2.21)$$

$\dot{Q}_{\text{useful}}$  is the useful energy retrieved through the HTM,  $\dot{Q}_{\text{conc}} - \dot{Q}_{\text{spil}} \equiv \dot{Q}_{\text{input}}$  is the net radiation that hits the receiver (difference between concentrated radiation and spillage-related radiation) and the other terms have the already explained loss meaning. The four items of losses can be summed up in the term  $\dot{Q}_{\text{loss}}$ . The efficiency of the receiver  $\eta_{\text{receiver}}$ , already mentioned in the overall Equation 2.1, is built as

$$\eta_{\text{receiver}} = \frac{\dot{Q}_{\text{useful}}}{\dot{Q}_{\text{input}}} = \frac{\dot{Q}_{\text{input}} - \dot{Q}_{\text{loss}}}{\dot{Q}_{\text{input}}} \quad (2.22)$$

A relevant comment is that the term  $\dot{Q}_{\text{useful}}$  can be either the increase in enthalpy of a HTF or e.g. the chemical energy stored in the output flow, as will be in case of solar fuels production through thermochemical cycles, that is the situation of interest. Some more details about solar reactors and more focused application of CSP systems for thermochemical purposes will be properly reported

in Subsection 3.2. If the conversion process is not working, the receiver efficiency will go to zero coherently with the absence of a useful effect at the output. The equilibrium temperature that the receiver will reach is the already mentioned *stagnation temperature*,  $T_s$ , at which the input energy will be balanced by the losses. For high concentration systems,  $T_s$  is likely to be too much high to be directly measured before the destruction of the receiver itself.

For evaluating analytically the thermal losses items, it is useful to define the optical concentration ratio,  $C_{\text{opt}}$ , that results to be more precise than the purely geometric one because it takes into account the actual radiation hitting the receiver and all the optical effects. The *local*  $C_{\text{opt}}$  and the surface-averaged one are reported, in the order, in the following two equations.

$$C_{\text{opt}} = \frac{I}{I_{\text{solar}}} \quad (2.23)$$

$$\bar{C}_{\text{opt}} = \frac{\int I \, dA_r}{A_r I_{\text{solar}}} \quad (2.24)$$

$A_r$  is the already defined aperture area of the receiver,  $I$  is the local irradiance on the receiver and  $I_{\text{solar}}$  is the solar irradiance. Observing now that the algebraic sum given by  $\dot{Q}_{\text{conc}} - \dot{Q}_{\text{spil}} - \dot{Q}_{\text{refl}}$  corresponds to the absorbed radiation (that will convert into useful effect plus losses), then a corresponding term  $\dot{Q}_{\text{abs}}$  can be defined to take them wholly into account. The absorbed radiation can be evaluated as follows:

$$\dot{Q}_{\text{abs}} = \alpha_{\text{eff}} \bar{C}_{\text{opt}} G A_r \quad (2.25)$$

$\alpha_{\text{eff}}$  is the *effective absorptivity* of the receiver, that will correspond to the material absorptivity only in case of a flat surface, while it will be different in case of a cavity receiver, for which the internal multiple reflections and absorptions should be taken into account [21]. A similar reasoning leads to define an *effective emissivity*,  $\epsilon_{\text{eff}}$ , that will be different from the material emissivity if a cavity receiver will be used. If  $T_{\text{amb}}$  is the ambient temperature,  $\bar{T}_{\text{ext}}$  is the average external surface temperature of the receiver,  $A_{\text{ext}}$  is the external surface of the receiver,  $h$  is the average heat transfer coefficient taking into account both natural and forced convection, and  $R_{\text{cond}}$  is a properly defined conductive resistance of the receiver, then the energy balance in Equation 2.21 can be rewritten as follows:

$$\dot{Q}_{\text{useful}} = \alpha_{\text{eff}} \bar{C}_{\text{opt}} G A_r - A_{\text{ext}} \frac{\bar{T}_{\text{ext}} - T_{\text{amb}}}{R_{\text{cond}}} - h A_{\text{ext}} (\bar{T}_{\text{ext}} - T_{\text{amb}}) - \sigma \epsilon_{\text{eff}} A_r (\bar{T}_{\text{ext}}^4 - T_{\text{amb}}^4) \quad (2.26)$$

$\dot{Q}_{\text{useful}}$  will be expressed coherently with the nature of the useful effect at the output. In principle, Equation 2.26 could be solved numerically for  $\bar{T}_{\text{ext}}$ . It is worth to highlight that conductive and convective losses increase as the external surface  $A_{\text{ext}}$  increases, while radiative emission losses increase for increasing aperture areas,  $A_r$ , characterized by higher view factor towards the external environment. For decreasing aperture areas, radiative losses decrease, but an increase in optical spillage losses is observed too, as expected. Radiative losses can be thus reduced or minimized either (i) using a cavity receiver instead of an external one, and assuring that the lower temperature region is the nearest one to the external aperture, and that the highest temperature one is the farthest from the external aperture, or (ii) using selective surfaces, with high solar-weighted (i.e., at lower wavelengths) absorptivity but low thermal-weighted (i.e., at higher wavelengths) emissivity [21]. Convective losses can be instead reduced or minimized either (i) confining the receiver surface using a transparent window or (ii) through an active air curtain to retain hot air currents within the receiver (in case of cavity receivers) [21].

For each typology of CSP plant, some more details will be reported for completeness in the following subsection.

## 2.3 Typologies of CSP facilities

In the order, parabolic trough, central tower, linear Fresnel and dish systems will be briefly described.

**i.** Parabolic trough-shaped (PT) mirrors concentrate the solar radiation on the outer cylindrical surface of a linear tubular receiver, located all along the focal line of the parabolic channel - see Figure 2.7a [21]. Indeed, as it was already mentioned in Section 2.2.2, the PT geometry allows the incoming rays parallel to the axis of the parabola to be reflected *ideally* towards a single point, the focus, as clearly shown in Figure 2.7b (readapted from [24]). The fluid passing inside the tubular external receiver is thus heated up for eventual further uses such as electrical power generation through high pressure superheated steam generation heat transfer units and following Rankine power cycles [17] or intermediate thermal storage through high temperature molten salts insulated tanks [17, 18]. A sun-tracking system is moreover used to allow the mirrors to follow the sun radiation direction [24]. According to the present technical limitations related to the thermal oils used today inside the receiver, the thermal energy of such systems can be delivered at up to roughly 400°C [17, 18]. This technology is currently the most widely used [17, 24]: at September 2010, parabolic trough power plants provided more than 90% of the total CSP capacity, in operation or in construction [24]. As examples of real PT systems, the 150 MW Andasol Solar Power Station, in Spain, the first CSP commercial plant in Europe using this type of CSP technology, saves roughly 149000 tonnes of CO<sub>2</sub> emissions per year with respect to a modern coal power plant [18], whereas the Solana plant, in Arizona, avoids roughly 427000 tonnes of CO<sub>2</sub> every year [18].

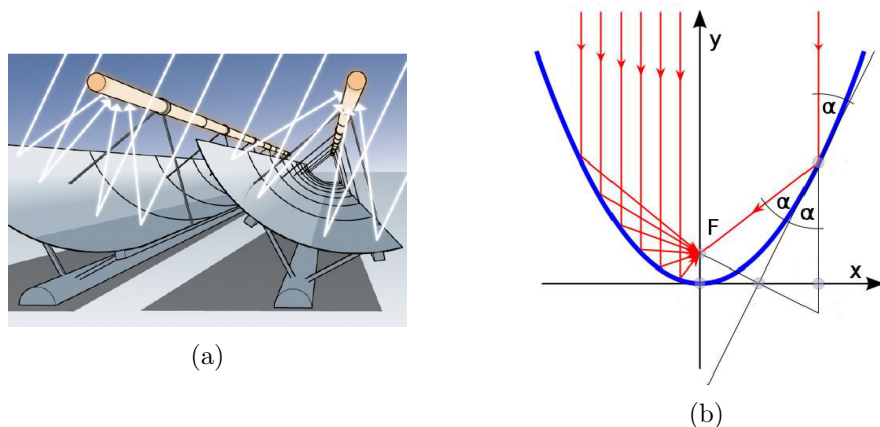


Figure 2.7: (a) Scheme of a parabolic trough system [21]; (b) PT geometry and ideal path followed by the incoming rays [24].

**ii.** In a central tower (CT) (or central receiver (CR)) system a field of reflecting mirrors - heliostats - redirects and concentrates the sunlight onto a receiver, located at the top of a central tower, as schematized in Figure 2.8. Each heliostat individually tracks the sun [18]. Typical concentration ratios are of 600 to 1000, allowing to reach temperatures even higher than 800-1000°C [18]. These high temperatures can drive not just steam cycles, but even gas turbines and combined cycles, with solar-to-electric peak efficiencies in this latter case up to 35% and annual values up to 25% [18]. Also in this typology, TES is typically performed, and smaller storage volumes compared with the PT systems are sufficient, for a given amount of energy stored, thanks to the higher temperatures reached. A CT station can implement both an external tubular receiver, as for the Gemasolar plant, in Spain, or a cavity receiver, as in Planta Solar plants PS10 and PS20,

again in Spain. The CO<sub>2</sub> emissions avoided thanks to the Gemasolar station are of roughly 30000 tonnes per year [18].

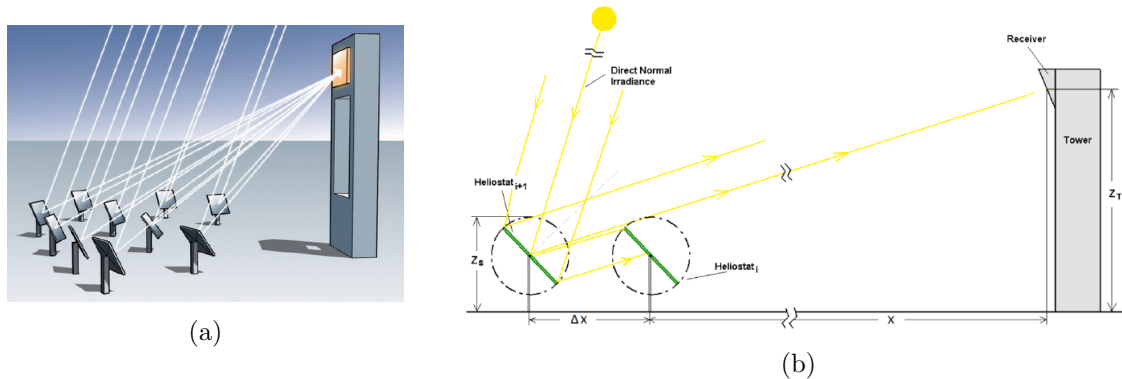


Figure 2.8: (a) Scheme of a central tower system [21]; (b) CT geometry and radiation path.

**iii.** Linear Fresnel (LF) systems exploit the Fresnel lens principle, valid also for mirrors, according to which a continuous reflecting surface can be *chopped* in a series of smaller planar surfaces that have together the same - or a very similar - optical effect as the original optical element. In this sense, a parabolic trough mirror can be optically approximated through a linear Fresnel mirror composed of linear reflecting segments, as shown in Figure 2.9a. A LF system has a lower solar-to-electric efficiency compared with PT, but on the other hand is cheaper, simpler to construct and allows for a more efficient land use [25]. LF mirrors have actually a small curvature obtained by mechanical bending [25]. The most relevant difference at the receiver level is that a secondary concentrator is used to increase the concentration. A compound parabolic shaped secondary concentrator (CPC) is shown in Figure 2.9b, where radiation coming from the mirrors is once again reflected before reaching the cylindrical absorber. Steam is typically used as working fluid, with the possibility of direct steam generation, as happens in the Puerto Errado 2 (PE2) 30 MW LF plant, in Spain: this solar station avoids roughly 16000 tonnes of CO<sub>2</sub> emissions every year [18].

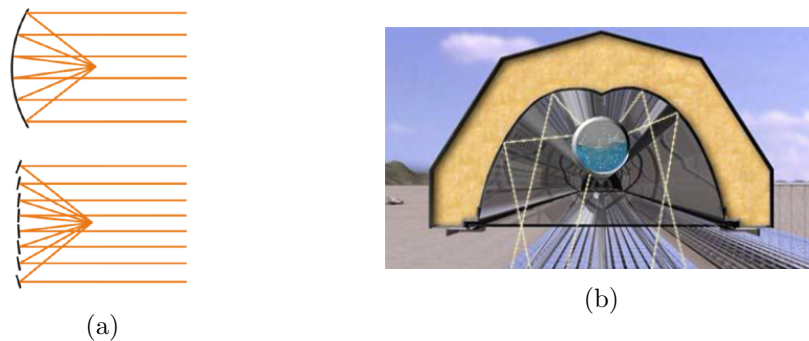


Figure 2.9: (a) Linear Fresnel mirror (bottom) approximating a parabolic trough mirror (top) [25]; (b) Compound parabolic shaped secondary concentrator [25].

**iv.** Solar dish (SD) CSP systems use paraboloidal dish mirrors to concentrate the solar radiation onto a receiver placed in the focus of the dish. Here, the radiation is absorbed and transferred either to the eventual heat transfer fluid in case of electricity production or to the thermochemical process of interest to drive some endothermic chemical reactions, as will be more deeply explained later on.

As already said, solar dish are ideally point-focusing systems. This leads to very high concentration ratios, that on their turn imply very high temperatures and thus very high efficiencies: dish systems have indeed the highest optical efficiencies and the highest overall conversion efficiencies among all the CSP systems currently available [17], having reached a solar-to-electric efficiency of 30% [17]. Other relevant advantages of such a technology are flexibility and modularity: dish systems are suitable both for stand-alone and small scale installations or for large scale installations, thanks to the possibility to implement a large number of dishes in a solar park [26]. Several mirrors are collected and mounted on a supporting structure [27]. Moreover, high power densities, good behaviour against moisture effects and a long lifetime are observed [27]. A solar dish is typically directed towards the sun through a biaxial tracking control system [17, 27]. A major fraction of commercial dish systems nowadays deals with electricity production through using Stirling engines [17, 27], although they can be used as said also for other CSP applications. Figure 2.10a [27] shows the typical scheme of a dish system, while Figure 2.10b [28] is a picture of the solar dishes at White Cliffs, Australia.

Summarizing, the main elements of a solar dish system are a paraboloidal concentrator, a receiver (i.e., the solar heat exchange unit), a tracking system for pointing the sun and optionally - according to the application - an engine-generator unit [17]. Typical concentration ratios for a solar dish are between 1500 and 4000, while the diameter ranges from 1 m to 25 m [17]. The radiation is only ideally focused onto a single point (i.e., the focus): in the reality, being the solar radiation spread in a cone of aperture  $\theta_s$  (see previous sections), and being the mirrors not perfectly reflective surfaces, then the actual focus is a finite region around the geometric focal point, with the highest flux near the center and decreasing intensity going to the edges [17]. Moreover, as a consequence of the previous considerations about optical and thermal losses, the receiver aperture area has to be optimized, in order not to be too large and thus causing excessive thermal losses because of the large external area, and in order not to be too small thereby causing excessive optical losses because of a higher amount of spilled rays. In SD systems both an external receiver or a cavity receiver can be used, as schematized in Figure 2.11 [29], although the cavity configuration is the most used one for high temperature applications because lower radiative and convective heat losses occur [29].

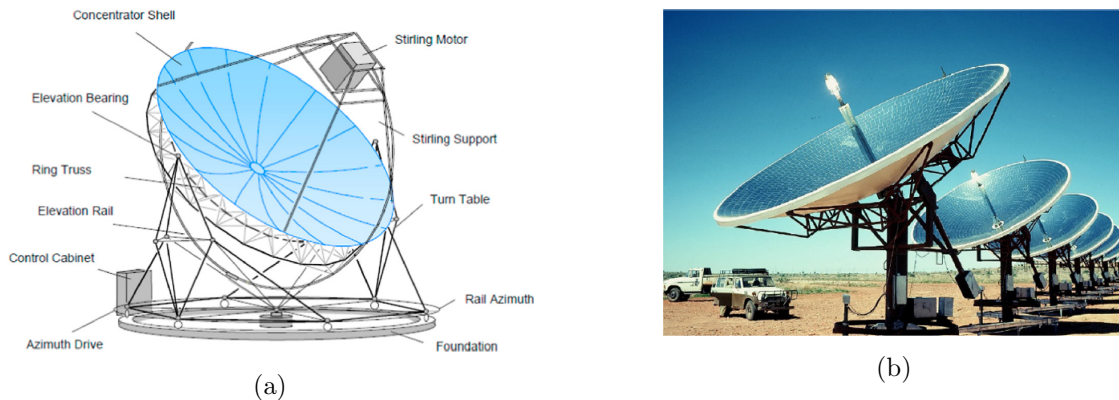


Figure 2.10: Solar dish systems: (a) Diagram of EURODISH system, as reported in [27]; (b) Solar dishes at White Cliffs [28].

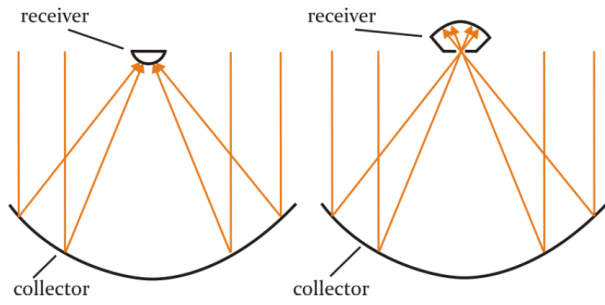


Figure 2.11: Scheme of external (left) and cavity (right) receivers for SD systems [29].

### 3 Solar thermochemical processes for hydrogen and syngas production

#### 3.1 A general overview

In this section, the attention will be focused in particular on the *solar* thermochemical processes, usually driven by high temperature heat coming from concentrating solar power (CSP) facilities. Thermochemical processes include all the processes that need high temperature heat to drive specific chemical reactions. RES-based SR facilities, biomass gasification or pyrolysis, thermolysis and thermochemical cycles belong to this category. Even in this case, the aim could be to produce either just hydrogen or instead a syngas that will be used e.g. as platform molecules mixture for further chemicals production. A fairly exhaustive classification of such processes is reported in Figure 3.1 [30]. From the scheme, it can be noticed that also other branches appear, such as all the industrial applications, that are not useful for the aim of the present analysis. As already mentioned above, several known processes are included: reforming processes (both steam and dry ones). Note: the renewable nature of the process lies here in the CSP feeding. The SR of fossil sources should be conceptually kept separate from the RES-based classification described here), coal and biomass gasification (Note: the RES-based nature in the scheme refers also here to the CSP feeding. For the process to be renewable as a whole, only the biomass should be considered) or direct solar thermolysis of water. A consistent branch is the one of thermochemical cycles, that will be the core of the following analyses.

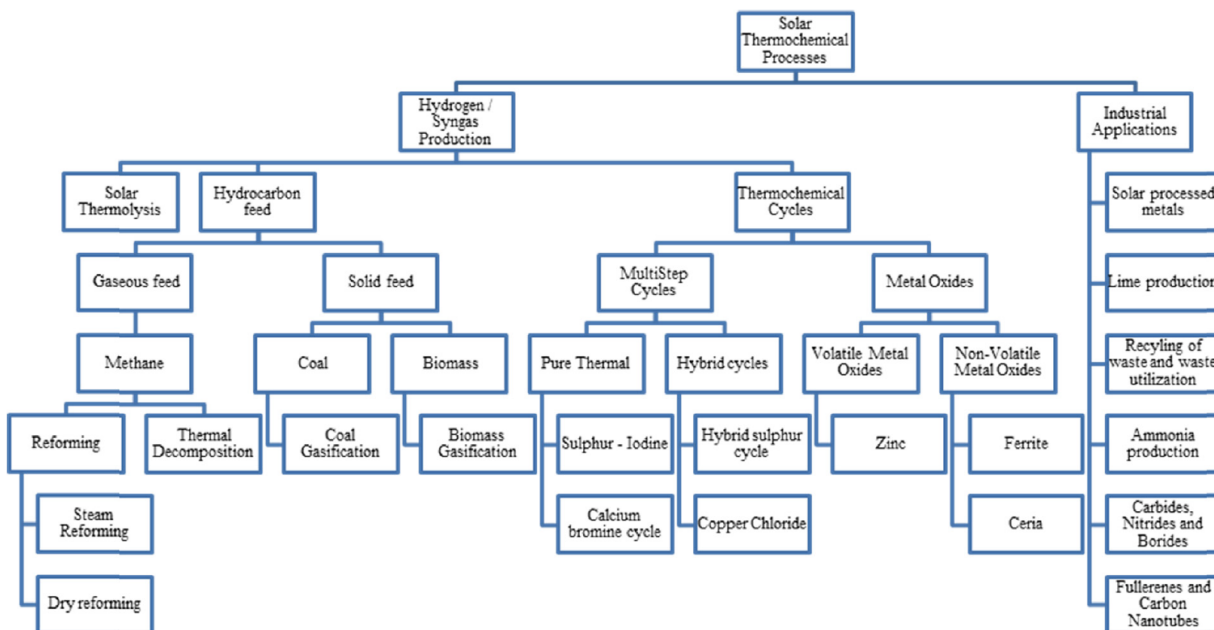


Figure 3.1: Classification of solar thermochemical processes [30].

As can be observed, a major portion of the scheme in Figure 3.1 is covered by hydrogen/syngas (i.e., solar fuels) production processes. Considering this subset of procedures, another interesting picture is given in Figure 3.2 [4], in which the main routes for CSP-aided thermochemical solar fuels production are shown. The paths shown are basically the same given in Figure 3.1: thermolysis, thermochemical cycles, reforming, cracking and gasification indeed appear as the five pathways viable. For the three latter alternatives, being these ones starting from fossil fuels, there is the

possibility for carbon dioxide capture and utilization or sequestration (storage). Let's notice that, in principle, even the  $\text{CO}_2$  indicated as a starting point at the top of the picture could come of course from carbon capture facilities.

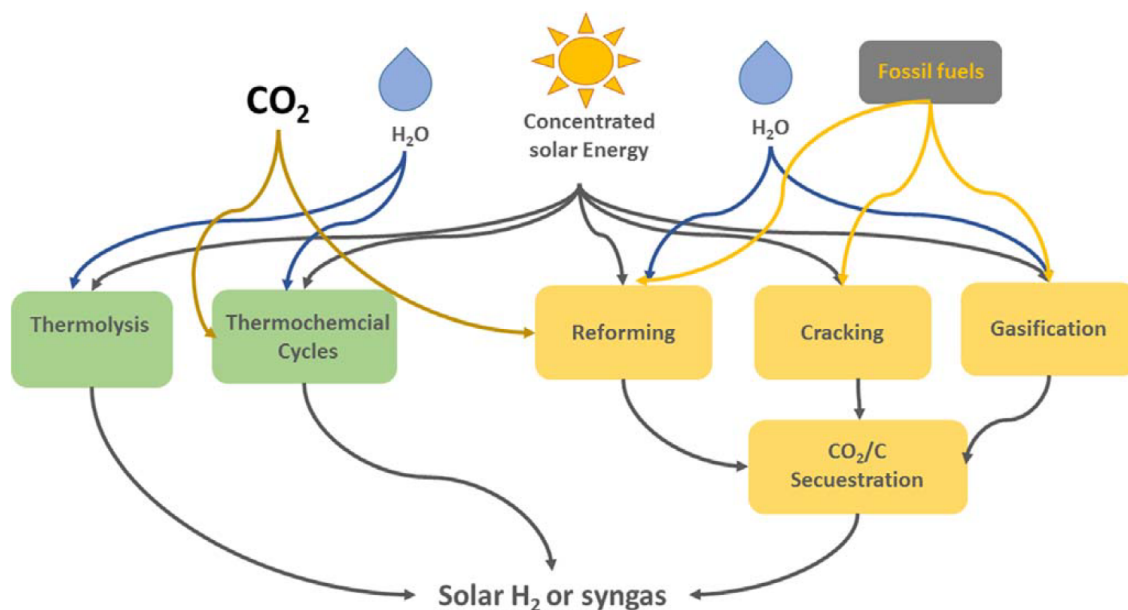
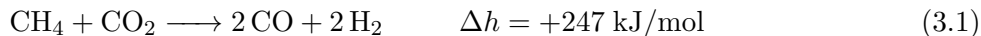


Figure 3.2: Main routes for CSP-aided thermochemical solar fuels production [4].

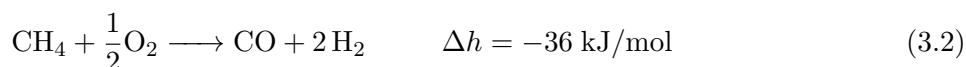
As can be observed, the energy input is fed as high temperature radiant heat through a CSP system for all of them, whereas the mass inputs are  $\text{H}_2\text{O}$  for thermolysis,  $\text{H}_2\text{O}$  and  $\text{CO}_2$  for thermochemical cycles,  $\text{H}_2\text{O}$ ,  $\text{CO}_2$ , hydrocarbons such as  $\text{CH}_4$  or other feeds such as biogas for reforming reactions,  $\text{H}_2\text{O}$  and fossil fuels for cracking reactions, and  $\text{H}_2\text{O}$  and fossil fuels or biomass for gasification. Being the thermochemical cycles route the one of interest for the following parts, it is worth now to mention the main differences that exist between this possibility and the other thermochemical options, in order to have an idea of the *pros and cons* associated to the different methodologies: for this reason, some information will be quickly given on the four alternatives presented above, and then thermochemical cycles will be more deeply described.

i. *Direct thermolysis* of water consists in heating it up to a sufficient temperature so that the thermal dissociation can take place in a useful amount. The dissociation reaction is exactly the same as Reaction 1.3, with the difference that here it is thermally driven. The process is reversible, and it is fundamental to prevent the products to recombine to form water again [43]. There are two main problems associated with this process. The first issue are the ultra-high temperatures needed for obtaining acceptable dissociation results: it has been estimated indeed that  $\Delta G$  for the dissociation reaction equals zero at roughly 4300 K [30, 31]. Furthermore, at 2500 K and 1 bar, less than 3% of the water actually dissociates yielding hydrogen [30]. Thermodynamic conditions needed are thus very challenging and not convenient at present, also because adequate materials have not been yet really found out [30]. The second relevant issue relates to the separation of hydrogen and oxygen after the water molecule decomposition, being this mixture potentially explosive [30]. Several solutions have been proposed at this aim, both as direct separation methods at high temperatures and as quenching coupled with low temperature separation [30, 43]. Thus, although this process could appear as attractive at glance because of its conceptual simplicity due to the one-step nature, several technical challenges should be first faced.

ii. *Reforming* process, that can be in general carried out through steam - case of *steam reforming* - or through CO<sub>2</sub> - case of *dry reforming* - has been already mentioned above for the relevant case of NGSR (i.e., natural gas steam reforming). For completeness, the dry reforming (DR) reaction for methane, to be conceptually coupled with Reaction 1.1, is reported here below:



However, the DR process is not used in the industrial sector [2], because of several drawbacks with respect to the methane SR, in particular regarding the following three aspects: (1) the H/C ratio in the DR-derived syngas is equal to 1, against the value of 3 for SR, and this is not good under the hydrogen productivity point of view; (2) DR is even more endothermic than SR, and this would imply more heat to be supplied; (3) finally, also CO<sub>2</sub> is needed. For sake of completeness, it is here cited also a third alternative for producing hydrogen: the *partial oxidation* reaction (POX), reported below:



In this case, the H/C ratio is 2, so also here the syngas has a lower quality than in SR, although it is not necessary to sustain thermally the process, being the reaction exothermic. Thus, what has been said here and above about the three alternatives to produce hydrogen/syngas (SR, DR and POX) starting from methane justifies the main industrial choice nowadays to follow the NGSR path. Even in DR case, however, the heat is mainly delivered by burning natural gas (Note: DR substitutes just the SR step in the production chain. The WGS and the following passages remain exactly the same as described previously). Going back to the general discussion about reforming processes, it would be a good solution to follow a RES-based pathway, such as a reforming process in which the energy input is not the chemical energy released from natural gas combustion, but instead is concentrated solar power heat, that is the case of interest in this descriptive review. In this case, the natural gas would be just the mass feed treated in the process. Such a path could be a transition solution, since performing the SR or DR reactions in a solar-aided way avoids to reach the high temperatures needed through burning fossil fuels [22]. Some investigations have been performed also as concerns reforming of biogas, in which case a possible mixture of both water and carbon dioxide as reforming agents has been considered [4, 22].

iii. *Cracking* process, typically applied to hydrocarbons, consists in breaking up heavier molecules, thus obtaining smaller ones [4]. Even in this case, the *leading actor* is basically methane, for which CSP-fed cracking has been explored [4]. The general reaction for hydrocarbon cracking is the following [4]:

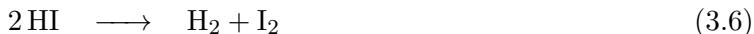
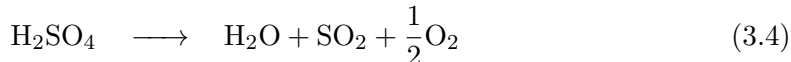


The aim of such a process is actually to produce H<sub>2</sub>, trying to avoid CO<sub>2</sub> emissions into the atmosphere [4].

iv. *Gasification* consists in general in converting a solid carbonaceous feedstock, such as coal or biomass, into a gaseous fuel, simpler to be handled, transported and used in the downstream technologies. Coal gasification is a well-established process, involving, in the standard solutions, a partial oxidation of the input feedstock in such a way to furnish the heat needed to the process, that has to be carried out between 800 and 1500°C [4]. However, if RES-based processes are considered, then just biomass is a possible candidate. Biomass gasification is technically more complex, and involves several reactions, both homogeneous (gas-gas) and heterogeneous (gas-solid carbon). Even in this case, the process is endothermic, and thus heat has to be supplied. In conventional biomass gasification, as for coal, the high temperature heat needed is delivered through the input biomass itself through partial oxidation reactions, although the typical temperatures are lower (800-850°C)

because of the higher oxygen and moisture content. If concentrated solar power is instead used to drive the endothermic gasification reactions, several advantages can be observed, first among all (1) a reduction in the CO<sub>2</sub> emissions up to 30% and (2) higher yields of syngas per unit of biomass, because there is no need for burning part of it to provide the process heat, since it comes from concentrated solar radiation [4].

v. *Thermochemical cycles* are the fifth category of processes analysed in this review, and the most interesting ones for the aim of the present work. It does make sense to report some motivational hints that justify the development of thermochemical cycles processes. The two relevant issues related with direct water thermolysis mentioned above are indeed overcome through this sub-family of processes. The technology available today allows in fact to perform such cycles at temperatures well lower than the ones required by thermolysis. Moreover, in this case hydrogen and oxygen are produced in separate stages, thereby eliminating also the issue related to the explosive mixture separation. The main advantage with respect to reforming, cracking or gasification is instead that no hydrocarbons feed is needed, rather conversely CO<sub>2</sub> can be used as mass input to the process, thereby allowing a net capture and a net reduction of such emissions. Thermochemical cycles, also referred to as a subset of the *chemical looping* processes, are indeed by definition loops of chemical reactions in which water, carbon dioxide or both are typically splitted to yield respectively hydrogen and carbon or carbon monoxide. Temperatures usually required are of the order of 800 to 2100 K. Chemical looping processes are further classified as *multi-step* (MS) cycles and *metal oxide redox pair* (MORP) based cycles. MS cycles can be defined as all those cycles able to produce hydrogen at around 1000 K and involving three or more chemical reactions steps. MORP based cycles involve instead redox materials, typically metal oxides, that undergo cyclic reduction and oxidation steps, in which oxygen and hydrogen are respectively released. Thus, the multiple oxidation states exhibited by the given metal are exploited. MS and MORP cycles operate at different temperature levels, with a kind of threshold value of roughly 1200 K [30]. MS operate typically below this level, and they can be fed e.g. by nuclear reactors, while higher temperature requirements of MORP can be reached only through a solar feeding. MORP cycles are inherently simpler than the MS ones because of the two-steps nature. A MS cycle reported here as an example is the Sulfur-Iodine (SI) one, that works according to the following reaction mechanisms [2]:



It is thus a 3-steps cycle used for hydrogen production, in which sulphuric acid is processed. The reactions above occur in three different dedicated "blocks", that will be referred to for simplicity as blocks 1, 2 and 3, respectively. In particular, Reaction 3.4, conducted at roughly 850°C, is the one fed by solar radiation, and oxygen is released here; Reaction 3.5 needs water from the external: here, SO<sub>2</sub> coming from block 1 and I<sub>2</sub> coming from block 3 react at around 100°C to yield H<sub>2</sub>SO<sub>4</sub>, sent to block 1, and HI, sent to block 3; finally, Reaction 3.6, developing at 200 to 700°C, converts the HI coming from block 2 into I<sub>2</sub>, sent back to block 2 again, and H<sub>2</sub>, that is the useful product of the loop. Besides the MORP's inherently simpler nature, the SI loop example is useful also for understanding another advantage of MORP cycles with respect to MS ones: the formers are indeed suitable not just for splitting water, but also carbon dioxide (splitting mechanisms can be found in Reactions 3.11 to 3.14 below), allowing for treating even CO<sub>2</sub> and thus producing syngas as useful product. The steps describing the simple working principle of MORP follow:

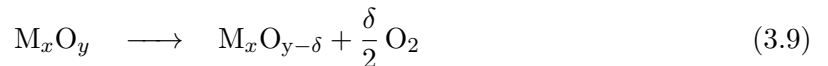
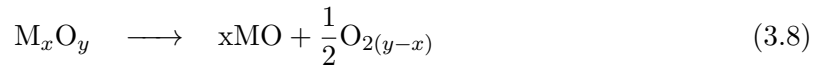
- o. The chemical loop is fed by high temperature heat, that in this framework will be solar heat

from a CSP system. The temperature level has to take into account also the material used in the loop. This heat is delivered to the higher temperature step of the cycle;

- i. The higher temperature step is the endothermic *reduction* reaction. The metal oxide at the higher oxidation degree is thermally reduced thanks to the high T heat received, thus delivering a metal oxide at a lower oxidation degree and O<sub>2</sub>. A further and deeper subdivision for the MORP loops is the following [32]:

- (1) Volatile stoichiometric;
- (2) Nonvolatile stoichiometric;
- (3) Nonstoichiometric (typically nonvolatile).

In a volatile MORP cycle (i.e., item (1)), the temperature needed for the thermal reduction step is higher than the vaporization temperature of the metal oxide, thus leading to a solid-to-gas transition [32]. Some examples are the redox pairs ZnO/Zn and SnO<sub>2</sub>/SnO [32]. In nonvolatile stoichiometric and nonstoichiometric cycles (i.e., items (2) and (3)) the metal oxide maintains the solid state, and no transitions occur [32]. An example for item (2) is the pair Fe<sub>3</sub>O<sub>4</sub>/FeO, while some examples for item (3) are the nonstoichiometric ceria or perovskites structures of the type ABO<sub>3</sub>, such as LaMnO<sub>3</sub> [32]. Furthermore, nonvolatile stoichiometric reactions are characterized by a change in the solid crystal structure, while nonstoichiometric reactions maintain the original crystallographic structure [32]. In other words: nonvolatile stoichiometric pairs form solid solutions during reduction, as happens for the pair Fe<sub>3</sub>O<sub>4</sub>/FeO, in which just a portion of Fe atoms reduce from 3<sup>+</sup> state to 2<sup>+</sup> state, whereas nonstoichiometric pairs structure does not change even if the lattice is accomodating some changes in ions vacancies concentrations [34]. Some reference reaction mechanisms follow, with Eqs. 3.7, 3.8 and 3.9 reporting respectively some possible characteristic reactions for items (1), (2) and (3) above [2, 30, 32]:



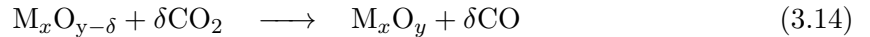
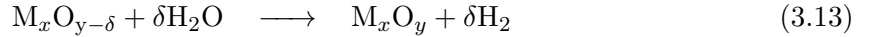
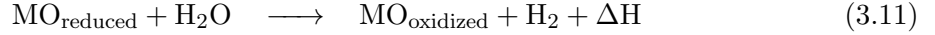
The reaction 3.8 is frequently written with  $x = 3$  and  $y = 4$ , since some relevant examples (such as the abovementioned pair Fe<sub>3</sub>O<sub>4</sub>/FeO) belong to this particular case of wüstite/spinel phases transition [33]. The volatile stoichiometric mechanism is very effective, because being the metal more strongly reduced, it will be able to accept a higher amount of O<sub>2</sub>. On the other hand, however, this type of reduction needs very high temperatures, so problems related to the concentrator and to the receiver materials could arise. In the case of ZnO/Zn cycle, the decomposition temperature of ZnO is indeed of roughly 2300 K, against a melting point of 692 K and a boiling point of 1180 K [6]. In the case of the Zn cycle, since the metal passes to the gaseous state, then a quenching is needed to avoid the recombination with the oxygen just after the reduction step, while in the hydrolysis oxidation step it is necessary to use nanoparticles of Zn to sufficiently enhance the reaction kinetics [33]. As reference values, a maximum solar-to-chemical theoretical efficiency for the Zn cycle realizing CDS equal to 39% has been estimated [45]. The nonstoichiometric mechanism is less effective in terms of oxygen removal, but it has the advantage to be carried out at lower temperatures. As further reference values, the reduction temperature for the abovementioned SnO<sub>2</sub>/SnO cycle

and for the  $\text{GeO}_2/\text{GeO}$  cycle, both volatile, are respectively around 1873 and 1673-2073 K, while around 1773 K for the nonstoichiometric ceria cycle [6, 32]. An interesting possibility for carrying out the reduction step at lower temperatures is to combine it with methane reforming, according to Reaction 3.10:



This option allows thus to reduce the temperature swing between the two steps and to produce a further syngas stream even in the reduction reactor. This option has been explored e.g. for the cerium oxide based cycles;

- ii. The lower temperature step is the exothermic *oxidation* reaction. The metal oxide at the lower oxidation degree is now oxidized again to produce  $\text{H}_2$  and/or  $\text{CO}$ , starting from water and carbon dioxide, according respectively to the following *water splitting* (WS) and *carbon dioxide splitting* (CDS) reactions, reported below both as generally valid qualitative reactions (i.e., Reactions 3.11 and 3.12 [6], in which MO stands for the metal oxide) and specifically for the nonstoichiometric case (i.e., Reactions 3.13 and 3.14 [32]):



$\Delta\text{H}$  is the enthalpy of reaction. The output obtained, both in case of pure  $\text{H}_2$  or pure  $\text{CO}$ , or in case of a syngas mixture, can be further used downstream for different purposes, as already mentioned, such as direct combustion, electrochemical oxidation or as platform molecules for subsequent processes, such as production of chemicals or hydrocarbon fuels through Fischer-Tropsch processing [32]. Some reference values for the oxidation step temperatures are around 873 K for the  $\text{SnO}_2/\text{SnO}$  cycle, below 1000 K for the  $\text{GeO}_2/\text{GeO}$  cycle and between 873 and 1273 K for the nonstoichiometric ceria cycle [6, 32].

The MORP approach is simple since the high temperature reduction step is actually the same for WS and CDS. Being the metal oxide recycled back in the loop, then the overall resulting reactions are the conversion of  $\text{CO}_2$  in  $\text{CO}$  and of  $\text{H}_2\text{O}$  in  $\text{H}_2$  with a net release of  $\text{O}_2$ , that is collected at the higher T step. The quantity  $\delta$ , referred to as *oxygen exchange capacity* [32] or *oxygen storage capacity* [34], represents the deviation from stoichiometry, and it is directly linked to the maximum amount of fuel that can be produced, and thus also to the conversion efficiency from solar energy to stored chemical energy [32, 34].

The following part (Subsection 3.2) will give some information on the reactors and facilities used for CSP driven thermochemical cycles for solar fuels production.

### 3.2 CSP-fed solar reactors for solar fuels production through thermochemical cycles

This subsection will deal with the coupling of CSP facilities with thermochemical processes, in the case with thermochemical cycles, for hydrogen or syngas production. This strictly technical part completes the general overview of solar fuels production processes given in Subsection 3.1, in which the main pathways viable at this aim have been described. Herein, a brief review on the

research path for testing a solar chemical process and a description of the typologies of reactors for thermochemical cycles applications will be mentioned.

As a general framework, in a research perspective, a solar thermochemical process is typically first tested in an indoor environment through a so-called *high flux solar simulator* (HFSS), that is able to artificially provide a concentrated radiation source coherent with the spectral distribution of the sun, and then demonstrated using a *solar furnace* fed by actual solar radiation [30]. A solar furnace is an optical system consisting in a heliostat with automatic sun tracking, that redirects the solar radiation towards a stationary concentrator, which on its turn reflects the concentrated radiation to the focal point of interest [4, 30]. Since the sun tracking is carried out by the heliostat and the concentrator is stationary, it is very effective to control the experiments. A solar furnace can have an on-axis or off-axis configuration: in the on-axis case, the focal point is located between the heliostat and the concentrator. This allows to have a symmetrical beam distribution towards the focal point and so a better optical performance, but some radiation is blocked by the receiver itself. In the off-axis case, the radiation is not blocked out, but the optical efficiency will be lower, because of the asymmetric distribution of radiation towards the reactor [30]. A shutter element can be foreseen to attenuate solar radiation [30]. Figure 3.3 shows an example of HFSS [30], while Figure 3.4 [30] gives a schematic representation of on-axis (left) and off-axis (right) solar furnaces.



Figure 3.3: High flux solar simulator, German Aerospace Center (DLR), Germany [30].

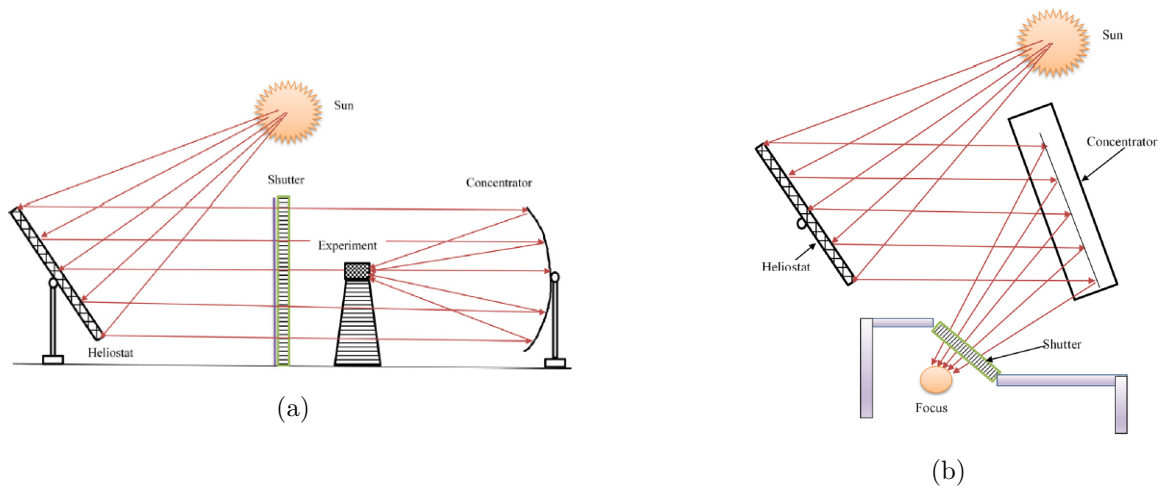


Figure 3.4: Solar furnaces in (a) on-axis and (b) off-axis configurations [30].

Let's stress that, from now on, the general *receiver* notion in the CSP framework will be replaced by the *solar reactor* (or *receiver-reactor*) one: the heat will be thus delivered as concentrated radiant power to a chemically reactive environment, and not just to a pure heat transfer unit, in order to drive the chemical reactions of interest and to deliver hydrogen or syngas. The solar energy is stored in chemical form inside the chemical bonds of the output fuels.

In Subsection 3.1, five main solar fuel thermochemical routes have been identified: direct water thermolysis, thermochemical cycles, reforming, cracking and gasification (see Figure 3.2). All these processes have to be coupled with proper solar reactors to be carried out, but here the attention will be focused just on reactors for the thermochemical cycles path. The high temperatures needed for MORP loops feeding (even up to 2300 K [6]) can be reached only through very high concentration ratios, and thus through solar dishes or solar tower plants [6]. Practically, a given redox material and a given reactor can be used either for producing two separate streams of H<sub>2</sub> and CO or for producing both of them simultaneously, if H<sub>2</sub>O and CO<sub>2</sub> are co-fed to the system. The reference chemical mechanisms for the high temperature and low temperature steps are the ones reported in Reactions 3.7 to 3.14.

In Subsection 2.1 several ways to classify CSP receivers have been proposed: let's keep in mind here for convenience the differentiation in Indirectly Irradiated Receivers (IIRs) and Directly Irradiated Receivers (DIRs). The comparison that arises is the one among traditional (i.e., not solar-aided) chemical engineering (TCE) and solar chemical engineering (SCE). TCE has to be conceptually combined with CSP-related knowledge in order to obtain suitable technical solutions at this aim. The way in which a MORP cycle works resembles indeed the catalytic gas reactions that take place on a solid catalyst in TCE framework. For this reason, a similar grouping of catalytic reactors coming from TCE can be used, according to whether the catalyst particles are randomly distributed in space or arranged in a sort-of-ordered fashion. These two categories are referred to respectively as *non-structured* and *structured* reactors. Some examples are packed or fluidized beds reactors for the first group, and honeycomb or foam reactors for the second group [6]. Both non-structured and structured designs can be translated from TCE to SCE, and in both direct and indirect irradiation configurations: following the same nomenclature, the IIRs become IIRRs (indirectly irradiated receiver-reactors) and the DIRs become DIRRs (directly irradiated receiver-reactors). It is however trivial that there will be some technical differences passing from TCE to SCE. The main two ones to be taken into account are the following:

1. While in TCE the initially colder catalyst is usually heated up by the hot reactant gases, in SCE it is the solid phase (i.e., the metal oxide) that is absorbing the solar radiation and has to heat up the reactant gas species up to the reaction temperature needed;

2. In SCE, the solid phase (i.e., the metal oxide) is not just a catalyst, but it is a reactant itself. This implies that even the metal oxide has to reach the reaction temperature, and that it has to be replenished or regenerated in some way during the operation.

Besides these two aspects, also several other issues could be mentioned, for instance related to the thermal and chemical conditions that all the materials involved (both the reactor and the redox ones) have to face, evaporation of volatile compounds, loss of reactant, changes in composition or side reactions involving the reactor materials [6]. Further relevant aspects to be considered are the "temperature swing" operation between reduction and oxidation and the issues related to the high temperature heat recuperation [6]. Indeed, as previously said, the two MORP steps are favoured by different thermodynamic conditions, namely high temperature and low oxygen partial pressures for the endothermic reduction, whereas low temperatures and high water/carbon dioxide partial pressures for the exothermic oxidation. The two steps occur typically in the respective ranges of 1600-1900 K and 1000-1300 K, and the thermal swing for the entire cycle can be considered to be around 400 K [6]. This temperature oscillation has to be handled both for the reactor itself

and for the redox material used. As concerns the heat recuperation, it is important to not reject the high temperature heat at the reduction step, because this would induce a drastic decreasing in the efficiency of the system [6]. Just few examples of IRRs have been actually proposed because of issues regarding the tubes material temperature and thus the maximum heat flux achievable, thus the major part of receiver-reactors employed are of DIRR type [6]. In this case, a transparent window is used for allowing the radiation to enter the reactor and isolating the reacting site from the ambient air. Another classification already proposed and that has to be reminded here is the distinction among volatile and nonvolatile MORP cycles. In the volatile case, a gaseous mixture of reduced metal or metal oxide and oxygen forms, and this leads to the need of managing their possible recombination. This issue is the reason why in the volatile MORP cycles two separate reactors have to be used for the reduction and oxidation steps, and the cyclic operation is splitted typically in a diurnal thermal reduction phase and a nocturnal oxidation and syngas production phase. The lower temperature splitting can be indeed even fed by a not-solar feeding. Since this problem does not subsist for nonvolatile cycles, in this case the reactors are usually designed instead for performing both the cycle steps [6]. The reactors used so far for redox cycles are summarized in Table 3.1 [6].

Heat transfer concept	Redox cycle							
	Volatile cycles (only TR cycle step)				Non-volatile cycles (both cycle steps)			
	Reactor concept							
	Non-structured reactors		Structured reactors		Non-structured reactors		Structured reactors	
	Movement							
Non-moving particles	Moving particles	Non-moving structures	Moving structures	Non-moving particles	Moving particles	Non-moving structures	Moving structures	
Directly-irradiated		Rotating cavities		Moving fronts	Packed beds	Spouted beds	Honeycombs	Rotary cylinders
		Entrained beds				Moving beds	Foams	Rotating fins
Indirectly-irradiated		Aerosols	Sintered plates		Packed beds			

Table 3.1: Solar reactors employed for performing WS/CDS thermochemical cycles [6].

The majority of solar reactors performing both cycle steps - thus the ones used in principle for all the nonvolatile redox pairs - are DIRRs, both using powders or well-ordered structures, and can be distinguished according to whether there are or not parts in movement. The technical solutions have to deal with the different thermal and chemical requirements of the two cycle steps. Both a continuous production and a batch production can be realized: in the continuous mode, reactive particles or structures are moved through two different zones of the reactor, managed at different temperature levels with solar radiation hitting at least the reduction zone, and irradiation and gas streams can be supplied in a continuous way; in the batch mode, there is just one single reaction zone, thereby avoiding any solid transport, and both irradiation and gas streams (and thus the chemical atmosphere in the reacting site, i.e., reducing or oxidizing one) are regulated/adjusted in order to achieve the optimal temperature conditions of the corresponding cycle phase in place.

## 4 Literature review on thermochemical cycles

This part will report a literature review on the thermochemical cycles of interest, in order to have a benchmark for the results achieved later in the present work. Subsection 4.1 will deal with the cerium oxides based thermochemical cycles, whereas Subsection 4.2 will be devoted to the iron oxides based thermochemical cycles. Both general information on such cycles and some relevant experimental results previously achieved will be mentioned. These two examples of cycles are among the most studied so far. A comparison between them does make sense because they belong to two separate typologies of cycles, namely to the nonstoichiometric as concerns the cerium-based ones, and to the nonvolatile stoichiometric as concerns the iron-based ones. Generally, it is reported that nonstoichiometric reactions have higher chemical and morphological stability and faster reaction kinetics, but on the other hand they allow for a lower oxygen storage capacity [34]. The results of the present analysis can be thus compared both under a literature point of view and among themselves.

### 4.1 Cerium oxides based thermochemical cycles

Among the MORP thermochemical cycles proposed so far, the cerium (IV) oxide ( $\text{CeO}_2$ ) based ones are for sure of great interest because of several appreciable characteristics of this redox material, such as suitable structural and chemical properties, high crystallographic stability during thermal processes, large oxygen capacity and ability to release and uptake it according to temperature and oxygen chemical potential changes [36]. Furthermore, the rapid reaction kinetics as concerns thermochemical redox cycles for solar fuels production has been documented [36, 37], as well as good friction resistance and mechanical strength [36]. Several possibilities have been investigated, namely a nonvolatile stoichiometric mechanism, a nonstoichiometric mechanism and using doped ceria as redox material. Some studies were devoted also to cycles implementing a methane-aided reduction. Each pathway has its own upsides and downsides. The stoichiometric cycle allows for higher yields with respect to the nonstoichiometric one, because a higher amount of lattice oxygen is being released, whence a higher fuel production per unit of metal oxide used. However, this result can be achieved only through very high temperatures, being the thermal reduction from  $\text{CeO}_2$  to  $\text{Ce}_2\text{O}_3$  complete over  $2000^\circ\text{C}$  [36, 37]. These temperature levels are difficult to be achieved in a continuous mode even for a concentrating solar power (CSP) system. Besides this, the stoichiometric mechanism involves the ceria being in the molten state during the reduction step, being its melting point below  $2000^\circ\text{C}$  according to some sources [37]. Melting a metal oxide is not the optimal solution, because e.g. of a possible vaporisation that can occur in the reaction site, with the eventual loss of some reactant and reduction of the amount available for the recycling in the loop [30], or because of a reduction in the surface area available for the reaction due to the solid-to-liquid transition. These issues shifted the interest towards alternative pathways, such as the nonstoichiometric mechanism or a methane-aided reduction step implementation. Several studies have been dedicated to the former case. Being the nonstoichiometric cycle performed below the ceria melting point [6, 30], then no transitions occur, and the practical issues mentioned can be avoided. Although the released oxygen yields are lower due to the lower temperatures, the advantage in this case is that consistent deviations from stoichiometry and thus oxygen removal extents can be anyway achieved without any change in the material's crystallographic structure, that in principle could lead to structural damages [6]. Even for the nonstoichiometric case, a good behaviour in terms of oxygen chemical diffusivity and kinetics has been observed. Apart from the nonstoichiometric mechanism, the second possibility that is being explored is the methane-aided reduction thermochemical cycle. In this case, the cerium oxide can be reduced at much lower

temperatures, allowing also for a reduction of the temperature swing in the loop or even for an isothermal operation [36]. In a RES-based perspective, biomethane as a renewable fuel could be for instance used at this aim. In the following, some previous experimental studies will be reported, in order to have a general idea on what has been done so far.

Figure 4.1 shows the crystal structure of ceria in its fully oxidized form ( $\text{CeO}_2$ ), around normal pressure and temperature (i.e., below the melting point). This type of structure is usually referred to as *fluorite phase*.

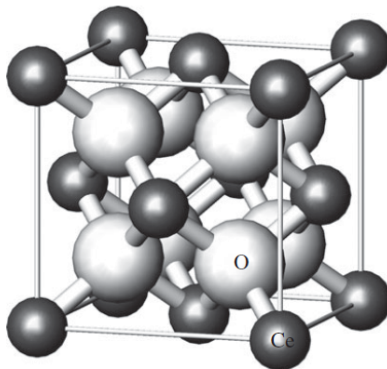
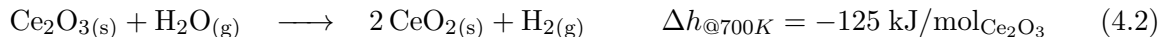


Figure 4.1: Crystal structure of fully oxidized ceria at normal pressure and temperature [33].

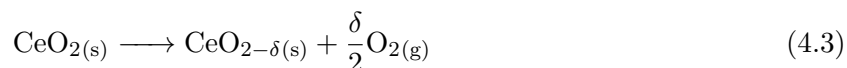
What happens at high temperatures, i.e., in reducing conditions, is that a fraction of Ce atoms pass from  $4^+$  oxidation state to  $3^+$  oxidation state, leading to oxygen release for balancing the charge and thus to formation of oxygen vacancies in the lattice. The amount of oxygen released depends upon temperature and oxygen partial pressure in the surrounding atmosphere, and it increases in general for higher temperatures and for lower oxygen partial pressures [33], as would be expected even from thermodynamic equilibrium considerations. These dependencies are of relevant importance, since, as mentioned,  $\delta$  is directly linked to the actual quantity of fuel that can be retrieved in each redox cycle and thus also to the system conversion efficiency.

The stoichiometric mechanism, identified and experimentally studied for the first time by Abanades and Flamant [37] in the early 2000s for  $\text{H}_2$  production, consists in the following reduction and oxidation reactions (4.1 and 4.2, respectively):



Cerium assumes the IV (or  $4^+$ ) oxidation state in  $\text{CeO}_2$ , and the III (or  $3^+$ ) oxidation state in  $\text{Ce}_2\text{O}_3$ . In that work [37], the reduction step was fed by solar energy, while the oxidation step was performed in a fixed bed reactor electrically heated. The authors report as an advantage of such cycle that there are not secondary reactions occurring and producing unwanted products. During the (solar) thermal reduction (Reaction 4.1) oxygen is released, while during the hydrolysis (i.e., oxidation, Reaction 4.2) hydrogen is produced. Coherently with the temperatures at which the enthalpies of reaction are reported, reference values to be considered are around  $2000^\circ\text{C}$  for the high temperature reduction step and around  $400\text{-}600^\circ\text{C}$  for the low temperature oxidation step, in case of only hydrogen production [37]. Since the melting point of  $\text{CeO}_2$  is around  $1950^\circ\text{C}$  according to some sources [37], then it melts during high temperature reduction phase. Abanades and Flamant [37] report that "the measured temperature before melting was  $1950^\circ\text{C}$ ", and "at

high temperature ( $T > 1950^\circ\text{C}$ ) [...] Ce(IV) was reduced during melting”. The reduction step was performed at constant pressures from 100 to 200 mbar, beyond which reduction was not observed, and temperatures higher than 2220 K, at which  $\text{CeO}_2$  was already in the molten state. The solar reactor used for the reduction step, shown in Figure 4.2a, assured controlled atmospheres, and a continuous flow of  $\text{N}_2$  as buffer gas through a vacuum pump was used in that case to achieve high mass transfers of  $\text{O}_2$  around the ceria sample, thus avoiding its recombination with the reduced phase. The pumping and the gas flow are also useful to prevent eventual deposition of ceria particles released by sublimation, that are then collected through a filter and recycled back. The  $\text{CeO}_2$  sample, placed on a water-cooled support, was exposed to solar radiation, redirected through a solar furnace, for a short time (2-6 min), depending on the initial mass used, in order to avoid sublimation. Moreover, writing the reduction reaction as follows,



then the reduction into Ce(III) results to be complete for a value  $\delta = 0.5$  [37] (that is, value for which the crystallographic structure of the sample completely converts to the  $\text{Ce}_2\text{O}_3$  one. Indeed, for  $\delta = 0.5$ ,  $\text{CeO}_{2-\delta} = \text{CeO}_{1.5} \equiv \text{Ce}_2\text{O}_3$ ). Although in the reference [37] the symbol  $x$  was used in place of  $\delta$ , it has been preferred here to be consistent with the nomenclature used in this work. In general, the composition written as  $\text{CeO}_{2-\delta(\text{s})}$  represents the averaged one in the sample. For  $0 < \delta < 0.5$ , the reduction is actually partial. Between the two *main* phases (i.e.,  $\text{CeO}_{2(\text{s})}$  and  $\text{Ce}_2\text{O}_{3(\text{s})}$ ), a great number of intermediate phases exists, and they can be predicted by thermodynamics [37]. In the work by Abanades and Flamant [37], the presence of such intermediate phases was not revealed. Thermogravimetric analysis (TGA) was used to determine the actual composition  $2 - \delta$  after the reduction step. TGA is a thermal analysis methodology allowing to measure the mass variation of a sample in time, as its temperature changes, as consequence of physical or chemical phenomena, such as solid-gas reactions, as happens in the present case. The main parameters monitored in a TGA procedure are thus mass, time and temperature. Indeed, in the reference work [37] described here, the reduced sample was heated up to  $400^\circ\text{C}$  for 2 h under ambient air, until the complete reoxidation towards  $\text{CeO}_2$  phase was achieved (that is, when the sample returned to show the initial white colour). Using the value of the mass gained during this reoxidation process, the  $\delta$  value for assessing the average after-reduction composition was determined. TGA results showed that almost complete reduction can be obtained for values of pressure of 100, 150 and 200 mbar: for a solar reduction exposition of 5 minutes, the mole fraction of the  $\text{CeO}_2$  phase was just 0.048, 0.332 and 0.076 respectively for the three increasing pressure values written above, with corresponding  $\delta$  values equal to 0.476, 0.334 and 0.462, so relatively very close to 0.5. Another result is that the necessary exposition duration must be longer than 2 minutes, otherwise a significant reduction rate is not achieved. As reference values, for a fixed pressure value of 200 mbar in the reduction reactor, a sample mass of 0.2731 g of  $\text{CeO}_2$  exposed to sun radiation for 3 minutes achieved a coefficient  $\delta$  equal to 0.493 (mole fraction of  $\text{CeO}_2$  equal to 0.014), whereas a sample mass of 0.4465 g exposed for 2 minutes achieved a coefficient  $\delta$  equal to 0.013 (mole fraction equal to 0.974). The factors that influence the reduction rate/extent are thus the mass of the sample, the pressure and the duration of the solar exposition, besides the sample temperature and the gas flow field around the sample as concerns the oxygen removal [37]. The second step of the experimental procedure was the lower temperature oxidation/hydrolysis, where the solar-reduced oxide, in the form  $\text{CeO}_{2-\delta}$ , as said very close to the  $\text{Ce}_2\text{O}_3$  one, is oxidized to deliver  $\text{H}_2$  in a fixed bed reactor, this latter shown in Figure 4.2b. As mentioned, the temperature here was around  $400\text{-}600^\circ\text{C}$ . The heat was provided using an electrical resistance. First, an inert gas flow of argon (Ar) was sent in the reactor, in order to remove the air and to reach the desired reaction temperature. Then, nebulized water was also

injected together with the Ar in the reaction site, where it evaporated. After the hydrogen was produced, the output gas was cooled down, and the excess steam was removed. The concentration of  $H_2$  at the outlet was thus measured through a gas analysis unit. For temperatures higher than  $200^\circ\text{C}$ , the reduced cerium oxide is very unstable if exposed to an oxidizing atmosphere, indeed even from TGA the oxidation resulted to be complete at  $200$  to  $300^\circ\text{C}$ . The oxidation kinetics increases rapidly with temperature, and this is the reason why it is necessary to remove the air in the reactor before reaching the reaction temperature (i.e., otherwise the reduced phase would be oxidized by air rather than by water). The aim was to study how the temperature of the fixed bed influenced the reduced cerium oxide reactivity. Results from Abanades and Flamant [37] are summarized in Figure 4.3 [37], that shows the hydrogen production in terms of molar fraction and the gas temperature against time, in different conditions reported in the captions. Water is injected at  $t = 0$  s. What is noticed is that the temperature has a weak rise when water is injected, because of the exothermicity of the hydrolysis reaction, and then fluctuates and decreases according to the fact that latent heat is being absorbed by nebulized water in order to vaporize. In Figure 4.3a, referred to the highest temperature tested,  $600^\circ\text{C}$ , the reduced solid phase completely reacts during the first water injection (dotted vertical line). In the other two cases (Figures 4.3b and 4.3c, referred respectively to gas temperatures of  $515^\circ\text{C}$  and  $440^\circ\text{C}$ ) the  $H_2$  molar fraction increases again after the water injection is stopped (second dotted vertical line), because of the again increasing gas temperature. The kinetics of the water splitting reaction results thus to be fast at all the temperatures studied [37]. After the oxidation runs, it was experimentally assessed that the cerium oxide was completely converted into  $CeO_2$ .

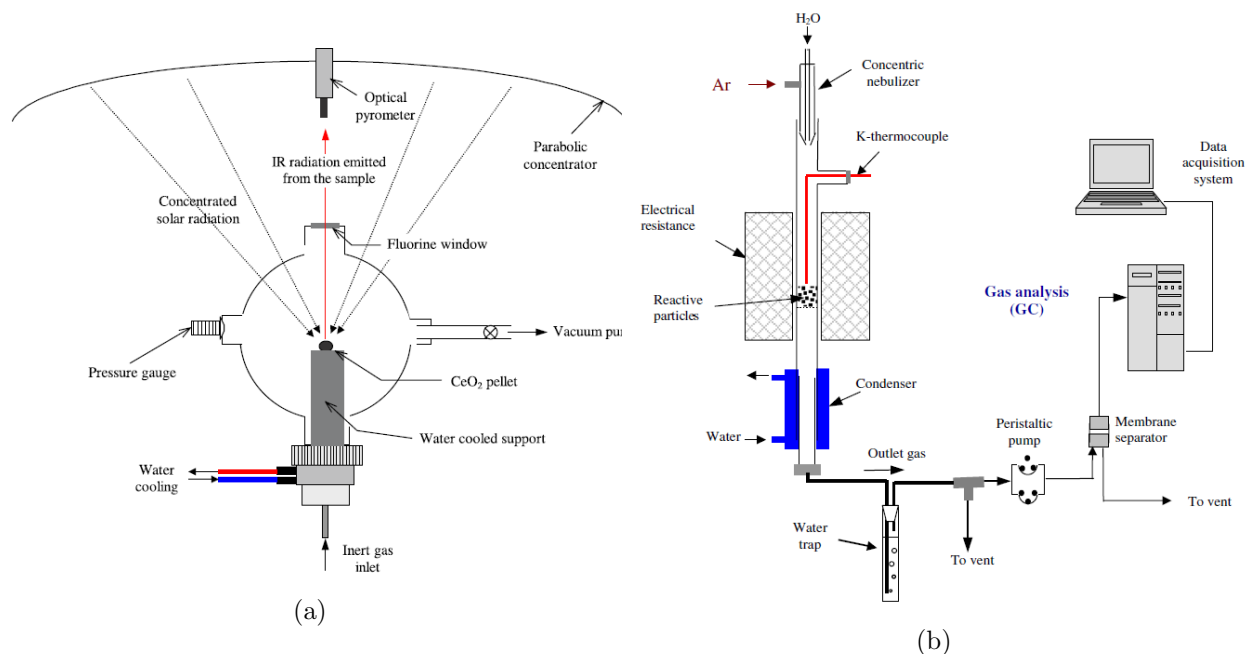


Figure 4.2: Experimental reactors used in the work by Abanades and Flamant [37] for (a) reduction and (b) oxidation steps.

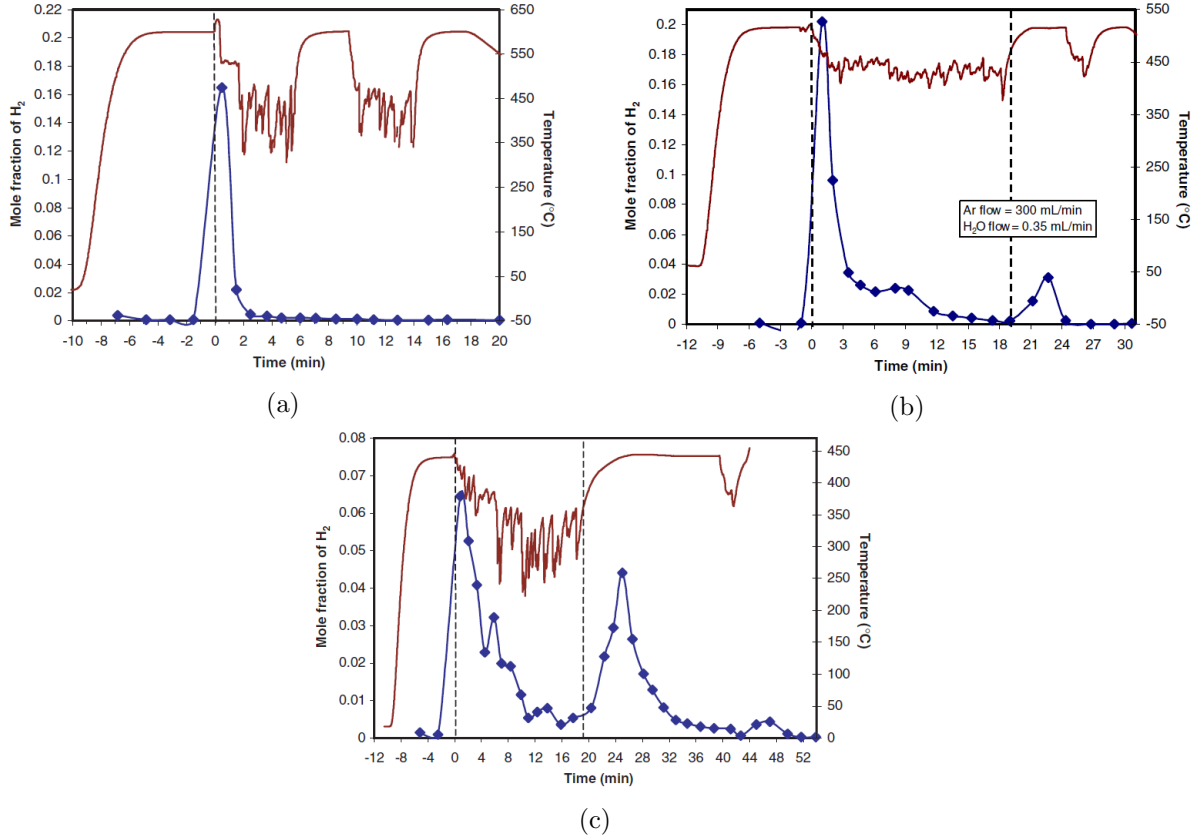
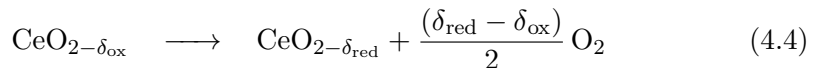


Figure 4.3: Kinetics of hydrogen production for different temperatures vs. time [37]. (a)  $T_{\text{gas}} = 600^\circ\text{C}$ , 1.123 g of  $\text{CeO}_{1.64}$ ; (b)  $T_{\text{gas}} = 515^\circ\text{C}$ , 1.585 g of  $\text{CeO}_{1.59}$ ; (c)  $T_{\text{gas}} = 440^\circ\text{C}$ , 1.954 g of  $\text{CeO}_{1.715}$ .

As mentioned, due to the really high temperatures needed to achieve a complete reduction of ceria, a path that has been extensively studied is its nonstoichiometric reduction, involving a deviation from stoichiometry  $\delta$  well lower than the threshold value of 0.5 pointed out above, as consequence of the much lower temperatures reached in this case. Actually, although the lower yields in terms of oxygen removal and thus of fuel production, the nonstoichiometric ceria (or  $\text{Ce}_{nst}$  in the following) is considered at present the reference MORP cycle because of several appreciable thermodynamic and physico-chemical properties. As already said, the nature of  $\text{Ce}_{nst}$  leads to no changes on the crystal structure even for quite high values of deviation from stoichiometry,  $\delta$  [33], and this allows to avoid possible structural damages. Furthermore, it seems to be fairly attractive for thermochemical fuel production because of the extremely high melting temperature, over 2200 K, whence it remains in the solid phase while cycling, and because of the high catalytic activity in dealing with carbon-containing gases [33]. Moreover,  $\text{Ce}_{nst}$  is characterized by extremely high rates of oxygen chemical diffusivity, whence the advantage of a faster redox kinetics [30]. Let's precise that the *nonstoichiometry* lies in the fact that just a portion of the oxygen atoms are torn out from the original oxide, leading from a structure of the form  $\text{CeO}_2$  to a structure of the form  $\text{CeO}_{2-\delta}$ . The deviation  $\delta$  represents the concentration of oxygen vacancies in the solid phase. The high temperature reduction, the WS and the CDS, written specifically for this redox pair, are shown in

the order here below [32]:



Equations 4.4, 4.5 and 4.6 contain the parameters  $\delta_{\text{red}}$  and  $\delta_{\text{ox}}$ , representing respectively the nonstoichiometry just after reduction and oxidation steps. Their difference ( $\delta_{\text{red}} - \delta_{\text{ox}}$ ) is a generalization of the abovementioned oxygen exchange capacity,  $\delta$ , to the case in which some stoichiometric defect survives after the lower temperature oxidation step. In case the oxidation can be considered as complete,  $\delta_{\text{ox}}$  is zero and  $\delta_{\text{red}}$  reduces to  $\delta$ . It is noteworthy to briefly report the experimental results obtained by Chueh and Haile [33] for the  $\text{Ce}_{\text{nst}}$  cycle implementation, according to which the  $\text{Ce}_{\text{nst}}$  seems to be a good candidate as thermochemical redox medium. In that work, the sample of redox material, made as a porous monolith, was placed in a horizontal tubular structured reactor of alumina, that on its turn was positioned in an IR furnace [33]. As concerns the cycle implementing just water splitting, results in terms of oxygen release during reduction and hydrogen production during oxidation are shown in Figure 4.4a. Left axes report the production rates per unit mass of oxide ( $\text{ml min}^{-1} \text{g}^{-1}$ ), while the values reported inside the plot are the overall productivities per unit mass of oxide ( $\text{ml g}^{-1}$ ). Moreover, the top figure refers to a reduction temperature of 1773 K, whereas the bottom one to a value of 1873 K. The heating ramp corresponding to the figure is of  $1000 \text{ K min}^{-1}$ , while the oxygen partial pressure during reduction has been maintained at  $10^{-5}$  atm. As concerns the top figure, it can be noticed that oxygen is almost immediately released, and the total amount retrieved is around  $4.3 \text{ ml g}^{-1}$ , that corresponds to a deviation  $\delta$  around 0.066. The subsequent oxidation step has been run at 1073 K. Through introducing steam at a partial pressure around 0.25-0.27 atm, hydrogen is fastly produced, up to a total amount (around  $8.5 \text{ ml g}^{-1}$ ) implying a complete reoxidation of the reduced ceria [33]. The average hydrogen production rate over the time interval corresponding to 90% of the extent of reaction is around  $4.6 \text{ ml min}^{-1} \text{g}^{-1}$ . In addition, as expected from thermodynamics and as it has been said above, increasing the reduction temperature from 1773 K to 1873 K (i.e., bottom figure), the oxygen released increases as well, from the previous value of  $4.3 \text{ ml g}^{-1}$  to a value of  $5.9 \text{ ml g}^{-1}$ , corresponding to a deviation  $\delta$  around 0.091. In this second case, running again the oxidation step at 1073 K, the total amount of hydrogen produced is around  $11.8 \text{ ml g}^{-1}$ , with an average value of  $6.2 \text{ ml min}^{-1} \text{g}^{-1}$ , higher than the previous one, probably due to higher reaction rates induced by an increased surface vacancy concentration with respect to the previous case [33]. Apart from hydrogen production, nonstoichiometric ceria has been proved to be suitable even for CO production starting from  $\text{CO}_2$  [33]. Even in this case, the amount of CO produced corresponds to a complete reoxidation of the lattice [33]. The CO production rate and the total amount of CO produced, this latter being around  $7 \text{ ml g}^{-1}$ , are shown in Figure 4.4b [33], that actually refers to 15%Sm-doped ceria (SDC15). The average reaction rate is around  $1.6 \text{ ml min}^{-1} \text{g}^{-1}$ . It is clear that, in principle, both the fuel productivity ( $\text{ml g}^{-1}$ ) and the fuel production rate ( $\text{ml min}^{-1} \text{g}^{-1}$ ) should be kept high over a relevant number of redox cycles (e.g., thousands). However, Chueh and Haile [33] highlighted that both the productivities and the production rates of  $\text{O}_2$  and  $\text{H}_2$  dropped of about 50% after the first 100 cycles, though reaching anyway the complete reoxidation. The main reason for this behaviour, and in particular for the decreasing in the production rates, lies in the reduced surface area of the material that is available for the reaction to take place (approximately from  $5 \mu\text{m}$  to  $15 \mu\text{m}$  of average size of the grains [33]), as consequence of the high number of thermal cycles performed. Thus, parameters of importance in such type of cycles are for sure the porosity and the average grain size, directly linked to the rate at which the reactions can proceed.

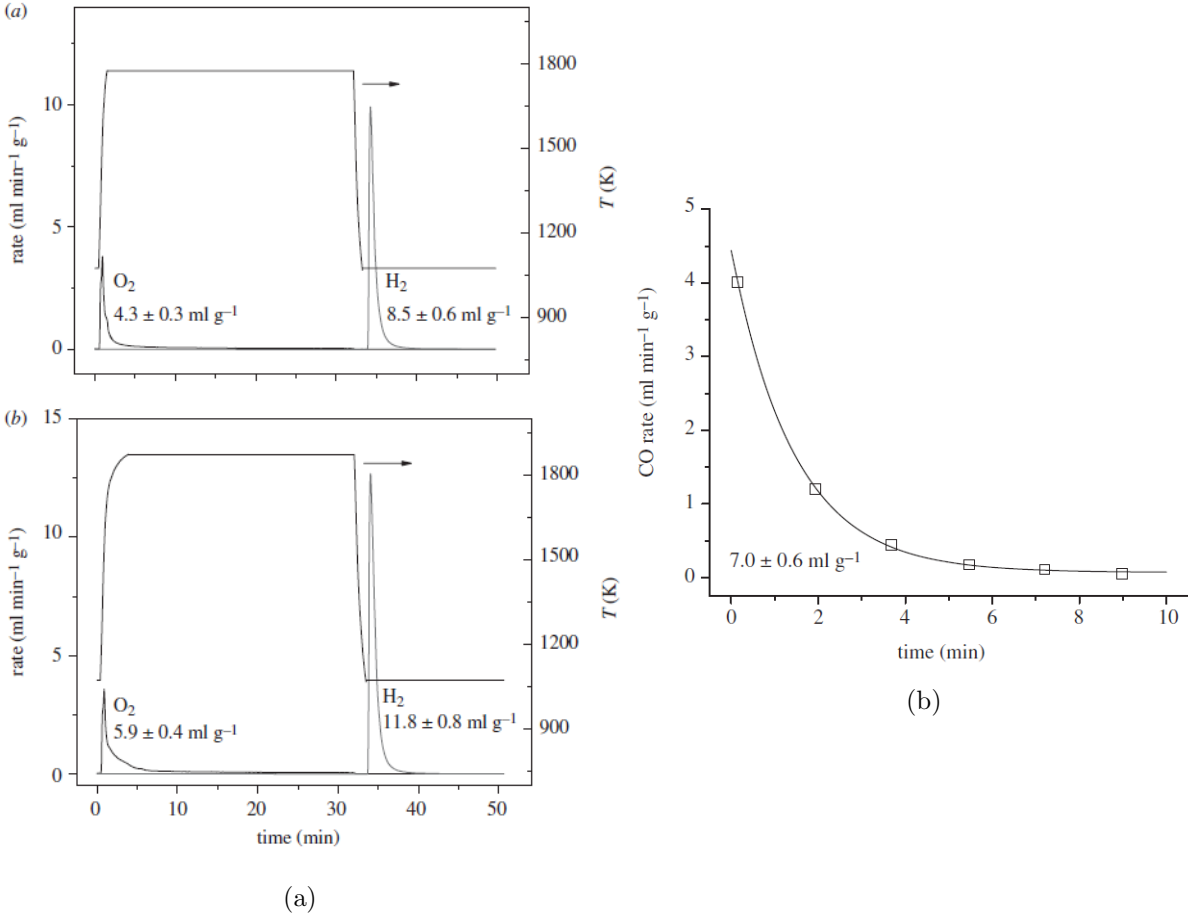


Figure 4.4: (a) O<sub>2</sub> and H<sub>2</sub> production rates and productivities, for T<sub>H</sub> = 1773 K (top) and T<sub>H</sub> = 1873 K (bottom) [33]; (b) CO production rate vs. time using SDC15 at 1073 K,  $\delta_{\text{red}} = 0.05$ ,  $p_{\text{CO}_2} = 0.032$  atm [33].

Several studies implementing such a cycle in nonstructured reactors can be also found in the literature. Possible examples of importance are two research works, conducted partly by the same authors, respectively by J. R. Scheffe, M. Welte and A. Steinfeld [38] for the first one, and by M. Welte, R. Barhoumi, A. Zbinden, J.R. Scheffe and A. Steinfeld [39] for the second one. In these works, an aerosol reactor was tested for the high temperature reduction step of nonstoichiometric ceria cycle, and they allow to point out the most important parameters involved in such a process. For this reason, it is worth mentioning the results there obtained, in order to have a benchmark for assessing the experimental outcomes of the present work.

The aerosol reactor used by Scheffe et al. [38] is shown in Figure 4.5. The ceria particles are supplied at the top through a feeder. The reaction takes place in a vertical alumina tube (Al<sub>2</sub>O<sub>3</sub>,  $D_{\text{out}} = 25.4$  mm,  $D_{\text{in}} = 19.1$  mm,  $L = 1300$  mm), placed within an electrically heated furnace. After have crossed the reaction zone by gravity, the particles are collected at the bottom on a balance, through which both their mass flow rate ( $\dot{m}_{\text{CeO}_{2-\delta}}$ ) and total mass ( $m_{\text{CeO}_{2-\delta}}$ ) are recorded. Argon (Ar), used as a purge gas, is fed both through the bottom balance housing and through the top of the particles feeder. The total gas flow rate exits just below the feeder, above the reaction zone, and its composition is analyzed downstream by mass spectrometry. The reaction zone, due to the system configuration, sees just the bottom Ar flow. An R-type thermocouple measures the

temperature on the external surface ( $T_f$ ) of the alumina tube, in correspondence of the center of the electrically heated region, whereas a B-type thermocouple measures the axial temperature profile along the reaction zone. The furnace was heated up to isothermal outer surface temperatures  $T_f$  in the range 1723-1873 K, with a heating ramp of 20 K min<sup>-1</sup>, while the Ar flow rate ( $\dot{V}_{Ar}$ ) coming from the bottom was varied between 200 and 800 sccm (standard cubic centimeters per minute). Also the residual oxygen mole fraction ( $y_{O_2, \text{baseline}}$ ) in the system was assessed to vary from 50 to 120 ppmv as function of the purge gas flow rate. As concerns the particles size, two typologies were used, namely with median diameters  $D_{v50}$  of 12  $\mu\text{m}$  and 21  $\mu\text{m}$ .

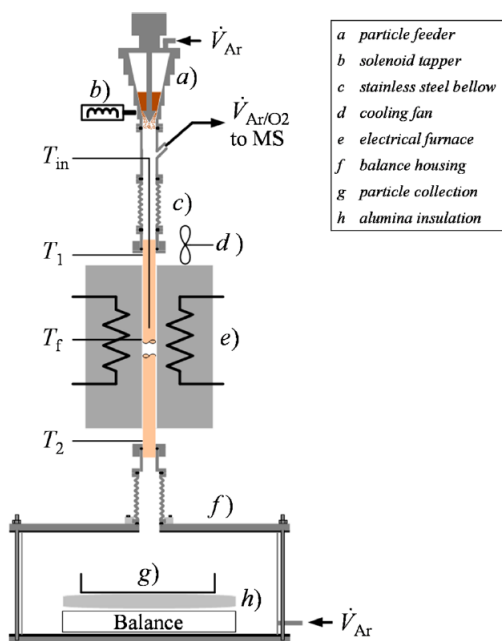


Figure 4.5: Aerosol reactor tested by Scheffe et al. [38].

Two type of experiments were conducted, namely feeding the ceria particles in a pulsed or continuous way. Pulsed case related results will be first briefly reported. In the pulsed experiments, whose short duration was less than 180 s, a ceria mass in the range 15-110 mg was fed in the reactor. Being not time consuming, the aim of these runs was to assess the influence of some leading parameters such as  $T_f$ ,  $\dot{V}_{Ar}$  and  $m_{CeO_{2-\delta}}$ , as well as the particles size distribution,  $D_{v50}$ , on the system behaviour. The results of a representative pulsed run are shown in Figure 4.6, with the experimental conditions reported in the corresponding caption. The mass of ceria used was of roughly 105 mg. As all the ceria mass reaches the balance, a peak in the  $O_2$  release is observed, with some seconds of delay because of the time needed to the oxygen to reach the spectrometer, before returning to the baseline partial pressure value of  $p_{O_2, \text{baseline}} = 6.1 \times 10^{-5}$  atm. The residence time of the particles in the reaction zone was around 1 s. The value of  $\delta_{\text{measured}} = 0.035$  corresponds to the average nonstoichiometry (or reduction extent) of the pulsed experimental run. Starting from the total moles of oxygen delivered, evaluated as in Equation 4.7, the moles of oxidized ceria ( $CeO_2$ ) fed to the reactor can be calculated through Equation 4.8, whence  $\delta_{\text{measured}}$  can be determined as reported in Equation 4.9.  $y_{O_2, \text{total}}$  is the oxygen molar fraction measured by the mass spectrometer downstream the reactor,  $V_{\text{mol}}$  is the gas molar volume equal to 22.4 L mol<sup>-1</sup>, while  $M_i$  stands for

the molar mass of the  $i$  species.

$$n_{O_2} = \int \frac{\dot{V}_{Ar}}{\dot{V}_{mol}} (y_{O_2, total} - y_{O_2, baseline}) dt \quad (4.7)$$

$$n_{CeO_2} = \frac{m_{CeO_{2-\delta}} + M_{O_2} n_{O_2}}{M_{CeO_2}} \quad (4.8)$$

$$\delta_{measured} = \frac{2n_{O_2}}{n_{CeO_2}} \quad (4.9)$$

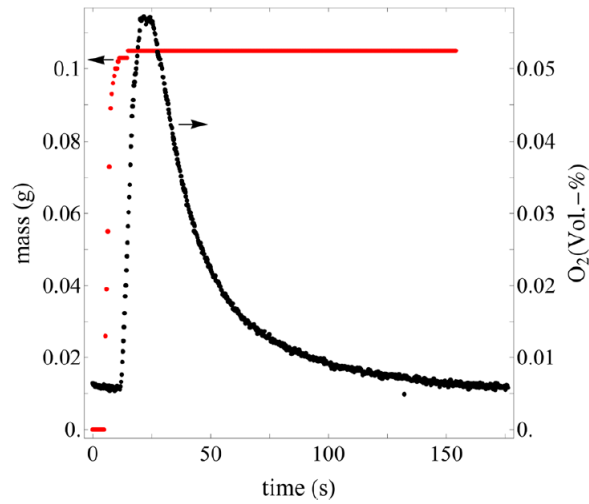


Figure 4.6: Total  $\dot{m}_{CeO_{2-\delta}}$  on the balance and  $O_2$  volume fraction vs. time, with:  $T_f = 1873$  K,  $\dot{V}_{Ar} = 800$  sccm,  $D_{v50} = 21 \mu\text{m}$ ,  $\delta_{measured} = 0.035$ ,  $p_{O_2, baseline} = 6.1 \times 10^{-5}$  atm [38].

To assess how the abovementioned parameters affect the reduction extent,  $T_f$  was varied as said from 1723 to 1873 K,  $\dot{V}_{Ar}$  from 200 to 800 sccm,  $D_{v50}$  from 12 to 21  $\mu\text{m}$  and  $m_{CeO_{2-\delta}}$  from 15 to 110 mg. Each parameter has been varied, of course, keeping constant all the other ones. The results are summarized in the following. As concerns the effect of the reduced ceria mass, the value of  $\delta_{measured}$  decreases as  $m_{CeO_{2-\delta}}$  increases. According to the authors [38], this can be explained at least in three ways: firstly, an increase in the (reduced) ceria mass could correspond to a lower average particle temperature, leading to a lowering of the oxygen release. Secondly, a higher oxygen partial pressure around the particles is expected, thus leading again to a reduced amount of oxygen release. Thirdly, considering to be roughly constant the average residence time of the particles inside the reactor as the ceria mass varies, it can be argued that the time interval during which the particle reaches a given temperature (e.g., the maximum among the particles' one) is shorter for higher ceria masses, and this reflects in a slower kinetics. Furthermore,  $\delta_{measured}$  increases for higher  $T_f$ , as would be expected from thermodynamic considerations, and increases as well for lower particle sizes, due to the higher contact area available. Finally, although an increase in  $\delta_{measured}$  would be expected for higher  $\dot{V}_{Ar}$ , the experimental correlation here appears to be fairly weak. These trends described above are presented in Figure 4.7, with Figure 4.7a showing the effects of  $m_{CeO_{2-\delta}}$  and Figure 4.7b showing the effects of the other three parameters (the three points centered around

a temperature value correspond respectively to 200, 500 and 800 sccm of  $\dot{V}_{\text{Ar}}$ ). In addition, the smaller particles, with median diameter of  $12 \mu\text{m}$  seem to approach the theoretical thermodynamic equilibrium  $\delta_{\text{measured}}$  values, whereas the  $21 \mu\text{m}$  ones roughly half of it.

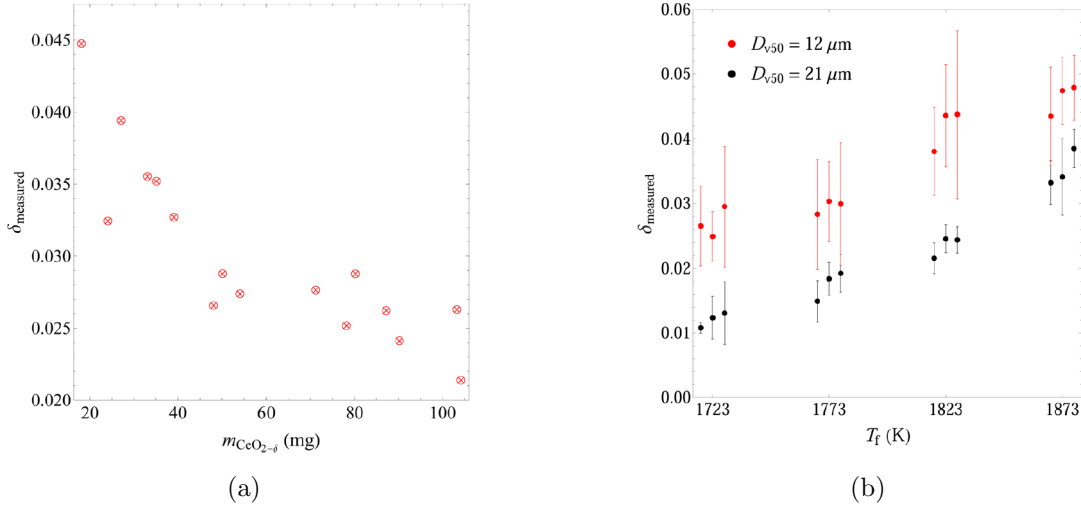
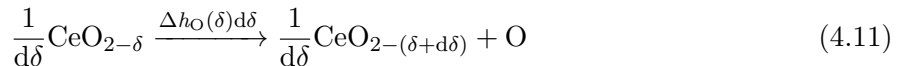


Figure 4.7: (a)  $\delta_{\text{measured}}$  as function of  $m_{\text{CeO}_{2-\delta}}$ , with  $T_f = 1773 \text{ K}$ ,  $\dot{V}_{\text{Ar}} = 500 \text{ sccm}$ ,  $D_{v50} = 12 \mu\text{m}$ ,  $p_{\text{O}_2, \text{baseline}} = (5 \times 10^{-5}) - (1.2 \times 10^{-4}) \text{ atm}$ ; (b)  $\delta_{\text{measured}}$  as function of  $T_f$ ,  $D_{v50}$ ,  $m_{\text{CeO}_{2-\delta}}$  ranging from 15 to 110 mg (as reported by the authors) and  $\dot{V}_{\text{Ar}}$ , with values of 200, 500 and 800 sccm respectively for the three points centered around each temperature value) [38].

Besides the pulsed feeding experiments, even continuous feeding experimental runs were performed. The results of a representative continuous run are shown in Figure 4.8 (in a parallel way with respect to Figure 4.6 referred to the pulsed case), in which three phases in time are highlighted: a first transition regime, in which the oxygen volumetric fraction measured increases with a sort of delay (due to the time needed to reach the spectrometer and to dispersion effects [38]), a steady state regime, in which the oxygen fraction remains fairly constant, and a third purging regime, in which the whole mass has reached the balance, and the oxygen fraction returns to the baseline value. The interesting phase is the steady state one, that would be the desired mode of operation. The authors of the work [38] defined a thermochemical efficiency as reported in Equation 4.10 (slightly rearranged with respect to the reference):

$$\eta_{\text{thermochemical}} = \frac{\overline{\Delta h_{\text{O}}} \dot{n}_{\text{O}}}{\dot{Q}_{\text{furnace}} + \dot{n}_{\text{Ar}} E_{\text{Ar}}} = \frac{\int_{\delta=0}^{\delta_{\text{measured}}} \Delta h_{\text{O}}(\delta) d\delta}{\delta_{\text{measured}}} \frac{\dot{n}_{\text{O}}}{\dot{Q}_{\text{furnace}} + \dot{n}_{\text{Ar}} E_{\text{Ar}}} \quad (4.10)$$

The numerator represents the stored chemical power, expressed as the product between the  $\delta$ -averaged stored energy (i.e., reduction enthalpy) per mole of atomic oxygen,  $\overline{\Delta h_{\text{O}}}$ , and the molar flow rate of atomic oxygen,  $\dot{n}_{\text{O}}$ . Indeed, the reduction enthalpy depends on  $\delta$  [38, 40], and it can be retrieved from literature [40]. The meaning of this can be understood at glance observing the reduction reaction written in a sort of infinitesimal way here below, where the enthalpy needed for a reduction from  $\delta$  to  $\delta + d\delta$  is pointed out on the reaction arrow:



The denominator of Equation 4.10, representing instead the power supplied externally, is the sum of the thermal power provided to the reactor,  $\dot{Q}_{\text{furnace}}$ , and of the power needed for obtaining the given Ar flow rate, on its turn equal to the product between the Ar molar flow rate,  $\dot{n}_{\text{Ar}}$ , and the energy required for separating one mole of Ar,  $E_{\text{Ar}} = 20 \text{ kJ mol}^{-1}$ . This definition assumes inherently the oxidation to be complete before running the reduction step ( $\delta = 0$ ). Furthermore,  $\eta_{\text{thermochemical}}$  increases as the ceria mass flow rate increases, as clearly shown in Figure 4.9a [38]. Then, taking the time-averaged values of  $\eta_{\text{thermochemical}}$  for the three mass flow rates used, both these three values and the  $\delta_{\text{measured}}$  have been plotted versus the ceria mass flow rate, as reported in Figure 4.9b [38]. For increasing  $\dot{m}_{\text{CeO}_{2-\delta}}$ ,  $\eta_{\text{thermochemical}}$  increases, while  $\delta_{\text{measured}}$  decreases, as already pointed out above for the pulsed experimental runs. The  $\eta_{\text{thermochemical}}$  behaviour can be explained considering the following energy balance on the reactor [38]:

$$\dot{Q}_{\text{furnace}} - \dot{E}_{\text{losses}} = \dot{m}_{\text{CeO}_2} \int_{T=298\text{K}}^{T_f} c_{p,\text{CeO}_2} dT + \dot{n}_{\text{Ar}} \int_{T=298\text{K}}^{T_f} c_{p,\text{Ar}} dT + \dot{n}_{\text{O}} \overline{\Delta h_{\text{O}}} \quad (4.12)$$

The furnace power, decreased by the thermal loss items of conductive, convective or radiative nature, must be equal, in the order, to the sum of the heat needed to heat up the ceria mass flow rate, the heat needed to heat up the Ar flow rate and the stored chemical energy.  $c_{p,i}$  is the molar heat capacity of the species  $i$ . Although the reduction extent decreases with increasing ceria mass flow rates, the efficiency increases, due to lower percentage thermal losses with respect to the total supplied power, as discussed in the reference work [38]. Thus, in a solar reactor, it will be important to maximize the ceria mass flow rate, and to assure an as much as possible efficient heat transfer to the redox material.

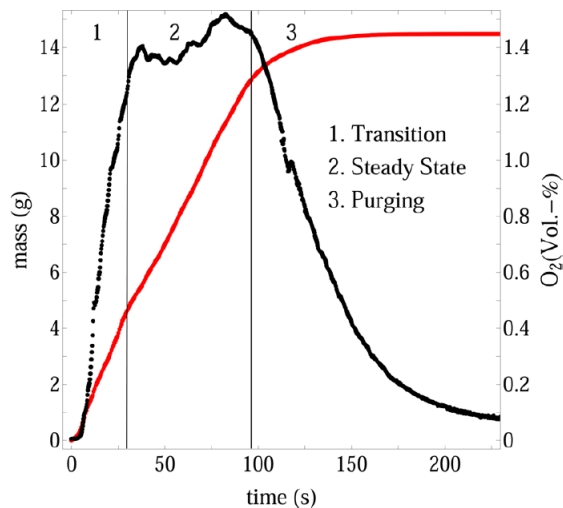


Figure 4.8: Total  $\dot{m}_{\text{CeO}_{2-\delta}}$  on the balance and  $\text{O}_2$  volume fraction vs. time, in case of continuous feeding [38].

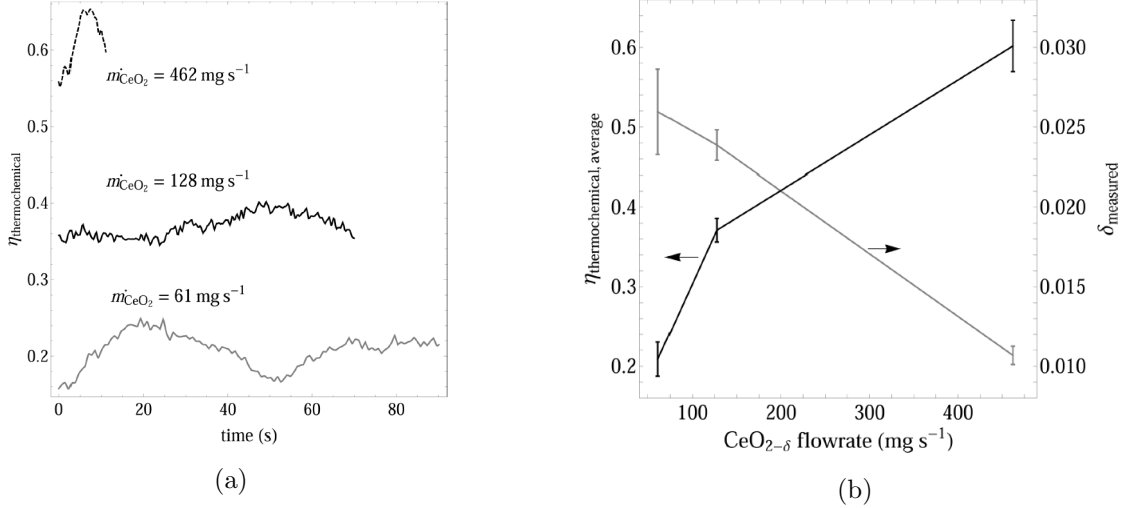


Figure 4.9: (a)  $\eta_{\text{thermochemical}}$  vs. time for  $\dot{m}_{\text{CeO}_2}$  of 61  $\text{mg s}^{-1}$ , 128  $\text{mg s}^{-1}$  and 462  $\text{mg s}^{-1}$ . Top two curves:  $\dot{V}_{\text{Ar}} = 800$  sccm,  $T_f = 1823$  K. Bottom curve:  $\dot{V}_{\text{Ar}} = 500$  sccm,  $T_f = 1818$  K. For all data,  $D_{v50} = 12$   $\mu\text{m}$ ; (b) Average  $\eta_{\text{thermochemical}}$  and  $\delta_{\text{measured}}$  vs.  $\dot{m}_{\text{CeO}_{2-\delta}}$ . Experimental conditions are the same as in Figure 4.9a [38].

Another study that is cited here as concerns nonstoichiometric ceria is the one by Welte et al. [39], consisting again in an experimental demonstration of the reduction phase of a  $\text{Ce}_{\text{nst}}$ -based cycle, this time through a solar aerosol reactor, working in more realistic conditions. The device, shown in Figure 4.10, hosts again an alumina ( $\text{Al}_2\text{O}_3$ ) tube, capable to withstand high temperatures and inert to the air, in which a mass flow rate of oxidized ceria particles ( $D = 70$   $\mu\text{m}$ , purity 99.99%) is fed at the top, and is driven towards the reaction zone by gravity. In counterflow, an argon (Ar) flow rate as purge gas is supplied. The ceria mass flow rate is measured through a balance at the bottom of the tube, while the gases after have exited using a mass spectrometer and an oxygen sensor [39]. Before each experiment, even the residual oxygen partial pressure,  $p_{\text{O}_2, \text{baseline}}$  [39], was measured. The heat is this time provided not through an electrical furnace, but instead by a high flux solar simulator (HFSS, see Subsection 3.2) through a lateral circular aperture of 30 mm diameter, and the temperatures reached are up to 1919 K. Figure 4.10 shows also the nominal cavity temperature ( $T_{\text{cavity}}$ ) in the reaction site and the oxygen partial pressure ( $p_{\text{O}_2}$ ) profile along the tube: going upward, because of the flow arrangement,  $p_{\text{O}_2}$  increases, coherently with the removal of lattice oxygen, whereas the temperature decreases, although significant temperature gradients were not expected due to the multiple internal absorptions, reflections and re-emissions [39].  $T_{\text{cavity}}$  is measured through a type-B thermocouple at the front of the tube, while the particles temperature, that varies from the ambient value to the reaction one, was not measured. The value of  $T_{\text{cavity}}$  thus represents an upper bound for the particles flow temperature. The reduction extent was evaluated through using the measured ceria mass flow rate and oxygen partial pressure. Three reduction runs were performed, whose results are reported in Figure 4.11 and in Table 4.1 [39]. Before each of them, the ceria was completely oxidized ( $\delta_{\text{ox}} = 0$ ) through being exposed to air at 573 K for 8 h [39]. Table 4.1 reports, in the order, the ceria mass flow rate ( $\dot{m}_{\text{CeO}_2}$ ), the argon volume flow rate ( $\dot{V}_{\text{Ar}}$ ),  $T_{\text{cavity}}$ , the solar power ( $P_{\text{solar}}$ ) delivered by the HFSS through the aperture, the nonstoichiometry

$\delta$  achieved and the solar-to-fuel efficiency ( $\eta_{\text{solar-to-fuel}}$ ), this latter being defined as follows:

$$\eta_{\text{solar-to-fuel}} = \frac{2\text{HHV}_{\text{H}_2} \int \delta \dot{n}_{\text{CeO}_2} dt}{\int P_{\text{solar}} dt + E_{\text{inert}} \int \dot{n}_{\text{inert}} dt} \quad (4.13)$$

In Equation 4.13 above, the numerator corresponds again to the stored chemical energy in the hypothesis to produce hydrogen in the oxidation step, with  $\text{HHV}_{\text{H}_2}$  being the higher heating value of hydrogen, while the denominator has the same meaning of Equation 4.10, with the differences that the thermal power supplied is here a radiative power from the HFSS, and that the expression is written in integral form instead of instantaneous one. The deviation  $\delta$ , calculated as said from the ceria mass flow rate and oxygen partial pressure, corresponds, in the three cases, respectively to 20%, 53% and 6% of the theoretical thermodynamic equilibrium. Being this latter assessed at  $T_{\text{cavity}} = 1886 \text{ K}$  (always higher than the ceria particles temperature) and  $p_{\text{O}_2, \text{baseline}} = 2 \times 10^{-4} \text{ atm}$  (always lower than the oxygen partial pressure inside the reactor), then the percentage deviation evaluated in this way represents a conservative estimation of the real reduction extent. The first run (Case 1, in blue) is the reference base case. In the second run, in which the ceria mass flow rate was kept constant, as well as the radiative power, and the argon volume flow rate was doubled, a triplication in  $\delta$  was observed, as well as an increase in the efficiency. Finally, in the third and last run, in which the ceria mass flow rate was decuplicated, the argon volume flow rate was kept constant as in Case 1, and the radiative power was increased to maintain the cavity temperature above 1873 K, the deviation  $\delta$  dropped down, but the efficiency increased. Thus, as a recapping comment, a relative increase in the purge gas flowrate with respect to the ceria one leads to a higher capability to torn out the lattice oxygen from the ceria particles, as intuitively expected, because of a lower local  $p_{\text{O}_2}$  that shifts the equilibrium towards higher  $\delta$  at a given temperature.

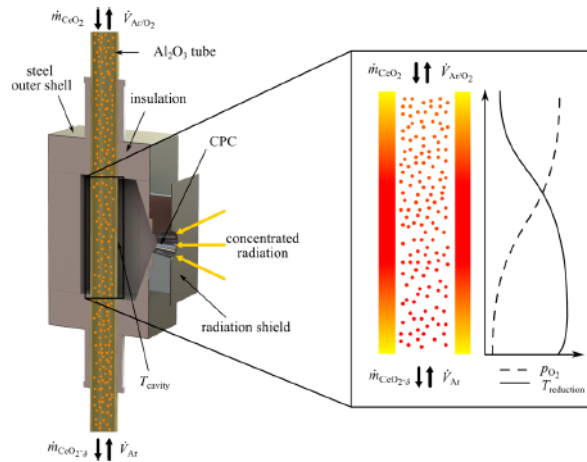


Figure 4.10: Solar reactor tested in the experimental demonstration by Welte et al. (readapted from [39]).

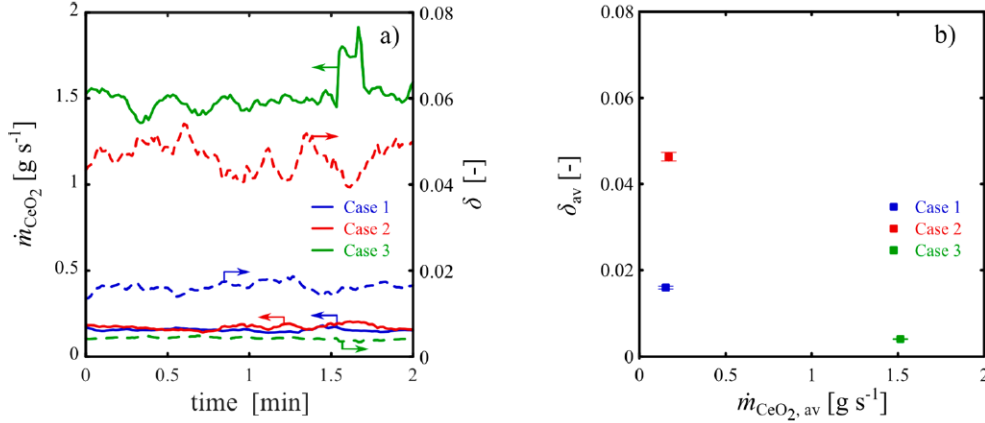


Figure 4.11: Experimental results from Welte et al. [39].

case	$\dot{m}_{\text{CeO}_2}$ [g s <sup>-1</sup> ]	$\dot{V}_{\text{Ar}}$ [L min <sup>-1</sup> ]	$T_{\text{cavity}}$ [K]	$P_{\text{solar}}$ [kW]	$\delta$ [-]	$\eta_{\text{solar-to-fuel}}$ [%]
1	$0.15 \pm 0.0015^b$	2	$1902 \pm 8^a$	2.28	$0.0162 \pm 0.0004^b$	0.18
2	$0.17 \pm 0.0026$	4	$1919 \pm 8$	2.28	$0.0463 \pm 0.0012$	0.56
3	$1.50 \pm 0.0167$	2	$1886 \pm 8$	2.80	$0.0042 \pm 0.0001$	0.37

<sup>a</sup>Given by manufacturer. <sup>b</sup>95% confidence interval.

Table 4.1: Experimental results from Welte et al. [39].

One more research work will be briefly cited here, this time regarding the entire redox cycle. In particular, the thermogravimetric analysis (TGA) results from Furler et al. [48] will be reported. In that work, a ceria reticulated porous ceramic (RPC) structure with dual-scale porosities was used for splitting CO<sub>2</sub> in the oxidation step. Results from TGA using RPC-0 (0%<sub>vol</sub> pore-forming agents) and RPC-50 (50%<sub>vol</sub> pore-forming agents) are shown in Figure 4.12 [48]. The reduction was run at 1773 K in an argon (Ar) inert atmosphere, with oxygen partial pressures ( $p_{\text{O}_2}$ ) lower than  $1.8 \times 10^{-4}$  atm, while the oxidation was performed at 1273 K and a carbon dioxide partial pressure ( $p_{\text{CO}_2}$ ) of 0.385 atm. The nonstoichiometry  $\delta$  was 0.037 and 0.038 respectively for RPC-50 and RPC-0 [48]. Just after the reduction phase, an increase in the mass is observed (see Figure 4.12), before the injection of the CO<sub>2</sub> stream: this is due to the presence of residual oxygen in the system, that led to a partial reoxidation of the sample. A steep increase in the mass is then observed as the CO<sub>2</sub> is delivered, much more rapid in the RPC-50 case. The average CO production rates (up to reaching 90% of the initial oxidation state) was around 2.22 mL min<sup>-1</sup> g<sup>-1</sup> (grams of CeO<sub>2</sub>) and around 0.22 mL min<sup>-1</sup> g<sup>-1</sup> for RPC-50 and RPC-0, respectively [48]. The relevant difference comes from the different specific surface area available for the reaction to take place, due to the presence of the additional  $\mu\text{m}$ -range porosity of the RPC-50 ceria.

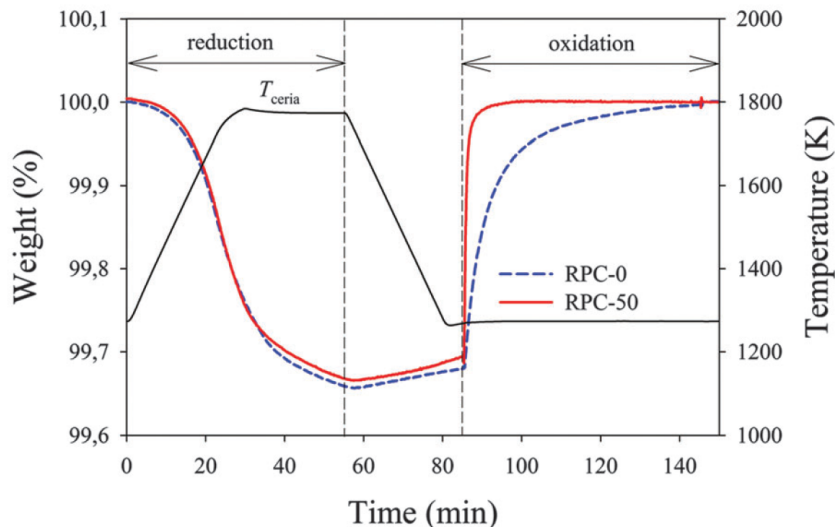


Figure 4.12: TGA results from Furler et al. [48]. RPC-0 and RPC-50 samples were compared. Reduction was conducted at  $T = 1773$  K and  $p_{\text{O}_2} < 1.8 \times 10^{-4}$  atm. Oxidation was conducted at  $T = 1273$  K and  $p_{\text{CO}_2} = 0.385$  atm.

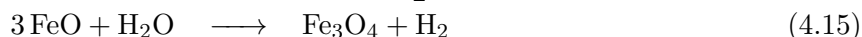
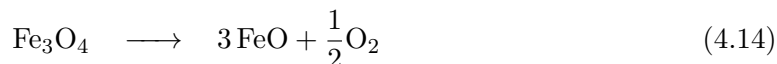
Going forward, in the perspective in which the stoichiometric cycle requires too high temperatures, and the nonstoichiometric cycle assures just relatively low yields, the alternative of doped ceria loops can be a solution to improve the reactivity of the redox material at lower temperatures. As concerns the technical solutions implementing doped ceria, several possibilities have been explored. The doping, performed using transition metals or rare earth elements, has the aim to tune the thermodynamic properties of the redox material and to possibly improve the redox performances [32]. Doping with  $\text{Zr}^{4+}$ , and thus considering the structure  $\text{Zr}_{0.25}\text{Ce}_{0.75}\text{O}_2$ , led to an improvement of the reduction extent, but to a decrease of the oxidation kinetics, according to Le Gal, Abanades and Flamant [41]. Le Gal and Abanades [42] studied also the doping of ceria with Ta, La, Sm and Gd, thus obtaining binary oxides, and the doping of ceria-zirconia solutions, thus obtaining ternary oxides. Ta-doped ceria resulted in a higher reduction extent, but the water dissociation reaction is hindered by the formation of a secondary phase. La-, Sm- and Gd-doped ceria led to a better thermal stability after have performed consecutive cycles, with the same hydrogen production compared to undoped ceria. Gd-Zr-doped ceria showed a higher hydrogen production with respect to Zr-doped ceria. Finally, La-Zr-doped ceria resulted in an improved thermal stability too. Besides these examples reported here, several other studies about doped ceria are widely available in the literature [32].

## 4.2 Iron oxides based thermochemical cycles

The iron oxides based cycles foresee the redox cycling among the reduced wüstite phase,  $\text{FeO}$ , in which the Fe atom is in the  $2^+$  oxidation state, the partially oxidized magnetite phase,  $\text{Fe}_3\text{O}_4$ , in which the Fe atoms are arranged in a form of the type  $\text{Fe}^{2+}(\text{Fe}^{3+}\text{O}_2)_2$ , and the fully oxidized hematite phase, with general formula  $\text{Fe}_2\text{O}_3$ , where both the Fe atoms are in the  $3^+$  oxidation state. For the reduction reaction from the magnetite phase to the wüstite one,  $\Delta G$  equals zero at  $T = 2500$  K, thereby requiring high temperatures for the process, and this leads to complications in the cycle, being the melting temperatures of the two phases respectively around 2000 K and 1643 K [34]. In the practice, however, this issue can be overcome performing the cycle at low

oxygen partial pressure conditions [34], and the experimental feasibility of such a solution has been proved by Charvin et al. [49] for hydrogen production. In that work, both thermodynamic and experimental studies were performed. As reference value, considering the energy needed to heat up 1 mole of magnetite from 600°C to 2100°C (446.51 kJ), the enthalpy of endothermic reduction (242.84 kJ) and the energy required to heat up 1 mole of water from 25°C to 600°C (64.9 kJ), and being the higher heating value of hydrogen equal to 286 kJ/mol, a theoretical efficiency around 37.1% has been estimated for this redox pair [49].

If magnetite and wüstite phases are considered for cycling, then the reduction and oxidation - both with H<sub>2</sub>O and CO<sub>2</sub> - reference reactions are the ones reported in the order below:



As already done for cerium oxides, some experimental results previously achieved using the iron based pair will be now mentioned. Charvin et al. [49] studied this cycle making use of the experimental set-up shown in Figure 4.13a for performing the high temperature reduction step. A solar furnace was used to heat up the sample, composed of about 1 g of Fe<sub>2</sub>O<sub>3</sub> commercial powder (99.9% purity, 100 μm), processed both directly or in form of compact pellets. The sample behaviour was studied both in air and in an inert (nitrogen, N<sub>2</sub>) atmosphere. In this latter case, the controlled atmosphere was maintained through a glass vessel around the reaction zone and a vacuum pump assuring the removal of the released oxygen for avoiding its recombination with the reduced phase. The sample was positioned on a water-cooled support, and its temperature was measured through an infrared pyrometer placed in the centre of the mirror. The sample heating was controlled through adjusting its position with respect to the parabolic mirror focal plane.

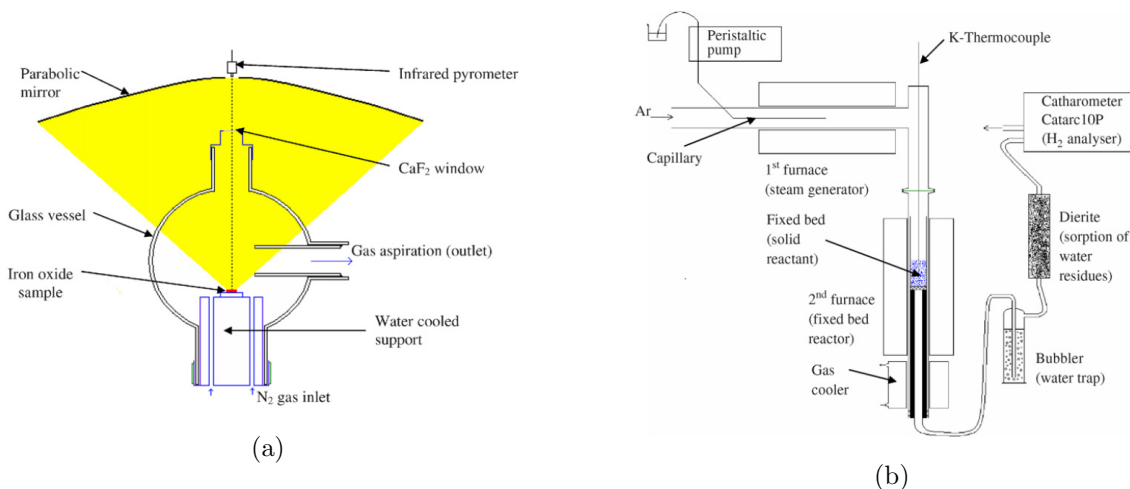


Figure 4.13: (a) Experimental set-up used by Charvin et al. [49] for performing (a) the reduction and (b) the oxidation steps.

It is worth mentioning that this redox cycle does not encompass the fully reoxidation towards the hematite (Fe<sub>2</sub>O<sub>3</sub>) phase, because of thermodynamic limitations. Thus, starting from (Fe<sub>2</sub>O<sub>3</sub>) as raw material, after a first reduction phase in the first cycle hopefully complete towards FeO, then the following redox cycles will deal just with the pair Fe<sub>3</sub>O<sub>4</sub>/FeO. A complete reduction towards

FeO would be desired in general. What has been just mentioned can be understood at glance looking at Figure 4.14, showing the equilibrium compositions respectively for the system (3FeO + H<sub>2</sub>O) moles (Figure 4.14a [49]) and for the system (3FeO + CO<sub>2</sub>) moles (Figure 4.14b [50]), both in a N<sub>2</sub> atmosphere at 1 bar. These compositions are the ones of interest for the oxidation phase, as clearly reported in Reactions 4.15 and 4.16 above. Let's notice that the Fe<sub>2</sub>O<sub>3</sub> phase is practically never observed in the equilibrium with H<sub>2</sub>O, whereas its molar fraction goes to zero as well in the equilibrium with CO<sub>2</sub> for temperatures higher than 500°C.

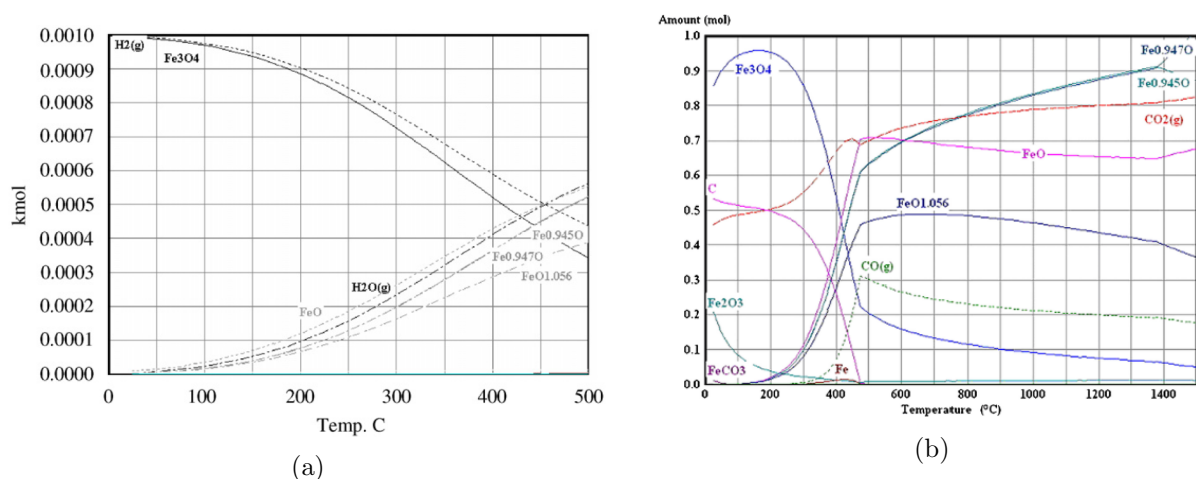
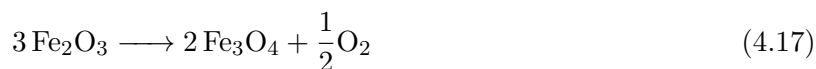


Figure 4.14: Equilibrium compositions involving iron oxides. (a) Equilibrium composition for the Fe/O/H system, starting from 3 mol of FeO and 1 mol of H<sub>2</sub>O, at 1 bar in N<sub>2</sub> atmosphere [49]; (b) Equilibrium composition for the Fe/O/C system, starting from 3 mol of FeO and 1 mol of CO<sub>2</sub>, at 1 bar in N<sub>2</sub> atmosphere [50].

Returning to the experimental work from Charvin et al. [49], that deals with only water oxidation, the final products obtained depend also on the atmosphere composition, that is, on if N<sub>2</sub> or air are used. Results referring to Fe<sub>2</sub>O<sub>3</sub> pellets heated up to 1700°C, obtained through X-ray diffraction, are summarized in Table 4.2 [49]. This temperature is above the melting point of all the three phases, thus the sample melting was observed [49]. The reduction led to a mixture Fe<sub>3</sub>O<sub>4</sub> + FeO through using air, whereas just FeO, as desired, was obtained using N<sub>2</sub>. The two reduction reactions involved are the one from hematite towards magnetite, as said of interest just in the first cycle, and the one from magnetite towards wüstite, as reported respectively in Reaction 4.17 below and in Reaction 4.14 above (and reported again here below as well):



As reported by the authors, in all the tested conditions reported in Table 4.2 hematite was not observed. Reduction reaction 4.17 resulted to be complete heating up the hematite over 1500°C, while the reduction reaction 4.14 led to several nonstoichiometric wüstite phases of the type Fe<sub>0.909</sub>O, Fe<sub>0.945</sub>O and Fe<sub>0.947</sub>O, according to what it is expected from thermodynamics [49]. Reduction in air never reached the completion towards FeO, whereas the reduction in N<sub>2</sub> atmosphere at 0.1 bar needed just 2 min to obtain a chemical conversion of 100% towards wüstite, according with the lower oxygen partial pressure maintained in the reaction site.

Reactant	Atmosphere	Pressure (bar)	Heating time	Product	Mass fraction of wustite (%)	Chemical conversion (%)
Fe <sub>2</sub> O <sub>3</sub>	N <sub>2</sub>	0.1	30 s	Fe <sub>3</sub> O <sub>4</sub> + FeO	85	95
Fe <sub>2</sub> O <sub>3</sub>	N <sub>2</sub>	0.1	1 min	Fe <sub>3</sub> O <sub>4</sub> + FeO	93	98
Fe <sub>2</sub> O <sub>3</sub>	N <sub>2</sub>	0.1	2 min	FeO	100	100
Fe <sub>2</sub> O <sub>3</sub>	N <sub>2</sub>	0.8	2 min	Fe <sub>3</sub> O <sub>4</sub> + FeO	91	97
Fe <sub>2</sub> O <sub>3</sub>	N <sub>2</sub>	0.8	5 min	Fe <sub>3</sub> O <sub>4</sub> + FeO	95	98.5
Fe <sub>2</sub> O <sub>3</sub>	Air	0.8	15 min	Fe <sub>3</sub> O <sub>4</sub> + FeO	82	93.5

Table 4.2: Experimental results from Charvin et al. [49] for the high temperature reduction step at 1700°C.

As concerns the low temperature water splitting step, thermodynamics suggests to perform the water-fed oxidation reaction at temperatures below 800°C [49]. For this reason, an electrical furnace was instead used. The equipment is shown in Figure 4.13b. The reduced sample was placed in a fixed-bed reactor inside the vertical furnace. Before the reaction, the sample was milled to enhance the contact area with steam, and also sieved in order to conduct experiments with different particle sizes. The bed temperature was measured through a K-thermocouple. The input flow rates into the reaction site were 0.225 ml/min of water, then evaporated in another furnace to produce steam, and 220 Nml/min of argon (Ar). Downstream, the steam was removed, and the H<sub>2</sub> molar fraction was measured online through a catharometer. Starting from the imposed Ar molar flow rate ( $\dot{n}_{\text{Ar}}$ ) and the measured H<sub>2</sub> molar fraction ( $y_{\text{H}_2}$ ), the H<sub>2</sub> molar flowrate ( $\dot{n}_{\text{H}_2}$ ) was evaluated through Equation 4.18, whereas the total normal volume of H<sub>2</sub> produced ( $V_{\text{H}_2}$ ) was calculated through Equation 4.19, where the integration is extended from the starting time  $t_0$  to the time instant  $t_{0.5}$  in which the hydrogen molar fraction was as low as 0.5%.

$$\dot{n}_{\text{H}_2} = \frac{y_{\text{H}_2}}{1 - y_{\text{H}_2}} \dot{n}_{\text{Ar}} \quad (4.18)$$

$$V_{\text{H}_2} = \frac{RT}{p} \times \int_{t_0}^{t_{0.5}} \dot{n}_{\text{H}_2} dt \quad (4.19)$$

The H<sub>2</sub> molar fraction detected downstream the reactor is shown in Figure 4.15 [49]. Before the experiment, the reactor was purged with Ar in order to eliminate the residual air (i.e., oxygen) inside the system. Then, the fixed bed was heated up to the target temperature (around 520°C) at the fixed Ar flow rate, and then fed through the Ar-steam stream. From the figure, a weak H<sub>2</sub> production is observed before the steam injection, probably because of some moisture inside the system. Moreover, an increase in temperature is observed when steam is injected, as consequence of the exothermicity of the oxidation reaction. A steep increase in the H<sub>2</sub> is observed, and then a gradual decrease to negligible values, confirming the occurrence of the oxidation and the oxygen filling of the iron oxide lattice.

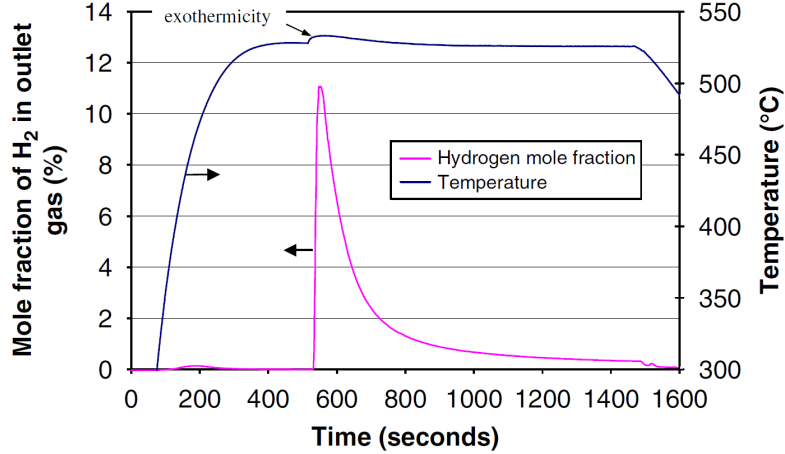


Figure 4.15:  $H_2$  molar fraction and temperature in time, measured by Charvin et al. [49] (sample mass: 2 g of  $FeO$ ; particles size:  $30 < d_p < 50 \mu m$ ; argon volume flow rate: 220 Nml/min).

Several kinetic considerations concerning the reactivity of the reduced material towards the water splitting step can be also found in literature [49]. The piece of information that is important to mention here is that the reactivity of the reduced sample is strongly influenced by the material processing before the oxidation reaction, that affects its properties. Indeed, the material processing influences the nonstoichiometry achieved before starting the oxidation, and thus also the amount of oxygen absorbable. Charvin et al. [49] compared the solar-reduced wüstite and a commercial one, and the results obtained are summarized in Table 4.3, where the two typologies of samples are referred to respectively using  $s$  and  $c$  subscripts.

Exp. no	Reactant	Mass (g)	Particles size ( $\mu m$ )	$T$ ( $^{\circ}C$ )	Reaction time (min)	Volume $H_2$ (ml)	Chemical conversion <sup>a</sup> (%)	mmol $H_2$ /g of $FeO$
1	$FeO_s$	2.35	$100 < d_p < 125$	675	32	17.3	7	0.33
2	$FeO_s$	2.35	$80 < d_p < 100$	675	40	72	29.5	1.37
3	$FeO_c$	2	$125 < d_p < 200$	575	28	71	34.1	1.58
4	$FeO_c$	2	$30 < d_p < 50$	480	29	70	33.6	1.56
5	$FeO_c$	2	$30 < d_p < 50$	525	50	138	66.4	3.08
6	$FeO_c$	2	$30 < d_p < 50$	575	44	191.2	92	4.27
7	$FeO_s$	2	$30 < d_p < 50$	575	28	112	53.9	2.5
8	$FeO_s$	2	$30 < d_p < 50$	525	18	60.9	29.3	1.36

Table 4.3: Experimental results from Charvin et al. [49] for the low temperature oxidation step: the solar-reduced wüstite (subscript  $s$ ) and a commercial one (subscript  $c$ ) are compared in terms of volume of hydrogen produced, chemical conversion (based on stoichiometric  $FeO$ ) of the initial sample and mole of hydrogen produced per gram of  $FeO$ .

Besides the material processing, also the bed temperature intensely affects the oxidation kinetics: the higher the temperature, the higher both the maximum value of the hydrogen mole fraction in time and the final conversion reached [49]. Finally, a third factor of influence is the particle size, as expected: the lower the particles diameter, the higher both the peak in hydrogen production and the final conversion of the sample [49]. A further, fourth parameter that influences the results (in terms of kinetics and final conversion) is of course the reaction time considered.

After have presented the work by Charvin et al [49] as concerns the hydrogen production, it is worth mentioning now some experimental results regarding the iron oxides based cycle implementing the CDS reaction in place of the WS one. At this aim, the research work by Abanades et al. [50] will

be briefly reported and described.

Under a purely thermodynamic point of view, something about the equilibrium composition starting from  $(3\text{FeO} + \text{CO}_2)$  moles has been already pointed out in Figure 4.14b [50] above. From the same figure, it is also evident that the optimal temperature for  $\text{CO}_2$  conversion towards  $\text{CO}$  for the initial composition considered is around  $500^\circ\text{C}$ , where a value of roughly 30% is observed. Furthermore, keeping constant at 3 moles the initial amount of  $\text{FeO}$ , and increasing the  $\text{CO}_2/\text{FeO}$  ratio, the amount of  $\text{Fe}_3\text{O}_4$  and  $\text{CO}$  increases in a monotonous way as this ratio increases, thereby allowing to conclude that an excess in  $\text{CO}_2$  is desirable to enhance the reaction extent [50]. Besides this, some other interesting considerations are that (i) lower and lower pressures are favourable for the hematite reduction reaction towards  $\text{FeO}$  and nonstoichiometric wüstite phases, and that (ii) thermal reduction of hematite towards wüstite becomes notable independently from pressure if temperature is above  $1500^\circ\text{C}$  [50].

Let's turn now to the experimental procedure and results. As concerns the reduction step, even in this case a solar furnace facility was used to convert a commercial  $\text{Fe}_2\text{O}_3$  powder into  $\text{FeO}$ . The equipment used for the reduction step is shown in Figure 4.16 [50], and it is substantially identical to the one of Figure 4.2a. The sample was placed on a water-cooled holder and heated up by the radiation coming from the solar furnace facility, composed of a heliostat and a parabolic concentrator.

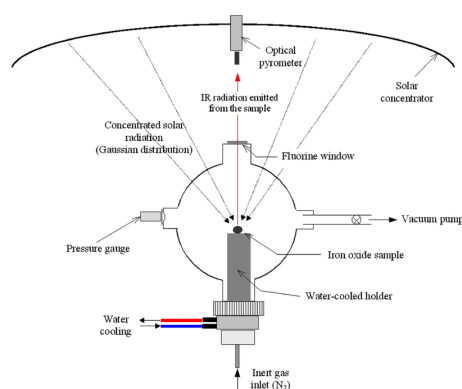


Figure 4.16: Solar reactor used by Abanades et al. [50] for performing the reduction step from hematite towards wüstite under controlled atmosphere.

After a first - complete - reduction of hematite to magnetite in air, the following reduction towards wüstite was performed in an inert nitrogen atmosphere at a pressure of 0.2 bar. The  $\text{N}_2$  flow rate was fixed at 5 NL/min. The nitrogen stream, as usual, is aimed at removing the released oxygen near the sample, thereby avoiding its recombination with the reduced phase. The second reduction reaction occurred above the magnetite melting point (1870 K). The resulting reduced samples, in form of pellets, were grounded and sieved to obtain samples with different particles size. X-ray diffraction revealed that the prevailing phase in the reduced samples was the wüstite one, besides some unconverted  $\text{Fe}_3\text{O}_4$ . From thermogravimetric analysis (TGA), the  $\text{FeO}$  mass fraction in the solar reduced powder resulted to be around 60% [50].

The oxidation of such  $\text{FeO}$ -rich mixed samples with  $\text{CO}_2$  was then studied through a TGA, both in isothermal and dynamic conditions. Isothermal runs were performed in the range  $600\text{--}800^\circ\text{C}$ , whereas dynamic runs were performed up to  $1100^\circ\text{C}$ . Both the experimental procedures were used to assess the influence of temperature,  $\text{CO}_2$  concentration and particles size on the CDS rate. The reaction site was properly purged and filled with argon before running the experiments, in order to

remove the residual air. Together with the solar-reduced samples, containing as said around 60% in mass of FeO, even a commercial FeO powder (purity 99.9%) was tested for sake of comparison. The authors report the following expressions for evaluating respectively the conversion extent in the commercial powder case, and the moles of CO produced per gram of FeO in the solar-reduced sample case:

$$X_{\text{FeO}} = 3 \frac{\Delta m}{16} \frac{M_{\text{FeO}}}{m_0} \quad (4.20)$$

$$n_{\text{CO}} = \frac{\Delta m}{16 m_0 x_{\text{FeO}}} \quad (4.21)$$

These expressions appear clear observing the stoichiometry of Reaction 4.16. In the order,  $\Delta m$  is the mass gain in terms of lattice oxygen,  $M_{\text{FeO}}$  is the molar mass of magnetite,  $m_0$  is the initial mass of the sample, and  $x_{\text{FeO}}$  is the mass fraction of wüstite in the solar reduced sample. Figure 4.17 [50] shows the results obtained for both (a) isothermal and (b) dynamic oxidation. As concerns isothermal runs (Figure 4.17a), both the reaction rate (connected with the slope of the curves) and the final conversion increase as the temperature increases, so a strong temperature dependence is pointed out, at a given particles size. By way of example, a final conversion efficiency higher than 90% is observed at 800°C after 90 min, corresponding to a productivity of 4.3 mmol<sub>CO</sub>/g<sub>FeO</sub>, against a maximum theoretical value of 4.6 mmol<sub>CO</sub>/g<sub>FeO</sub> in case of complete FeO conversion [50]. As concerns dynamic runs (Figure 4.17b), in which the heating ramp was fixed at 15°C/min, it is highlighted that the CO<sub>2</sub>-driven oxidation starts at around 400°C, regardless of the CO<sub>2</sub> concentration in the feed gas [50]. The maximum conversion achieved is of roughly 95% at the highest temperature tested (1100°C), corresponding to a CO production of 4.4 mmol<sub>CO</sub>/g<sub>FeO</sub>. Also here, the reaction rate (i.e., slope of the curves) increases with temperature, before reaching a final plateau level.

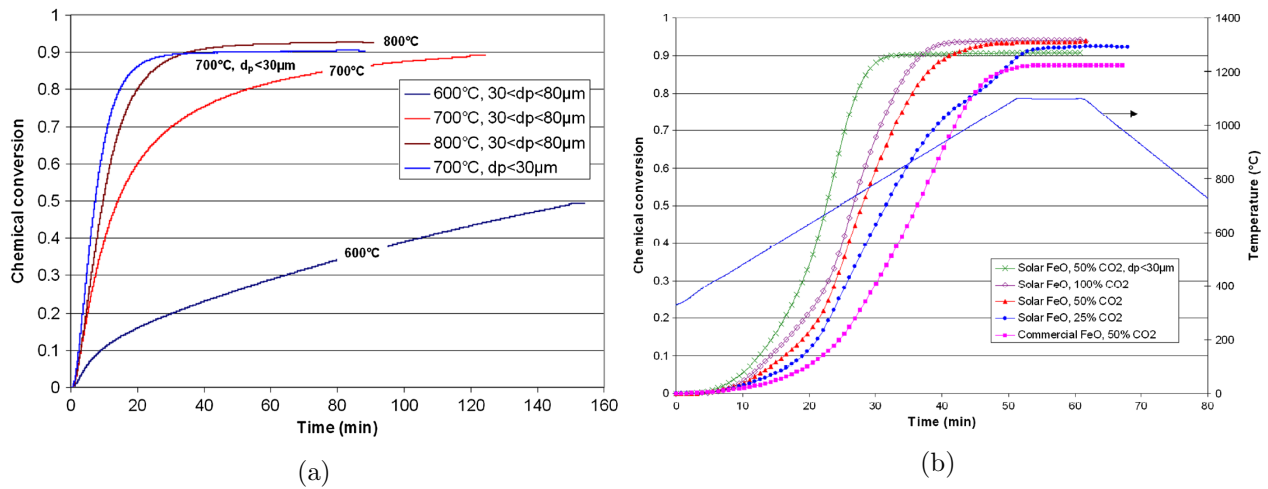


Figure 4.17: Experimental results in terms of chemical conversion vs. time from Abanades et al. [50] concerning the oxidation step. (a) Results in isothermal conditions, for the solar-reduced samples, for temperatures in the range 600-800°C and different particles diameter, and for a CO<sub>2</sub> concentration of 50%; (b) Results in dynamic conditions, for both the samples analysed, and for different CO<sub>2</sub> concentrations and particles diameter (this latter in the range 30-80 μm when not specified).

Besides the temperature dependence, several other factors influencing the outcomes can be men-

tioned. Firstly, the type of FeO material used: commercial FeO, very close to exact stoichiometry, led to lower reaction rates and to lower final conversions, if compared with the solar-produced FeO, that actually contains several nonstoichiometric phases characterized on average by a structure of the type  $\text{Fe}_{1-\delta}\text{O}$ , with  $\delta$  close to 0.05 [50]. The higher reactivity due to nonstoichiometric structures can be explained through the formation of large defect clusters [50]. However, this aspect is not deepened herein, and further details can be found in the references [50]. There are still two factors that affect the results: the particles size and the  $\text{CO}_2$  concentration. In particular, the lower the particles diameter, the higher the reaction rates, because of an increase in the specific surface contact area. This is confirmed even looking at Figure 4.17 above, for both the isothermal and dynamic curves, in which steeper slopes are observed in case of smaller particles. Finally, the higher the  $\text{CO}_2$  concentration around the sample, the higher the oxidation reaction rates. This is again confirmed looking at Figure 4.17b. The final conversion results remain instead roughly the same.

As concluding remark about this literature review reported so far, the main parameters that influence the iron oxides based cycle, implementing both WS and CDS reaction in the oxidation step, are (i) the temperatures involved, (ii) the type of material used and its previous processing or treatment, that determine its structure and its level of eventual nonstoichiometry, (iii) the particles size, (iv) the concentration of the species involved and of course (vi) the reaction times considered.

## 5 Experimental activity

In this section, the whole experimental activity will be presented and described. A TGA has been conducted on cerium oxide samples and on iron oxide samples. The oxidation steps were focused on CO production through implementing a CO<sub>2</sub> feeding. Subsection 5.1 presents the equipment used, whereas Subsection 5.2 deals with the experimental procedures and results obtained.

### 5.1 Test bench description

#### 5.1.1 Thermogravimetric analysis (TGA)

Thermogravimetric analysis (TGA) consists in measuring the mass (or the mass variation) of a given sample during time, either in isothermal conditions or according to predefined heating or cooling temperature ramps. Typically, either an inert, oxidizing or vacuum atmosphere can be implemented in the reaction site, both static or dynamic one. As already mentioned, several physical phenomena can be studied in this way, such as thermal decomposition or solid-gas reactions. The output of the analysis is made up of curves, called thermograms, thermal decomposition curves or simply TGA curves, through which the absolute or relative sample mass is plotted versus time or temperature. The main components of a thermogravimetric analyzer are, in general:

- i. A thermobalance, aimed at monitoring the sample mass variations. The measurement is performed through the two arms of the balance, supporting respectively the crucible with the sample to be analyzed and a reference weight. Photodiodes are used as transducers to convert the optical signal, deriving from the movement of the arms, into an electrical signal, that is then elaborated to obtain eventually the mass variation;
- ii. The furnace, typically made up of refractory materials, such as alumina (Al<sub>2</sub>O<sub>3</sub>), with melting temperature above 2000°C;
- iii. Crucibles, composed of inert material, such as alumina;
- iv. Thermocouples, to measure the temperature in the reaction site, near the sample;
- v. Gas flow managing system, to control the atmosphere and to remove the eventual gas produced;
- vi. A data elaborating system, such as a computer.

The thermogravimetric analyzer used in the present experimental activity is the STA 2500 Regulus by NETZSCH, whose main technical data are summarized in Table 5.1 [47]. As can be observed, the thermogravimetric resolution of 0.03 μg is extremely low, several orders of magnitude lower than the weight of a typical sample (~ mg).

<b>Furnace data</b>	
Temperature range	Up to 1600°C
Heating rate	0.001 to 100 K min <sup>-1</sup>
<b>Balance and sensor data</b>	
Weighing range	± 250 mg, max. sample load 1 g
Thermogravimetric resolution	0.03 μg
<b>Atmosphere</b>	
Gas atmospheres	Inert, oxidizing, vacuum

Table 5.1: Technical data of the thermogravimetric analyzer STA 2500 Regulus [47].

## 5.2 Experimental procedure and results

### 5.2.1 TGA on cerium oxides

The STA 2500 Regulus thermogravimetric analyzer was used, and three redox cycles were performed, with three different cerium oxide samples: an oxidized one, a reduced one and a virgin (i.e., as it is) one. According to the thermal program implemented during the analysis, there is an initial stable phase of 5 minutes at 20°C, then a heating ramp with a slope of 50 K/min brings the system at 1600°C, temperature at which the reduction takes place for a duration of 30 minutes per cycle. Reduction is followed by a cooling ramp with a slope of -50 k/min, until the temperature reaches the value of 800°C. At this thermal level, a first stabilization phase of 5 minutes is maintained, then the oxidation by injecting CO<sub>2</sub> takes place for 15 minutes, and finally a second stabilization phase is performed for 5 minutes again, before starting again with a heating ramp for the following cycle. The temperature plot in time will be shown herein in the following pictures. Table 5.2 summarizes the thermal program just described, composed of 19 total segments.

Segment	T <sub>start</sub> /duration or slope/T <sub>end</sub>
#1	20°C/5 min/20°C
#2	20°C/50 K min <sup>-1</sup> /1600°C
#3	1600°C/30 min/1600°C
#4	1600°C/-50 K min <sup>-1</sup> /800°C
#5	800°C/5 min/800°C
#6	800°C/15 min/800°C
#7	800°C/5 min/800°C
#8	800°C/50 K min <sup>-1</sup> /1600°C
#9	1600°C/30 min/1600°C
#10	1600°C/-50 K min <sup>-1</sup> /800°C
#11	800°C/5 min/800°C
#12	800°C/15 min/800°C
#13	800°C/5 min/800°C
#14	800°C/50 K min <sup>-1</sup> /1600°C
#15	1600°C/30 min/1600°C
#16	1600°C/-50 K min <sup>-1</sup> /800°C
#17	800°C/5 min/800°C
#18	800°C/15 min/800°C
#19	800°C/5 min/800°C

Table 5.2: Thermal program of the experimental TGA procedure on cerium oxides.

An Ar volume flow rate ( $\dot{V}_{\text{Ar}}$ ) of 80 ml/min was used as purge gas all along the experimental run, except during the oxidation phases, when the CO<sub>2</sub> flow rate was of 40 ml min<sup>-1</sup> in a 50% Ar-50% CO<sub>2</sub> mixture. Data processing has been performed in the following way. First of all, the useful data available were the time vector, with a time step of 0.25 min, the temperature vector around the sample, and the mass variation (in absolute or relative terms) in time with respect to the initial value. These information were available for all the three samples analyzed. No data were recorded by mass spectrometry. Moreover, the analyzer was first run without any sample, to record eventual background noises of the experimental equipment. The actual data were thus purified from this noise to achieve more reliable values. After have evaluated the sample mass just

after each reduction and oxidation, the mass and the corresponding moles of oxygen released were computed. Thus, it was possible to assess the nonstoichiometry,  $\Delta\delta$ , as the moles of atomic oxygen released per mole of ceria (i.e., of cerium). Total volumes (in Sml), average volume flow rates (in Sml min<sup>-1</sup>), productivities (in Sml g<sup>-1</sup>) and production rates (in Sml min<sup>-1</sup> g<sup>-1</sup>) for oxygen were then evaluated. The oxygen volume flow rates and production rates were averaged arbitrarily on the net 30 minutes of reduction at high temperature. This latter passage is not a forced path, but just a possible way to proceed. Exactly the same passages were followed for CO production, with the difference that the time interval used for averaging the values was 15 minutes, that is the duration of the oxidation phase. The reference mass of ceria for evaluating productivities and production rates was fixed at the value just before each reduction for oxygen release, and just before each oxidation for CO production. Finally, an attempt of estimating the thermochemical efficiency of the cycles was proposed.

The mass of the samples is different in the three cases, and for this reason it does make sense to perform the comparisons through referring to percentage mass variations with respect to the initial values. From the lightest to the heaviest, the oxidized, virgin and reduced samples have a mass of roughly 32.24 mg, 44.84 mg and 64.74 mg, respectively. The reduced sample has thus a mass double of the oxidized one. The crystallographic state of the virgin sample is not known in principle. In the following analysis, the cycle 1 has been conceptually kept separated from the other two, because the different initial nature of the samples requires to pay attention to their different behaviour in the first minutes of cycling.

Figure 5.1 shows the results obtained for the cycle 1. Figure 5.1a shows the overall trends, whereas Figure 5.1c shows a detail of what happens in the first minutes: after less than one minute, the oxidized sample shows a peak in mass decreasing, absent in the other two cases, coherently with the fact of being already oxidized. Just afterwards, the mass value returns to values similar to the reduced sample ones. During the heating ramp (see Figure 5.1a) the reduced sample tends to absorb oxygen in the lattice, although the increasing temperature, coherently with the fact of being more reduced and thus poorer in oxygen. Once the 1600°C level has been reached, the reduced sample returns to the initial mass value, confirming its already reduced state before starting the cycle, and maintains fairly constant values. A consistent decreasing in mass is instead observed in the other two cases (oxidized and virgin samples), and a higher percent mass decreasing in the virgin case, that reaches a minimum around 99.4% of the initial mass, against a value around 99.6% for the oxidized sample. During the cooling ramp, the oxidized sample mass increases more rapidly than in the virgin case. The mass increase in this phase is due to the re-absorption of residual oxygen in the system, being still absent a CO<sub>2</sub> stream. In the oxidation phase, during which CO<sub>2</sub> is injected, the oxidized sample is not particularly affected, differently from the other two cases: the steepest mass increase is observed for the reduced sample, as expected, with relatively high values for the first derivative (see Figure 5.1d), until a plateau value is reached (see Figure 5.1a), and maintained for all the rest of the oxidation and of the following thermal stabilization at 800°C, suggesting that the sample is completely oxidized. The virgin sample shows a progressively decreasing first derivative, until the end of the cycle, as can be seen from Figures 5.1a and 5.1d. The overall first derivative information are reported in Figure 5.1b.

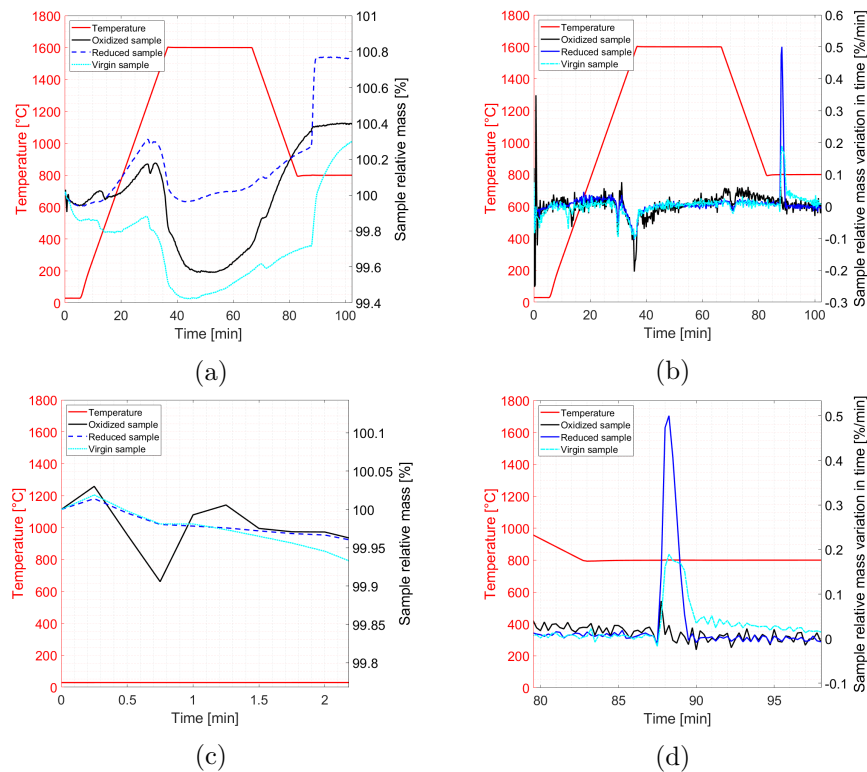


Figure 5.1: TGA results for the cycle 1, together with the temperature evolution vs. time. (a) Relative mass (with respect to the initial value) vs. time for the three samples; (b) First derivative of the relative mass vs. time for the three samples; (c) Detail of (a) in the first minutes; (d) Detail of (b) during the oxidation phase.

Figure 5.2 shows the results obtained for cycles 2 and 3. In general, it is observed that the average percent mass values with respect to the initial ones increase, proceeding from virgin sample, to the oxidized one, to the reduced one. Even in this case, it is useful to observe in parallel the plots referred to the percentage mass variation and to its first derivative in time, respectively shown in Figures 5.2a and 5.2b. As concerns Figure 5.2a, the higher average percent mass value of the reduced sample can be explained through the sample nature itself: being initially reduced, during the following cycles it maintains as expected an average mass higher than the initial value, having absorbed some oxygen (in particular during the first cycle oxidation, as said). Looking at Figure 5.2b, it is observed that all the peaks - both the positive ones referred to oxidation (Figure 5.2c), and the negative ones referred to reduction (Figure 5.2d) - are more intense for the oxidized sample, then following the virgin sample one, and finally the reduced sample ones, with the weakest peak values in absolute value. Rapidity the sample mass varies with is related to the speed at which the reaction is proceeding. In this case, the behaviour of the samples can be related to their absolute mass: the lighter is the sample (i.e., the lighter the reacting mass to process) at a given purge gas (Ar) flow rate sent to the system, the higher the rapidity with which oxygen or carbon dioxide can penetrate in the whole sample and making the reaction to occur. This result is coherent with what has been reported previously from literature, although the systems analyzed are quite different (namely, reactors and TGA): if the mass/mass flow rate of redox reactive material increases, at a given purge gas flow rate, then a higher oxygen partial pressure during the reduction and a lower carbon dioxide partial pressure during the oxidation are induced. This leads to what has been observed here in the results obtained, that is, reduction and oxidation phases more effective in

some sense, under the reaction speed point of view.

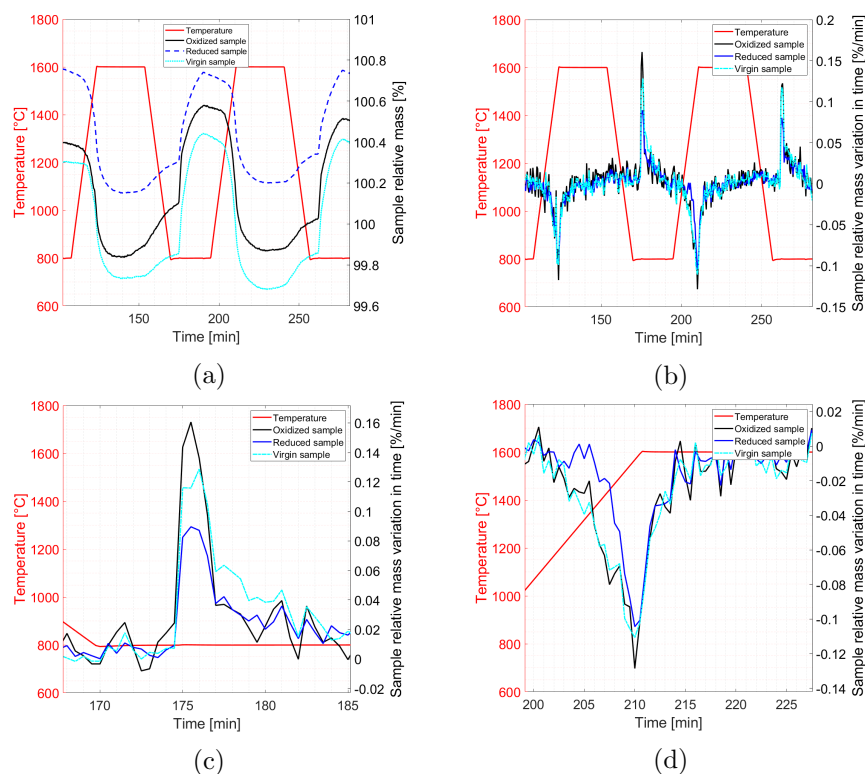


Figure 5.2: TGA results for the cycles 2 and 3, together with the temperature evolution vs. time. (a) Relative mass (with respect to the initial value) vs. time for the three samples; (b) First derivative of the relative mass vs. time for the three samples; (c) Detail of (b) during the oxidation phase; (d) Detail of (b) during the reduction phase.

Figure 5.3a reports the results obtained in terms of average production rates of  $O_2$  and  $CO$  ( $Sml\ min^{-1}\ g^{-1}$ ). Just the cycles 2 and 3 have been considered.  $O_2$  production rates refer as already mentioned to the 30 minutes of net reduction at  $1600^\circ C$ , and to the sample mass immediately before the reduction, whereas the  $CO$  rates to the 15 minutes of net oxidation at  $800^\circ C$ , and to the sample mass immediately before the oxidation. As concerns  $CO$ , the virgin sample showed the highest rates, with more than  $0.5\ Sml\ min^{-1}\ g^{-1}$ . Following, there was the oxidized sample with values in the range  $0.4\text{--}0.5\ Sml\ min^{-1}\ g^{-1}$ , and the reduced one, with values around  $0.4\ Sml\ min^{-1}\ g^{-1}$ . The best rates in terms of  $CO$  yields of the virgin sample can be reconducted to the absence, at the beginning of the sample life, of deleterious effects due to thermal cyclicity. The  $O_2$  rates are all more or less around the value of  $0.1\ Sml\ min^{-1}\ g^{-1}$ . These values are nevertheless subjected to the way in which they are evaluated: if the time interval considered varies, of course the average values will vary as well. Thus, they have to be considered just as indicative values, and function of the definition used for their evaluation. Figure 5.3b reports the same results in terms of overall productivities, whereas  $O_2$  and  $CO$  standard volumes and average volume flowrates, produced for the three samples and for the cycles 2 and 3, can be found in Figure 5.4.

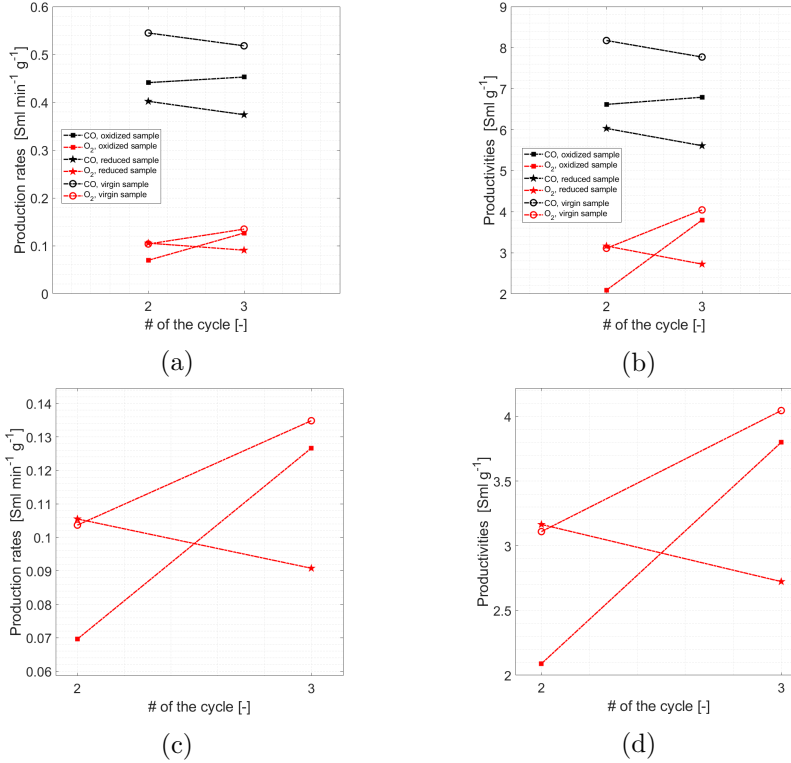


Figure 5.3: O<sub>2</sub> and CO<sub>2</sub> (a) production rates and (b) productivities resulting from TGA for cycles 2 and 3, and for the three samples analyzed; (c) Detail of (a); (d) Detail of (b).

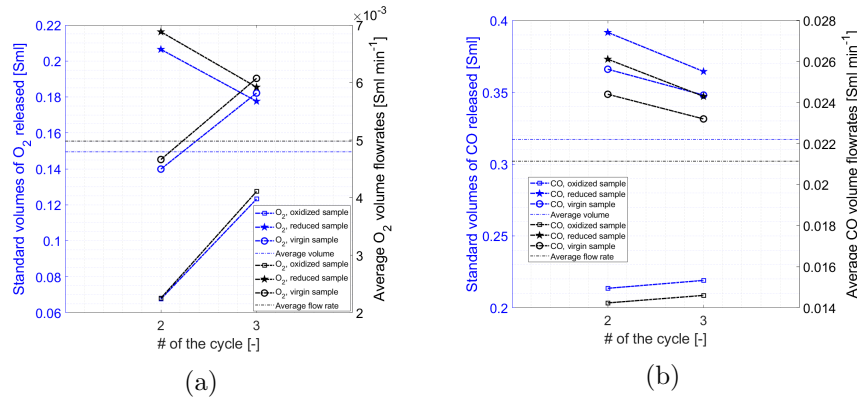


Figure 5.4: (a) O<sub>2</sub> and (b) CO<sub>2</sub> standard volumes and average volume flowrates resulting from TGA for cycles 2 and 3, and for the three samples analyzed.

Figure 5.5 shows the nonstoichiometry  $\Delta\delta$  obtained for cycles 2 and 3 and for the three different samples. As before, the first cycle has not been included here, being inherently not reliable for evaluations of this kind, because of interferences arising at the beginning possibly due to not correct atmospheres near the redox material and to the different initial state of the samples. Indeed, negative values are obtained in cycle 1 for the oxidized and reduced cases. In general, the values obtained for  $\Delta\delta$  are completely comparable with those from literature, although the systems analyzed are, again, quite different (namely, reactors and TGA), as well as the conditions imposed,

such as the reduction temperature. This is for sure a necessary condition for the results obtained here to have a potentially correct meaning. By way of example, the average  $\Delta\delta$  obtained in this analysis is around 0.049, against an average value of 0.0375 obtained through a thermogravimetric analysis by Furler et al. [48], who conducted the reduction at a temperature, slightly lower, of 1773 K instead of 1873 K, and the oxidation at 1273 K instead of 1073 K. What is observed is first of all an increase in  $\Delta\delta$  from cycle 2 to cycle 3 for the oxidized and virgin samples, and a decrease for the reduced sample. The virgin sample induces a  $\Delta\delta$  always higher than the oxidized one, whereas the reduced one leads to the highest value among the three in cycle 2, and to the lowest value among the three in cycle 3. This latter consideration as concerns the reduced sample can be explained observing that in cycle 2 the reduced sample is affected by the complete oxidation that follows the cycle 1 (in which the minimum mass reached during reduction was roughly equal to the initial value), while in cycle 3 is instead affected by the oxidation following the cycle 2, that is weaker. In other words: the fact that the sample is initially reduced leads to a very effective oxidation in cycle 1, and consequently to a considerable oxygen release in cycle 2. This effect is weakened in cycle 3. In the case of the oxidized sample, the  $\Delta\delta$  for cycle 3 is almost double than the one for cycle 2. Being the percent mass reached during reduction roughly the same in the two cycles (99.8-99.9%), this effect is the consequence of a percent mass increase much higher in the second oxidation than in the first one (increase of 0.2%). A further comment is noteworthy: from Equations 4.4 to 4.6 it is clear how the  $\Delta\delta$  can be actually interpreted in two different ways, i.e., either as moles of oxygen released per mole of ceria or as moles of fuel produced per mole of ceria. These two definitions coincide only in the case of identically repeating cycles, i.e., up to identical reduction and oxidation extents. This is no more true if cycles are slightly different one from the other, as happens in the reality: in this case, the first interpretation (related to the oxygen released) holds if  $\Delta\delta$  is evaluated considering a given oxidized state and the *following* reduced state, whereas the second interpretation (related to the fuel produced) holds if  $\Delta\delta$  is evaluated considering a given oxidized state and the *previous* reduced state. In this analysis, the oxygen-related definition was adopted.

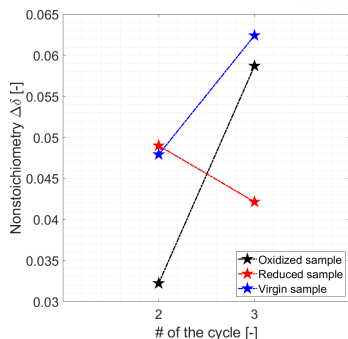


Figure 5.5: Nonstoichiometry  $\Delta\delta$  resulting from TGA, for cycles 2 and 3, and for the three samples analyzed.

Table 5.3 summarizes and compares the average results retrieved from literature and the average outcomes of the present work, in terms of nonstoichiometry reached and CO productivities and production rates. This comparison is useful to just get at glance the similarity among the different results, although the experimental conditions implemented are slightly different, e.g. in terms of temperatures, flowrates, typology and masses of ceria samples. The most consistent comparison is for sure the one with the results from Furler et al. [48], being both the works based on a TGA.

Chueh et al. [33]	Scheffe et al. [38]	Welte et al. [39]	Furler et al. [48]	Present work
$\Delta\delta$ [-]				
-	0.035	0.0162-0.0463	0.037-0.038	0.049
<b>CO production rates [Sml min<sup>-1</sup> g<sup>-1</sup>]</b>				
1.6	-	-	0.22-2.22	0.46
<b>CO productivities [Sml g<sup>-1</sup>]</b>				
7	-	-	-	6.83

Table 5.3: Summary and comparison among the literature results and the outcomes of the present work, as concerns nonstoichiometric ceria.

In terms of thermochemical conversion efficiency, the definition adopted is the following:

$$\eta_{\text{thchem,CO}} = \frac{n_{\text{CO}} HV_{\text{CO}}}{\int P_{\text{th}} dt + E_{\text{Ar}} \int \dot{n}_{\text{Ar}} dt} \quad (5.1)$$

This expression has the same meaning of Equation 4.13 above, with the difference that the power delivered is a purely thermal one, and not solar-derived high temperature heat. The numerator is the output energy, given by the product between the moles of CO produced ( $n_{\text{CO}}$ ) and the molar heating value of CO ( $HV_{\text{CO}}$ ), equal to 281.4 kJ/mol. The Ar molar flow rate ( $\dot{n}_{\text{Ar}}$ ) used was of 80 ml/min. The denominator contains the integral thermal energy delivered to the system ( $\int P_{\text{th}} dt \equiv Q_{\text{th}}$ ) and the energy required to separate the whole Ar molar flow rate. Let's precise that the heat is delivered inside the thermogravimetric analyzer through an electrical feeding. If the process is run making use of solar radiation, then the efficiency will be a *solar-to-fuel* one. Herein, it was estimated an average value for the efficiency for the whole cycle, and for each cycle, and not instantaneous ones. A precise estimation is very difficult to be performed, because several factors and parameters should be taken into account, and they are difficult to be assessed, in particular for the thermal power delivered to the furnace. At least the two following items can be listed:

i. Thermal losses towards the external environment, e.g. of convective nature on the external boundaries of the whole system. Not only they are difficult to be evaluated, but they even vary along the cycle, because the reaction temperature is varying in time as well. In the approach proposed herein, they have been fixed arbitrarily to 2% of the total thermal power delivered to the system;

ii. Reduction/oxidation enthalpy: indeed, to be precise, it should be taken into account in the thermal balance also the heat absorbed by the sample to reduce, and the heat released by the sample to oxidize. Being the masses involved of the order of milligrams, this contribution was neglected.

Thus, the thermal energy delivered to the system ( $Q_{\text{th}}$ ) has been estimated through taking into account just the heating ramp of the cycle: the two contributions are therefore the sensible heat delivered to the ceria sample and to the Ar flow rate, to heat them up from 800°C to 1600°C. The constant temperature phases are in some way included through the thermal losses (i.e., at steady state, the thermal power from the external has to balance just the eventual reaction enthalpy, that was neglected, and thermal losses). The cooling ramp was not considered, since it can be argued that the heat is flowing from the system towards the external. Even for these sensible heat contributions some approximations were needed. Indeed, both the specific heat capacities of ceria and argon have been considered as constant with temperature. In addition, the specific heat of ceria varies also with the nonstoichiometry  $\delta$ : an indicative value of 0.523 J g<sup>-1</sup> K<sup>-1</sup> was extrapolated from literature [51]. Moreover, the mass of the ceria sample was considered as constant during

the cycle in the efficiency formula, and equal to the initial value for each cycle (i.e., just after the previous oxidation), although it varies, because the variations are very small. The specific heat capacity of argon was fixed at  $20.8 \text{ J mol}^{-1} \text{ K}^{-1}$ . The time interval for integration was considered thus to be 16 minutes for the thermal power, and 87 minutes (whole duration of the cycle) for the argon separation power. Summarizing, if the thermal efficiency of the system is fixed at  $\epsilon = 98\%$  as concerns the thermal losses, the overall thermal balance leads to the following expression for  $Q_{\text{th}}$ , taking into account all the hypotheses just mentioned:

$$Q_{\text{th}} \approx \frac{mc_p\Delta T|_{\text{CeO}_2} + \dot{n}c_p\Delta t\Delta T|_{\text{Ar}}}{\epsilon} \quad (5.2)$$

Results obtained in terms of efficiencies for cycles 2 and 3 are shown in Figure 5.6. It can be observed an increase in the efficiency for the oxidized sample, and a decrease in the other two cases, proceeding from the cycle 2 to the cycle 3. All the values obtained are of the order of  $10^{-2}\%$ , and the highest are the ones referred to the reduced sample. The overall average value is around  $0.055\%$ , whereas the peak value is around  $0.068\%$ , reached by the reduced sample in cycle 2. The values retrieved from literature are of the order of  $10^{-1}\%$  if hydrogen production is considered instead of CO (Table 4.1, Welte et al. [39]), and of the order of 1-2% in case of a solar cavity reactor-receiver is used [48]. Although these values were obtained in slightly different conditions in terms e.g. of technology, material and temperatures, and using slightly different analytic expressions, values and hypotheses, they are qualitatively comparable at all, keeping in mind that a more reliable comparison should come for sure from as much similar as possible experimental operating conditions and definition adopted.

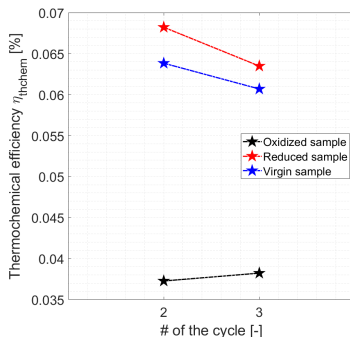


Figure 5.6: Thermochemical efficiencies resulting from TGA, for cycles 2 and 3, and for the three samples analyzed.

To present some results related to the kinetics of the process, it is now needed to introduce some definitions according to what is usually reported in the references [53]. If  $m(t)$  is the sample mass at time  $t$ ,  $m_0$  its initial value at time  $t = 0$ , and  $m_\infty$  the stoichiometric mass of the fully reacted sample (or simply the mass of the reacted sample up to the reaction extent considered), then the *temporal conversion function*  $\alpha(t)$  is defined as follows:

$$\alpha(t) = \frac{m(t) - m_0}{m_\infty - m_0} \quad (5.3)$$

The function  $\alpha(t)$  gives information on how fast the sample mass crosses the mass interval considered (or the stoichiometric mass interval, if the full reaction is taken into account), starting from the initial value to the reacted (or fully reacted) one. It is applicable both to the reduction and oxidation

phases. In this analysis, a complete cycle is defined as the corresponding reduction summed up to the following oxidation. As regards the results obtained for the ceria samples and presented so far, (i) the reduction initial mass  $m_{0,\text{red}}$  was defined as the mass value just before the mass dropping down, at the end of the previous oxidation, with corresponding  $m_{\infty,\text{red}}$  equal to the minimum mass reached during the reduction, whereas (ii) the oxidation initial mass  $m_{0,\text{ox}}$  was defined as the mass value just before the oxidation, with corresponding  $m_{\infty,\text{ox}}$  equal to the reacted mass at the end of the oxidation. The definition adopted for  $m_{\infty,\text{red}}$  comes from the fact that during the cooling ramp the sample mass tends to increase again, as said, possibly due to residual oxygen in the reaction site. Thus, it does make sense to consider just the actual mass decreasing part. Results in terms of conversion  $\alpha(t)$  are shown in Figure 5.7. As concerns the reduction phases, although the reduced sample seems to react faster at the beginning, the higher slope is reached by the oxidized one, as shown in Figure 5.7c. As concerns the oxidation phases, all the three samples tend to react rapidly at the beginning (Figure 5.7d) for roughly two minutes, and then a sudden decrease in the slope is observed. A comment of relevance is that the highest slope for higher and higher times is the one for the initially reduced sample, that seems to oxidize faster. A further consideration is that whereas the final slope for reduction nearens a zero value (actually this happens *by construction*, since the minimum mass value was taken), this does not happens for the oxidation, meaning that this latter is not at all complete when the  $\text{CO}_2$  feeding is cut. The importance of dealing with  $\alpha(t)$  has to do with its first derivative in time, that under an experimental point of view represents the reaction rate  $r(t)$  of the process observed:

$$r(t) = \frac{d\alpha}{dt} \quad (5.4)$$

In this framework,  $r(t)$  is measured in  $\text{s}^{-1}$ . The numerical values of the corresponding reaction rates for the cycles analysed are shown for completeness in Figure 5.8: it can be observed that almost in all the cases the rate at which the reaction proceeds slows down passing from cycle 2 to cycle 3, possibly because of some cyclicity effects that arise in the samples. The highest rates are around  $0.2 \text{ s}^{-1}$  for reduction and around  $0.25\text{-}0.35 \text{ s}^{-1}$  for oxidation.

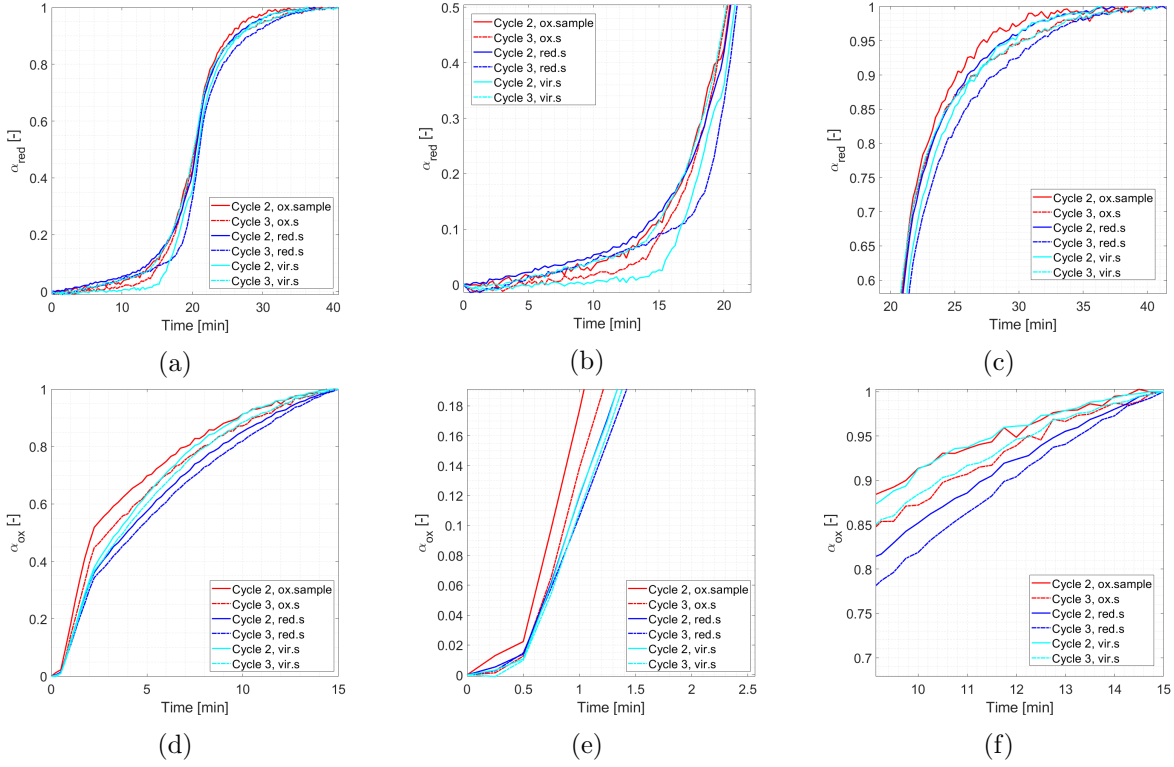


Figure 5.7: (a)  $\alpha(t)$  for the reduction reactions; (b), (c) Details of (a); (d)  $\alpha(t)$  for the oxidation reactions; (e), (f) Details of (d).

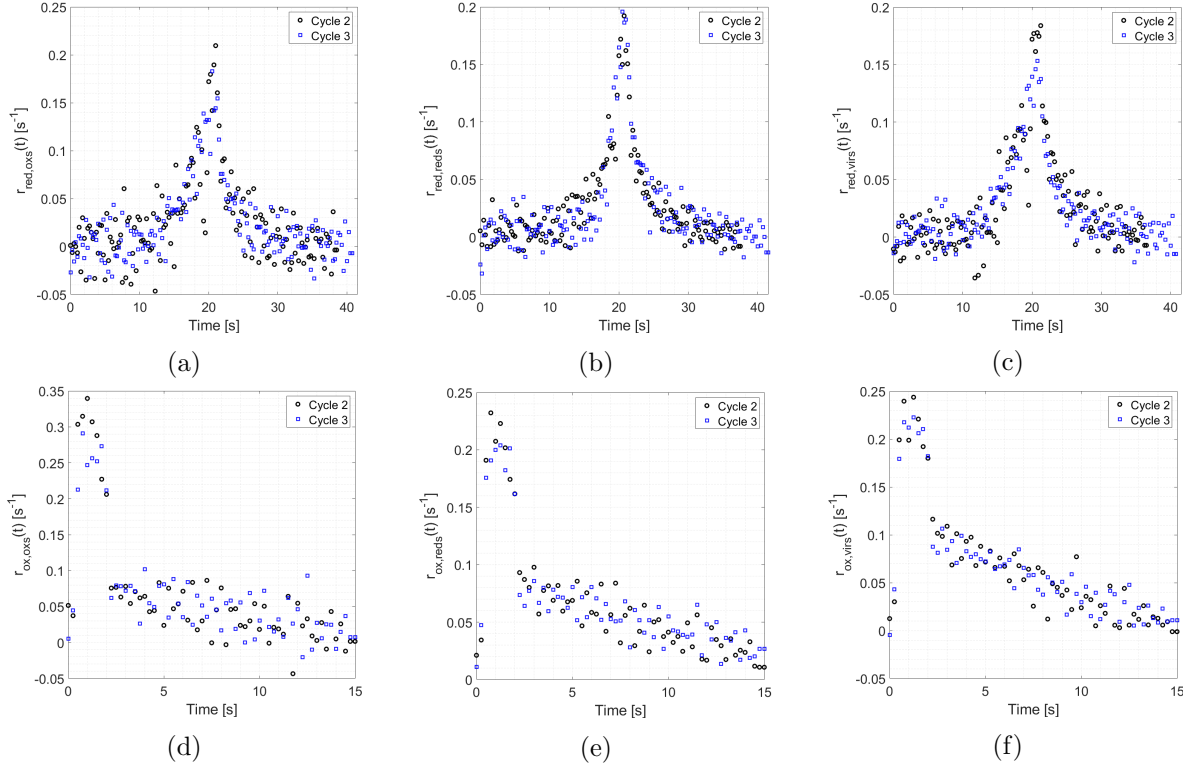


Figure 5.8: Reaction rates for the oxidized, reduced and virgin samples: (a), (b) and (c) Reduction phases; (d), (e) and (f) Oxidation phases.

## 5.2.2 TGA on iron oxides

The TGA with iron oxides, again through the STA 2500 Regulus thermogravimetric analyzer, was performed in three steps, using as raw material a  $\text{Fe}_2\text{O}_3$  powder available at the laboratory scale. The powder was not characterized in terms of specific properties, and was used as it was. The three experimental subparts will be described in the order below.

**5.2.2.1 First part. Thermal reduction and air-based oxidation cycle** A first experimental procedure, referred to as *test#1* in the following, was run taking as a reference the work by Bush and Loutzenhiser [53]. After having heated up the sample to 1623 K in Ar starting from ambient temperature and through a ramp of  $20 \text{ K min}^{-1}$ , 10 isothermal redox cycles were performed at this thermal level. Each cycle was composed of a thermal reduction in 100% Ar ( $80 \text{ ml min}^{-1}$ ) and of an oxidation in 50% air-50% Ar ( $40 \text{ ml min}^{-1} + 40 \text{ ml min}^{-1}$ ), since the analyzer requires a protective gas flowrate at all times. The sample mass for the *test#1* was around 21.495 mg. The thermal program just described is reported in Table 5.4.

Figure 5.9 reports the TGA output in terms of relative sample mass. The initial mass decrease shown in Figure 5.9a has not to be considered, since it is due to the mass stabilization inside the analyzer. It has been chosen here to discard the first 4 cycles as well, being the mass not yet fully stabilized in this first half of the experiment. The aim was to analyse the sample behaviour at a sort of steady state operation, when cycles seem to repeat themselves in a kind of regular way. The last 5 cycles - i.e., the ones studied - are reported in Figure 5.9b for sake of ready visualization.

Segment	$T_{\text{start}}$ /duration or slope/ $T_{\text{end}}$
#1	20°C/5 min/20°C
#2	20°C/20 K min <sup>-1</sup> /1350°C
#3	1350°C/15 min/1350°C
...	...
...	...
...	...
#23	1350°C/15 min/1350°C
#24	1350°C/-20 K min <sup>-1</sup> /25°C

Table 5.4: Thermal program of the *test#1* experimental TGA procedure on iron oxides.

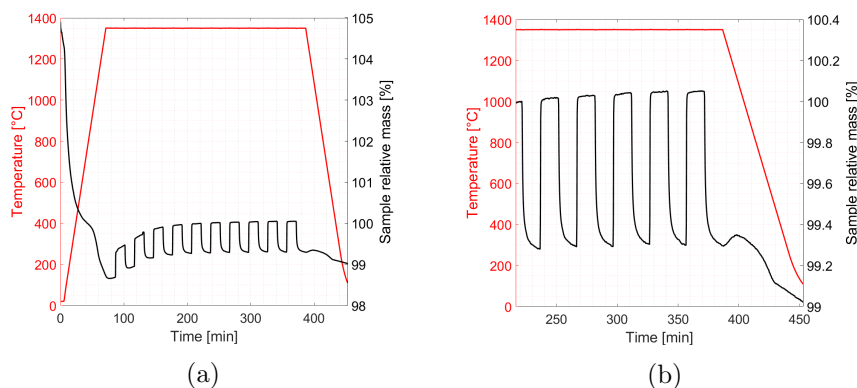


Figure 5.9: Relative mass representations of (a) all the 10 cycles performed and of (b) the last 5 cycles performed, i.e., the ones studied.

Since just the last 5 cycles were studied, the initial sample mass previously reported was replaced with an *apparent* initial mass value, equal to the absolute oxidized mass just after the oxidation in the fifth cycle. This can be noticed even from the percent value on the right y axis in Figure 5.9. From the fifth cycle on, the oxidized mass seems to reach higher and higher values, and this corresponds to reach values slightly higher than the apparent initial one. The cycles were then superimposed as done in the reference work. Figure 5.10 reports, in the order, the cycles representation from Bush and Loutzenhiser [53], and their representation from the present analysis, with and without a full conversion reference level (dotted black line). This latter is the mass level reached in the hypothesis of full conversion towards the  $\text{Fe}_3\text{O}_4$  phase, supposing that the initial mass was  $\text{Fe}_2\text{O}_3$ . What can be observed at glance is that, while in the reference work this level is well reached, this does not happen in the present one, in which the sample mass seems to nearen a well higher plateau value. The reasons could lie in unknown factors, such us different absolute sample masses or different characteristics of the sample in terms of structure, actual oxidation state and particle size, and in known factors, such us the lower purge gas volume flowrate used in the present experiments ( $80 \text{ Nml min}^{-1}$  instead of  $120 \text{ Nml min}^{-1}$ ), that leads in principle to a higher oxygen partial pressure around the sample, and thus to a lower reduction extent. Moreover, the powder used contained also other heteroatoms in small quantities, and this would reduce the actual hematite mass in the sample.

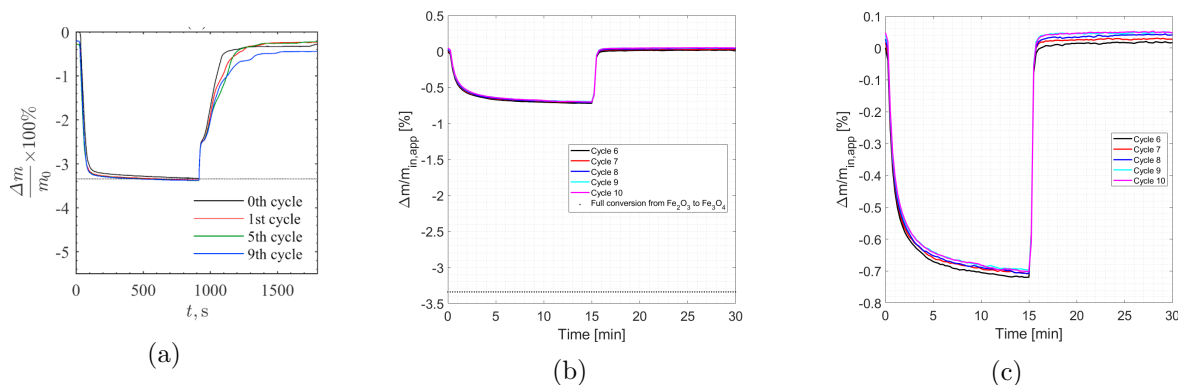


Figure 5.10: Cycles representation: (a) plot from Bush and Loutzenhiser [53]; plots from the present analysis, respectively (b) with and (c) without full conversion reference level.

Kinetic results are now shown, as done for the cerium oxides. Also here, a complete cycle is defined as the corresponding reduction summed up to the following oxidation. Thus, for each cycle, (i) the reduction initial mass  $m_{0,red}$  was defined as the mass value just before the mass dropping down, with corresponding  $m_{\infty,red}$  equal to the reacted mass at the end of the reduction, whereas (ii) the oxidation initial mass  $m_{0,ox}$  was defined as the mass value just before the mass rising up (minimum value reached in each cycle), with corresponding  $m_{\infty,ox}$  equal to the reacted mass at the end of the oxidation. These definitions led to the trends reported in Figure 5.11 below. What it is observed from Figure 5.11a is that its first derivative does not reaches actually a zero value (plateau level), meaning that probably the reduction was not complete. As concerns instead Figure 5.11b, what can be highlighted is that the first derivative is much higher at the beginning with respect to the reduction case, and then apparently reaches a zero value (plateau level). The oxidation plateau suggests that the sample has reached the equilibrium oxidized state: this is consistent with the experimental operating conditions involving a flowrate of air entering the system, that leads to a relatively higher oxygen partial pressure around the powder, determining a definitely effective oxidation process.

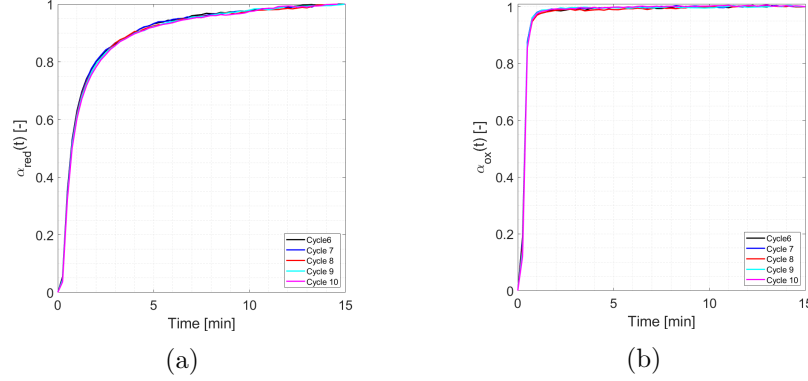


Figure 5.11: Temporal conversion function  $\alpha(t)$  for (a) reduction and (b) oxidation phase, for the 5 cycles studied.

The reaction rates for the reduction and oxidation phases for all the 5 cycles is shown in Figure 5.12. It is worth noticing that the time step of 15 s coming from the experiments seems to be extremely large for the aim of these observations: during both the cycles phases, the maximum values region for  $r(t)$  is captured by just one point, and this inhibits to have a precise idea about its actual trend in time. Both for reduction and oxidation, just the first 5 minutes have been plotted, over a total of 15 min for each phase. The black dashed curves represent an interpolation of the average rates among the 5 cycles. In particular, in Figure 5.12a, the average profile for the reduction was built as a cubic curve: the aim was just to better visualize a *possible* shape for the actual reaction rate function, but it *does not* reproduce in any sense the actual behaviour of the rate. The interpolation for the oxidation (Figure 5.12b) was built instead as a linear one, again just for sake of visualization: it is highlighted in this case how the quantity of data available are too poor - especially in the first region, at lower times - to estimate in a precise way a probable functional shape for the reaction rate. Figures 5.13a to 5.13f show some details on the rate trends, in the order, at the initial time instant, at the peak (or better, the highest value detected) and in the *tail* of the curve: as concerns the reduction (Figures 5.13a to 5.13c), the initial rate decreases proceeding towards later cycles, and so does the peak rate, except for the last two values, while no particular correlations with the number of cycle is observed in the tail of the curve; as concerns the oxidation (Figures 5.13d to 5.13f), the initial rate decreases again for later cycles, but the peak value increases, and also here no correlations seem to exist for later and later times. Summarizing, the reduction phases are possibly affected by the cyclicity effects e.g. as regards the powder structure and particle size, whereas the oxygen-aided oxidation does not. A further representation of the relative behaviour among cycles is given in Figure 5.14 from the reference work [53] as comparison, and in Figure 5.15 for the present results: in the latter, a parity plot is reported for both of the cycles phases, for all the cycles, where the rates of cycles 7 to 10 are compared to the 6<sup>th</sup>'s one (the first one of the cycles studied). In both the analyses, and according to the  $\alpha$  definition and respective reference values used for its calculation, later cycles values tend to lie below the reference line during the reduction, with corresponding values always lower than the earlier ones, whereas during the oxidation later cycles tend to lie above the earlier ones, i.e., later cycles seem to show a more rapid oxidation, and this happens all along the oxidation itself.

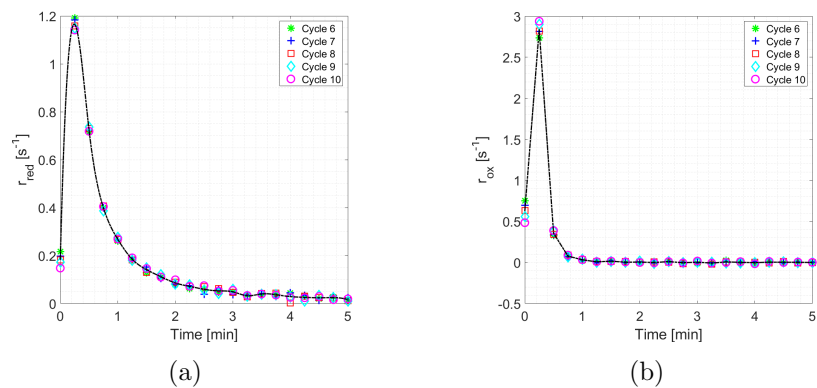


Figure 5.12: Experimental reaction rates  $r(t)$  for (a) reduction and (b) oxidation phase, for the 5 cycles studied and for the first 5 minutes over a total of 15 min of each phase.

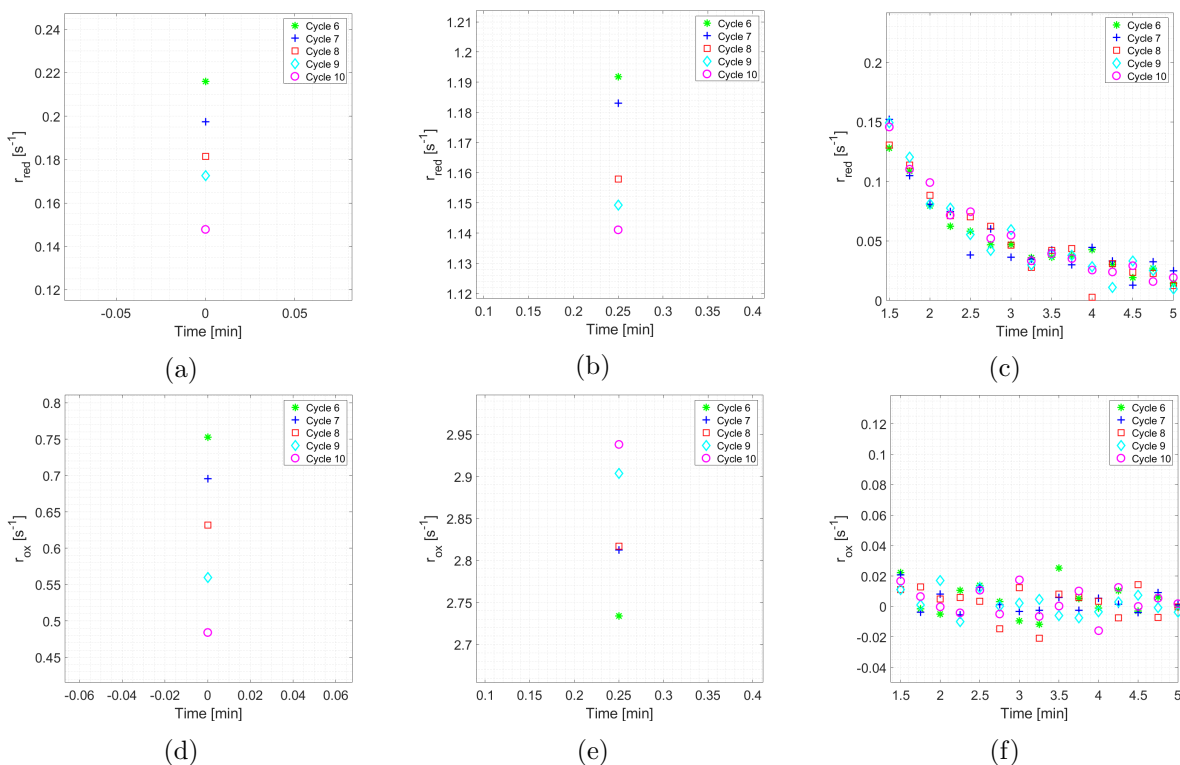


Figure 5.13: Details on the reaction rates curves: initial time instant, highest value detected and tail of the curve, respectively for (a, b, c) reduction and (d, e, f) oxidation phases.

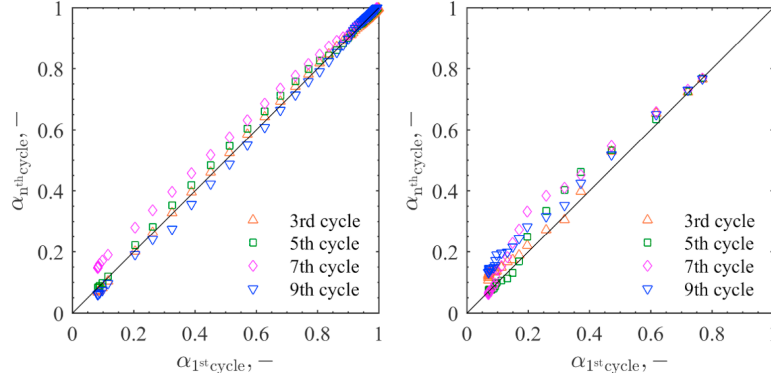


Figure 5.14: Parity plots for reduction (left) and oxidation (right) phases from the reference work [53].

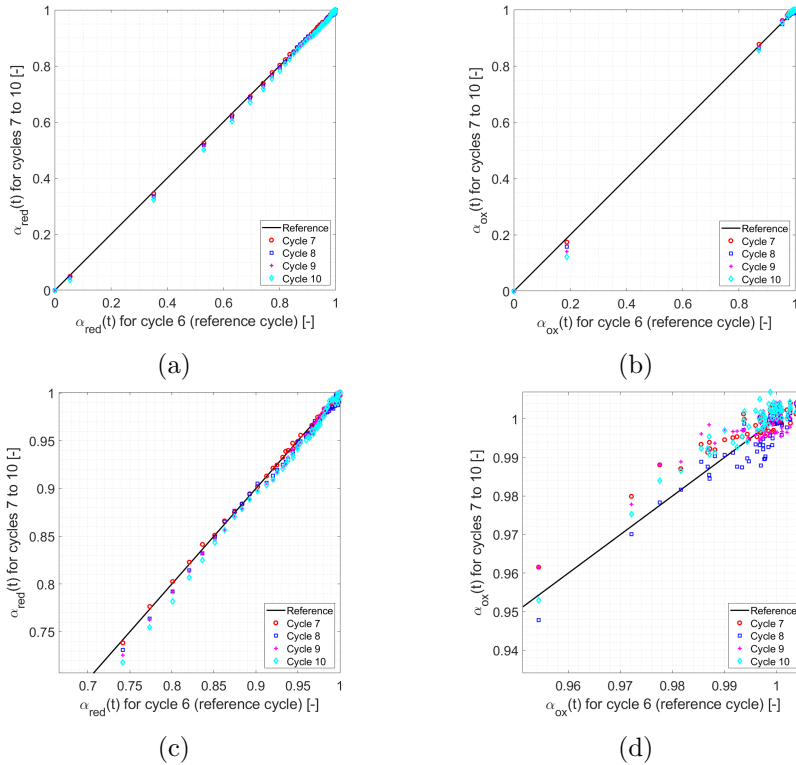


Figure 5.15: Parity plots for (a) reduction and (b) oxidation phase of the 5 cycles studied; (c) Detail of (a); (d) Detail of (b).

To complete the picture of this first experimental part, the results in terms of  $O_2$  production during the reduction phase will be now summarized. The oxidation phase is not useful at this stage, since no fuel productivity is observed because of the air (pure oxygen) feeding. Figure 5.16 reports, in the order, the standard volumes and the standard volume flowrates of oxygen released, the oxygen productivities and the oxygen production rates, these latter two being expressed both in terms of standard volumes and in terms of amount of substance. From the definition of cycle used in this analysis (i.e., reduction plus subsequent oxidation), it follows that the oxygen released in a given cycle was evaluated as the mass variation with respect to the oxidized mass of the previous

cycle. This reasoning is coherent with the previous discussion on cerium oxides. The reference time interval for evaluating average quantities such as the volume flowrates and the production rates was fixed at 15 min, that is the duration of the reduction phase. Finally, the reference mass for evaluating the productivities and the production rates was fixed at the value at the end of the previous oxidation, as it is reasonable to do. The last reduction just before the cooling ramp was neglected from the whole analysis.

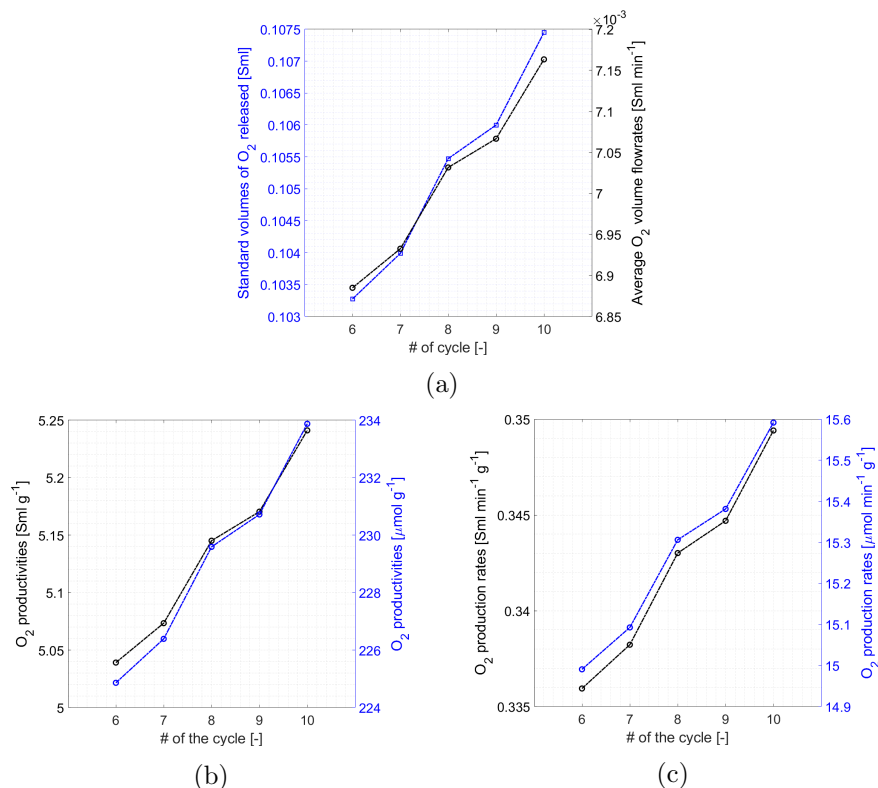


Figure 5.16: O<sub>2</sub> results for the 5 cycles studied: (a) Standard volumes and average standard volume flow rates; (b) Productivities; (c) Production rates.

**5.2.2.2 Second part. H<sub>2</sub>-aided reduction and CO<sub>2</sub>-based oxidation cycle** The second experimental procedure that was performed, referred to as *test#2* in the following, will be described from now on, and all the outcomes will be reported basically in the same way as was done for *test#1* above.

The literature reference for this second part was the work by Farooqui, Santarelli and Llorca [54]. After having heated up the sample to 1073 K in Ar starting from ambient temperature and through a ramp of 20 K min<sup>-1</sup>, 5 isothermal redox cycles were performed at this thermal level. Each cycle was built as a H<sub>2</sub>-aided reduction, using a mixture of 50% Ar-50% reducing gas, on its own composed of 1% H<sub>2</sub>-99% N<sub>2</sub>, for a total volume flow rate of 80 ml min<sup>-1</sup>, and a CO<sub>2</sub> oxidation, with a mixture of 20% CO<sub>2</sub>-80% Ar, for a total volume flow rate fixed again at 80 ml min<sup>-1</sup> (16 ml min<sup>-1</sup> CO<sub>2</sub> + 64 ml min<sup>-1</sup> Ar). The sample mass for the *test#2* was around 28.02 mg (same powder used in *test#1*). Reduction and oxidation, whose duration was fixed respectively at 15 min and 30 min, were interspersed through 5 min long stabilization phases. The thermal program is shown in Table 5.5 (segments #3 to #6 repeat other three times in the middle).

Segment	$T_{\text{start}}$ /duration or slope/ $T_{\text{end}}$
#1	20°C/5 min/20°C
#2	20°C/20 K min <sup>-1</sup> /800°C
#3	800°C/15 min/800°C
#4	800°C/5 min/800°C
#5	800°C/30 min/800°C
#6	800°C/5 min/800°C
...	...
...	...
...	...
#19	800°C/15 min/800°C
#20	800°C/5 min/800°C
#21	800°C/30 min/800°C
#22	800°C/-20 K min <sup>-1</sup> /25°C

Table 5.5: Thermal program of the test#2 experimental TGA procedure on iron oxides.

The TGA output is reported in Figure 5.17, as already done for the previous part. The same definition as before for a given cycle was maintained, i.e., each cycle is considered to be formed by a given reduction and the following oxidation. Also in this case, the data available at shorter times were discarded, and just the last 4 cycles were analysed. The apparent initial mass value was fixed at the same value reached at the end of the second cycle oxidation, although it is actually reached - in the first, discarded cycle - during the reduction phase. As already said before, no precise information were available on the actual structure of the sample along the experiments, in terms of oxidation state of the powder. One more comment is that the analysis was stopped at the end of the last oxidation, i.e., 30 minutes after the last CO<sub>2</sub> feeding, and this implies that the last portion of the curve - the one corresponding to the cooling ramp - was neglected.

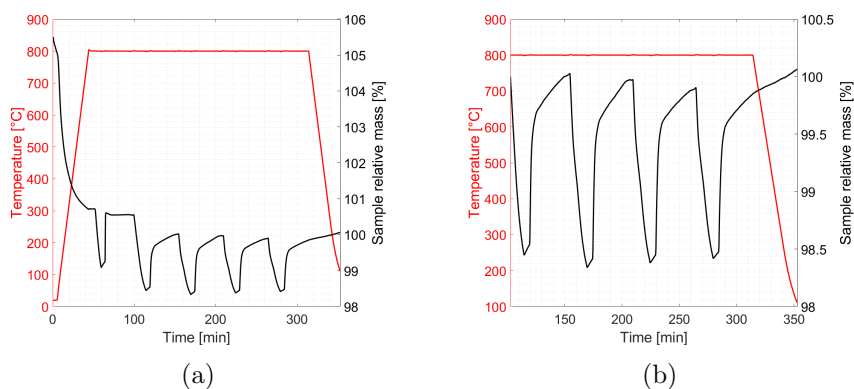


Figure 5.17: Relative mass representations of (a) all the 5 cycles performed and of (b) the last 4 cycles performed, i.e., the ones studied.

Figure 5.18 reports the 4 cycles studied superimposed on each other, again with (left) and without (right) a reference fully reacted mass level. Since the reoxidation from Fe<sub>3</sub>O<sub>4</sub> towards Fe<sub>2</sub>O<sub>3</sub> is not thermodynamically favoured in the presence of CO<sub>2</sub>, as mentioned in the literature review part, the analysis here was conducted supposing that the apparent initial mass was in the Fe<sub>3</sub>O<sub>4</sub> phase, and the reference conversion value was estimated from stoichiometry considering a fully

reduction towards FeO. The considerations done for test#1 are again valid, and several factors could contribute to the high distance that separates the mass values obtained and the theoretical fully reacted ones: first among all, the unknown nature of the sample, as already mentioned, in terms of structure, phase, composition (heteroatoms present in small quantities) and particle size, that determine the theoretical mass reachable through reduction or oxidation, and the practical way in which this can happen under a kinetic point of view. An interesting point is that the mass variation slope at the end of each reduction is well far from being zero, meaning that the sample seems not at all to be fully reacted (i.e., reduced). This could come from the H<sub>2</sub>-aiding in the reducing gas feeding, that would tend to enhance the effectiveness of the process.

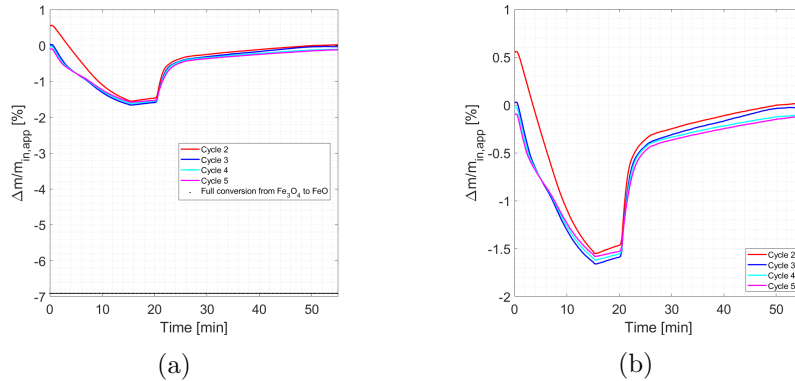


Figure 5.18: Cycles representation: plots from the present analysis, respectively (a) with and (b) without full conversion reference level.

Figure 5.19 shows the reaction rate  $r(t)$  for the reduction (left) and the oxidation (right) phase, and for the 4 cycles studied. Looking at the rates values, it is again evident how the reduction is not at all complete after 15 minutes (i.e.,  $\alpha_{red}(t)$  - not shown here for sake of conciseness - has a non-zero positive slope). Moreover, as concerns reduction (Figures 5.19a and 5.19c), it is clear how the rate reaches higher and higher values proceeding from one cycle to the next one at shorter times, before reaching the absolute maximum, and then it drops to lower and lower values, from one cycle to the next one, after the peak. This trend is reversed during the oxidation (Figures 5.19b and 5.19d), that instead looks to be nearly complete (plateau value in  $\alpha_{ox}(t)$ ). In other words: proceeding from one cycle to the following one, the oxygen release becomes faster and faster (i.e., concentrated in smaller time intervals), whereas the CO production tends to slow down (i.e., to spread in larger time intervals). Figure 5.20 reports a parity plot representation of the relative behaviour among the cycles studied, that corresponds to an alternative perspective for looking at the same results: as concerns the reduction, for shorter times the later cycles seem to correspond to faster reaction extent variation, and the trend among cycles is reversed for later times; as concerns oxidation, for shorter times later cycles show slower oxidation extent, and then tend to superimpose for later and later times.

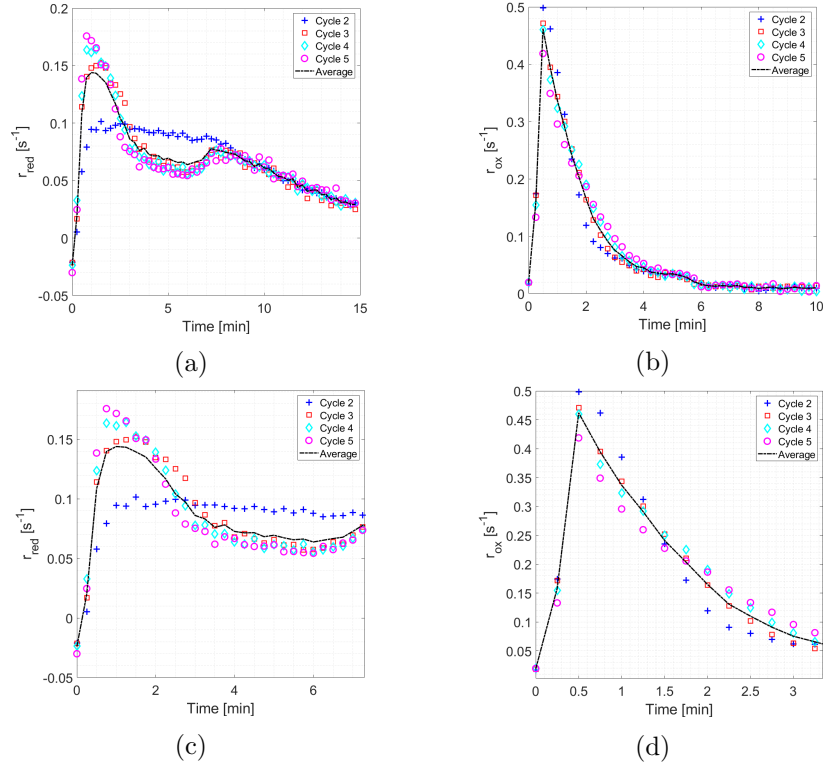


Figure 5.19: Experimental reaction rates  $r(t)$  for (a) reduction and (b) oxidation phase, for the 4 cycles studied and respectively for the 15 minutes of reduction and for 10 minutes over a total of 30 min of oxidation; (c) Detail of (a); (d) Detail of (b).

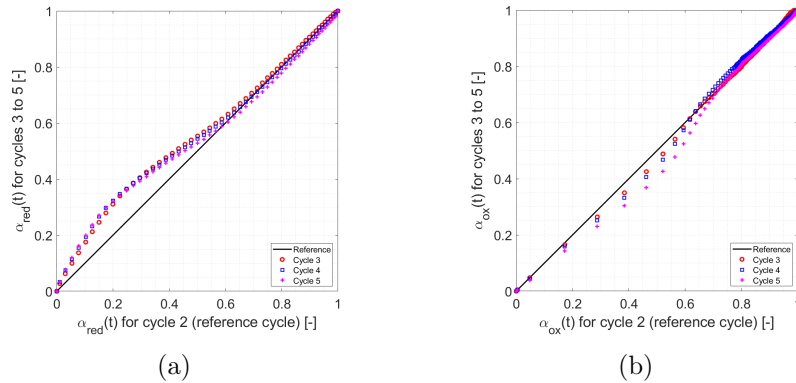


Figure 5.20: Parity plots for (a) reduction and (b) oxidation phase of the 4 cycles studied.

Finally, Figure 5.21 reports the outcomes in terms of volumes and average volume flow rates of O<sub>2</sub> (left) and CO (right), whereas Figure 5.22 shows the results in terms of O<sub>2</sub> and CO productivities and production rates, for the four cycles studied. Values are averaged in time considering 15 min of net reduction for the O<sub>2</sub>, and 30 min of net oxidation for the CO. Moreover, the O<sub>2</sub> values are referred to the mass just after the previous oxidation (when starts the stabilization phase), while the CO values refer to the mass just before the subsequent oxidation (after the stabilization phase). It is worth to notice that here an equivalent amount of oxygen extracted was evaluated, since the output mixture will contain actually also some water vapour because of the H<sub>2</sub> feeding.

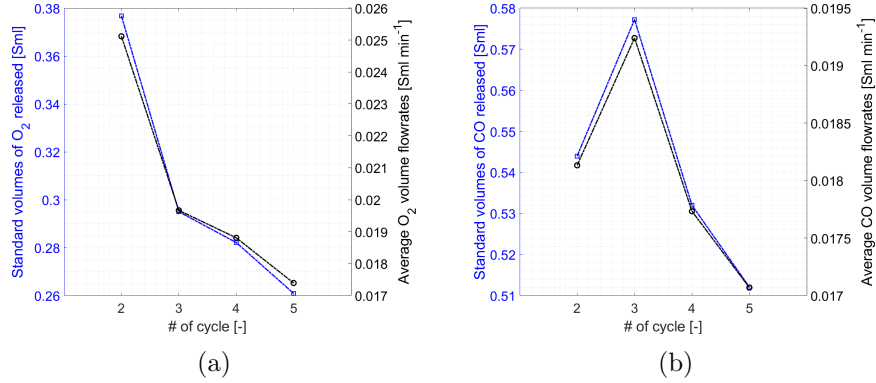


Figure 5.21: Standard volumes and standard volume flow rates for (a) O<sub>2</sub> released and (b) CO produced.

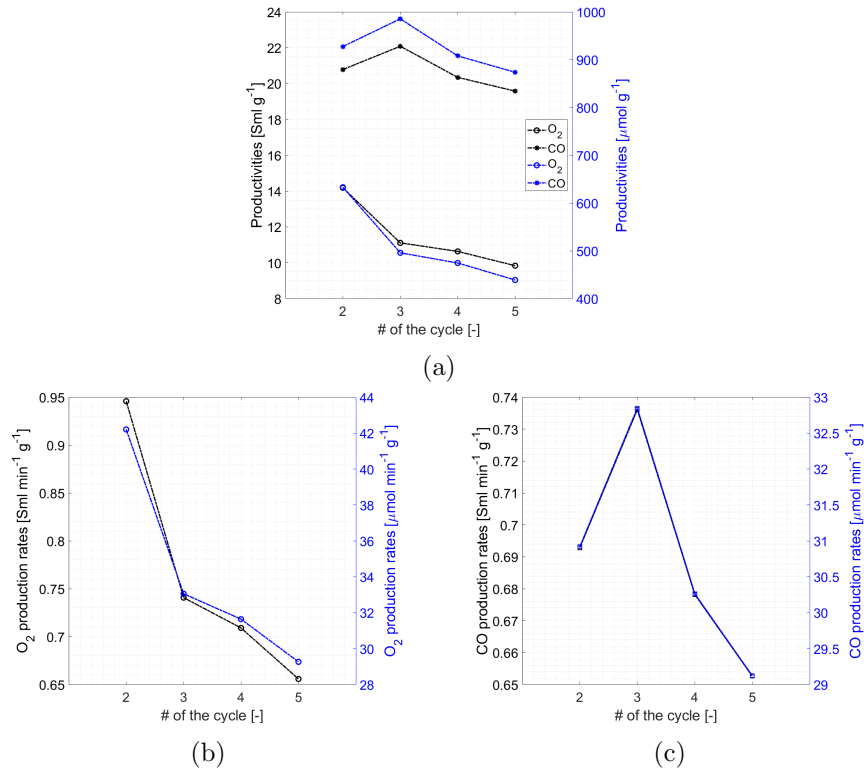


Figure 5.22: (a) O<sub>2</sub> and CO productivities; (b) O<sub>2</sub> production rates; (c) CO production rates.

A comparison with the literature results in terms of CO yields is now reported. The CO productivities from the work by Abanades et al. [50] and from the present analysis are compared in Table 5.6, in which also a description of the operating conditions is reported. Both the oxidation experiments were conducted in isothermal conditions, but results from the reference are higher than the present ones: this could be explained at least by the different times considered for the reaction to proceed and by the different CO<sub>2</sub> concentration in the feed, higher in the reference work. The oxidation temperature was fixed at 800°C in both of them. The CO productivities from the reference work by Farooqui et al. [54] are instead compared with the present results in Table 5.7. Also in this case, the different results are explained by the different operating conditions implemented in the two

cases. At least three reasons can be identified: firstly, in Farooqui et al. [54] the reduction phase was 30 min long instead of 15 min, thus allowing for a higher reduction extent, and thus potentially for a higher CO productivity; secondly, in the reference a higher total gas volume flow rate of 120 Nml min<sup>-1</sup> was used, instead of 80 Nml min<sup>-1</sup>, and this allows again to increase the reduction extent reached by the sample; thirdly, in the reference a higher H<sub>2</sub> molar fraction, equal to 5% in Ar, was fed to the reactor, against the value of 0.5% used here, thereby allowing once again to reach much higher reduction extents and thus higher effectiveness in the subsequent oxidation.

$T_{\text{ox}} = 800 \text{ }^\circ\text{C}$	<b>Abanades et al. [50]</b>	<b>Present work (test#2)</b>
<b>Conditions</b>	$y_{\text{CO}_2} = 50\%$ , $\Delta t = 90 \text{ min}$	$y_{\text{CO}_2} = 20\%$ , $\Delta t = 30 \text{ min}$
<b>CO prod. [mmol g<sup>-1</sup>]</b>	4.3	0.92 (on average)

Table 5.6: Comparison of the CO productivities among Abanades et al. [50] and the present work.

$T_{\text{ox}} = 800 \text{ }^\circ\text{C}$	<b>Farooqui et al. [54]</b>	<b>Present work (test#2)</b>
<b>Red. conditions</b>	$\Delta t = 30 \text{ min}$ , $\dot{V}_{\text{tot}} = 120 \text{ Nml min}^{-1}$ , $y_{\text{H}_2} = 5\%$	$\Delta t = 15 \text{ min}$ , $\dot{V}_{\text{tot}} = 80 \text{ Nml min}^{-1}$ , $y_{\text{H}_2} = 0.5\%$
<b>CO prod. [mmol g<sup>-1</sup>]</b>	10	0.92 (on average)

Table 5.7: Comparison of the CO productivities among Farooqui et al. [54] and the present work.

Table 5.8 below summarizes the outcomes in terms of O<sub>2</sub> and CO yields presented so far, for both cerium oxides and iron oxides based cycles. For the iron oxides data, the O<sub>2</sub> results come from the thermal reduction of test#1, whereas the CO results come from the oxidation with CO<sub>2</sub> of test#2, to be coherent with the cerium oxides related data. The values reported have to be interpreted just as indicative values, since error bars were not evaluated in the analysis. Looking in particular at the productivities and at the production rates, it can be observed that the iron oxides results are much better than the cerium oxides ones. As a qualitative comment, this could come, among the rest, from the stoichiometric nature of the iron oxides based cycle, that leads to higher oxygen release and to higher fuel productivity. As a consequence of these considerations, the iron oxides were chosen for performing the numerical modeling part of this work, that will be presented in Section 6.

<i>Average on cycles</i>	<b>Cerium oxides</b>		<b>Iron oxides</b>	
	<b>O<sub>2</sub></b>	<b>CO</b>	<b>O<sub>2</sub> (test#1)</b>	<b>CO (test#2)</b>
<b>Volumes [Sml]</b>	0.149	0.317	0.105	0.541
<b>Avg. vol. flow rates [Sml min<sup>-1</sup>]</b>	0.005	0.021	0.007	0.018
<b>Productivities [Sml g<sup>-1</sup>]</b>	3.155	6.833	5.134	20.699
<b>Prod. rates [Sml min<sup>-1</sup> g<sup>-1</sup>]</b>	0.105	0.456	0.342	0.689

Table 5.8: Summarizing table of the results obtained in terms of O<sub>2</sub> and CO yields with cerium oxides and iron oxides.

**5.2.2.3 Third part. Mixed equivalent cycle** The third part of this analysis consists in considering an equivalent mixed cycle, starting from the ones performed in test#1 and test#2 above, with the aim of comparing directly the results obtained with the ones coming from cerium oxides, not having been possible to run such a complete cycle at the laboratory scale. Thus, the mixed cycle was built as the union of the thermal reduction of test#1, performed at 1350°C for 15

min, and the CO<sub>2</sub> oxidation of test#2, performed at 800°C for 30 min. A structure similar to the cerium oxides thermal program was considered, as reported below in Table 5.9.

Segment	T <sub>start</sub> /duration or slope/T <sub>end</sub>
...	...
#1	800°C/5 min/800°C
#2	800°C/50 K min <sup>-1</sup> /1350°C
#3	1350°C/15 min/1350°C
#4	1350°C/-50 K min <sup>-1</sup> /800°C
#5	800°C/5 min/800°C
#6	800°C/30 min/800°C
...	...

Table 5.9: Thermal program for an equivalent mixed cycle based on test#1 and test#2, with the same structure of the cerium oxides based cycles.

In this way, a thermochemical efficiency can be estimated, using the same formulations reported above in Equations 5.1 and 5.2, and making use of the same simplifying hypotheses. Thus, considering an average amount of CO produced in the test#2 oxidation around  $2.37 \cdot 10^{-5}$  mol, an average initial mass of Fe<sub>2</sub>O<sub>3</sub> of 24.76 mg (average among the actual values, not among the apparent ones), a specific heat capacity for Fe<sub>2</sub>O<sub>3</sub> at the mean temperature of 1075°C around 0.896 J g<sup>-1</sup> K<sup>-1</sup> (NIST data), a temperature difference  $\Delta T$  of 550°C, an Ar volume flow rate  $\dot{n}_{Ar}$  of 80 ml min<sup>-1</sup>, a time needed for the heating up ramp  $\Delta t$  of 11 min, a thermal efficiency  $\epsilon$  around 98%, and keeping constant all the other parameters involved in the formulas, then the thermochemical efficiency results to be around 0.11%, higher than the value obtained in the cerium oxides case.

	Cerium oxides based cycle	Iron oxides based equivalent cycle
$\eta_{thchem,CO}$	0.055%	0.11%

Table 5.10: Thermochemical efficiencies obtained in the present experimental analyses, through the formula and with the hypotheses proposed.

Under the hypotheses done, the value coming from using iron oxides in place of cerium oxides - with this given cycle structure - seems to be roughly double. This is the further and definitive reason why iron oxides were chosen for the numerical modeling step of the work, that will be presented in the following section.

## 6 Numerical modeling

In this section, a numerical model built in COMSOL Multiphysics® environment will be presented and discussed. As mentioned in the previous part, the iron oxides were selected to perform the numerical simulation step of the workflow, because of higher O<sub>2</sub> and CO productivities and production rates and because of a higher value for the estimated thermochemical efficiency of the redox cycle, although the slightly different operating conditions implemented in the two cases. The numerical model simulates the cylindrical solar receiver-reactor of the CSP system installed at the Energy Center research pole, Turin (Italy), and in particular the iron oxide (hematite) transient thermal reduction reaction that takes place with the given boundary conditions imposed. Thus, the outcomes from the test#1 will be considered as a reference here in this part. In the real system, the receiver is placed in the focus of the paraboloidal concentrator to absorb as much solar radiation as possible. The concentrator was not considered inside the numerical simulation, apart from a thermal flux boundary condition imposed on the external walls of the cylinder.

Subsection 6.1 will present a kinetic analysis, based on the experimental results obtained and presented so far, as a link between experiments and numerical model. Subsection 6.2 will describe the geometry implemented and the materials used, while Subsection 6.3 will deal with the physics involved. Finally, Subsection 6.4 will be devoted to the meshing and computational optimization procedures that were performed, whereas in Subsection 6.5 the results obtained will be shown and discussed.

### 6.1 Kinetic analysis and data-fitting

Since the model is a transient one taking into account the reaction kinetics, then a reduction kinetic model assessment is needed. For a gas-solid reaction as the one of interest, the reaction rate can be expressed as a function of temperature  $T$  and of the temporal conversion function  $\alpha(t)$ , as in Equation 6.1 [54]:

$$r(T, t) = \frac{d\alpha}{dt} = k(T)f(\alpha) \quad (6.1)$$

$k(T)$  is the Arrhenius rate constant, expressed as in Equation 6.2:

$$k(T) = k_0 e^{-\left(\frac{E_a}{RT}\right)} \quad (6.2)$$

$R$  is the gas constant (8.314 J mol<sup>-1</sup> K<sup>-1</sup>),  $k_0$  is the pre-exponential factor (s<sup>-1</sup>) and  $E_a$  is the activation energy (kJ mol<sup>-1</sup>).  $f(\alpha)$  is the differential form of the kinetic model function. The corresponding integral form,  $g(\alpha)$ , can be found integrating isothermally the Equation 6.1, leading to Equation 6.3:

$$g(\alpha) = \int_0^\alpha \frac{d\alpha}{f(\alpha)} = k(T) \cdot t \quad (6.3)$$

The experimental data concerning  $\alpha(t)$  are used in Equation 6.3 to determine the best reaction model to be used. The experimental curve coming from the integral expression (second term of Equation 6.3) is compared with the theoretical one (third term of Equation 6.3), this latter being linear in  $t$  at a fixed temperature. Experimental data from the test#1 thermal reduction can be thus fitted through varying the model parameters, i.e.,  $k_0$  and  $E_a$ . Herein, the pre-exponential factor  $k_0$  was fixed at the value proposed by Bush and Loutzenhiser [53] ( $k_0 = 2.768 \pm 0.783 \cdot 10^{14}$  s<sup>-1</sup>), since the experimental conditions are the same there and in test#1 performed in this work, and  $E_a$  was varied for finding the optimum. Table 6.1 reports the results for the only two models showing a coefficient of determination  $R^2$  higher than 0.9, among the ones typically used for gas-solid reactions and tested here, shown for completeness in Table 6.2 [54] with the corresponding

differential and integral forms of the model function ( $X$  stands for  $\alpha$ ). The fit performed with all the 19 models proposed is shown in Figure 6.1, and the most suitable resulted to be the the Jander diffusion one (model #10).

Model	$E_{a,opt}$ [kJ mol <sup>-1</sup> ]	95% confidence interval for $E_{a,opt}$	RMSE	SSE	$R^2$
#10	487.9	$\pm 0.4$	0.05701	0.195	0.9361
#12	460.8	$\pm 0.4$	0.4632	12.45	0.9012

Table 6.1: Results of the two best models among the ones tested.

No	Model	$f(X)$	$g(X)$
<i>Power law models</i>			
1		$4X^{3/4}$	$X^{1/4}$
2		$3X^{2/3}$	$X^{1/3}$
3		$2X^{1/2}$	$X^{1/2}$
4		$(2/3)X^{-1/2}$	$X^{3/2}$
<i>Geometrical contraction models</i>			
5	Zero order	1	$X$
6	2D(also called R2)	$2(1-X)^{1/2}$	$1-(1-X)^{1/2}$
7	3D(also called R3)	$3(1-X)^{2/3}$	$1-(1-X)^{1/3}$
<i>Diffusion models</i>			
8	1D	$1/(2X)$	$X^2$
9	2D	$(-\ln(1-X))^{-1}$	$X+(1-X)\ln(1-X)$
10	diffusion – Jander D3	$3/2(1-X)^{2/3}(1-(1-X)^{1/3})^{-1}$	$(1-(1-X)^{1/3})^2$
11	Ginstling – Brousttein D4	$3/2((1-X)^{-1/3}-1)^{-1}$	$(1-2/3X)-(1-X)^{2/3}$
<i>Reaction – order models</i>			
12	first order	$(1-X)$	$-\ln(1-X)$
13	3/2 order	$(1-X)^{3/2}$	$2((1-X)^{-1/2}-1)$
14	second order	$(1-X)^2$	$(1-X)^{-1}$
15	third order	$(1-X)^3$	$0.5((1-X)^{-2}-1)$
<i>Nucleation models</i>			
16	$n = 1.5$	$2/3(1-X)(-\ln(1-X))^{1/3}$	$(-\ln(1-X))^{2/3}$
17	$n = 2$	$2(1-X)(-\ln(1-X))^{1/2}$	$(-\ln(1-X))^{1/2}$
18	$n = 3$	$3(1-X)(-\ln(1-X))^{2/3}$	$(-\ln(1-X))^{1/3}$
19	$n = 4$	$4(1-X)(-\ln(1-X))^{3/4}$	$(-\ln(1-X))^{1/4}$

Table 6.2: Kinetic models used for gas-solid reactions [54].

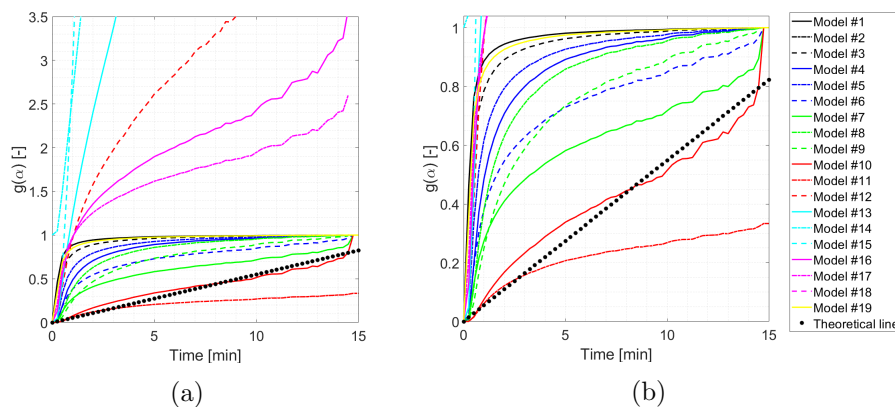


Figure 6.1: Data-fitting of the experimental data from thermal reduction of test#1 through different kinetic models with the theoretical line.

It is worth saying that the value of 487.9 kJ mol<sup>-1</sup> obtained here for the activation energy is very

close to the one retrieved by Bush et al. [53], equal to  $487 \text{ kJ mol}^{-1}$ . The Jander model will be thus implemented in the numerical model for simulating the reduction kinetics. It is noteworthy as well that the value for the activation energy was found out here at a given temperature, equal to the one of the experiments. Since the model simulates a 3D geometry, then a temperature distribution actually will exist in the domain. This implies that the use of such a model is for sure an approximation in the theory perspective, but it is the correct reference benchmark, since both the reaction and the material used are the same as in the TGA.

## 6.2 Geometry and materials

For describing the geometry and the materials used, the real system object of the simulation will be briefly described. The system, produced by El.Ma srl Electronic Machining [52], is composed of an aluminum paraboloid internally coated with a polymeric film with high optical efficiency reflectivity. The plant is equipped with an automatic solar tracking system with two independent axes - azimuth and elevation - aimed at ensuring the automatic orientation of the paraboloid in such a way to receive solar radiation always with the best possible angle of incidence. From the solar dish data sheet [52], the supplier reports that, if a capturing surface of  $4.5 \text{ m}^2$  is considered, as well as an optical efficiency of 80% and an average direct irradiance around  $800 \text{ W/m}^2$ , the concentrated power results to be of roughly 2.8 kW. In the focal point, temperatures higher than  $1800^\circ\text{C}$  can be even reached. As mentioned, the part of the real system that was simulated is the cylindrical solar reactor-receiver. The modeled cylindrical geometry is shown in Figure 6.2. Figure 6.2a shows the whole cylindrical receiver, whereas Figures 6.2b, 6.2c and 6.2d show the sub-domains in which the cylinder was divided, in the order, the external alumina ( $\text{Al}_2\text{O}_3$ ) tube, the free-flow regions and the porous medium region. The fluid inlet is on the left, and the flow proceeds towards right.

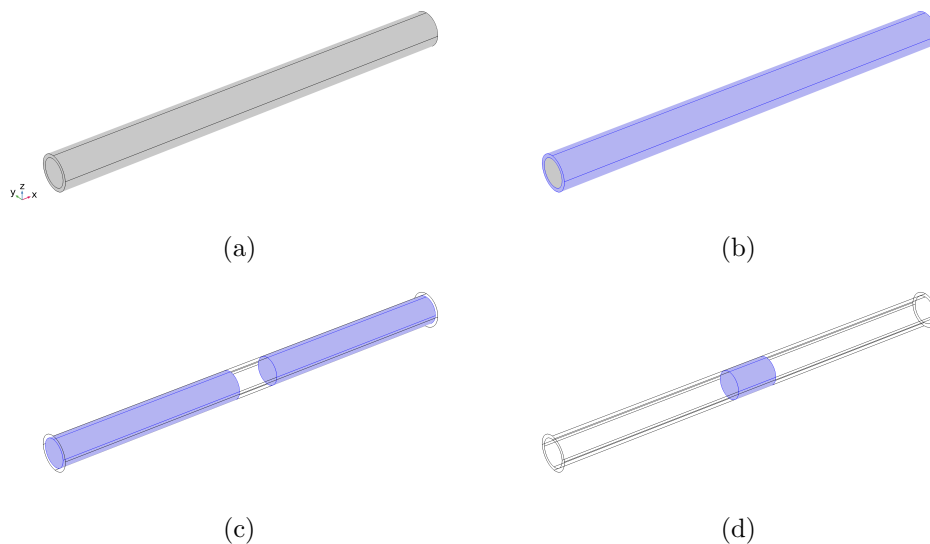


Figure 6.2: Cylindrical geometry implemented in the model: (a) Whole geometry; (b) Alumina tube; (c) Free-flow regions; (d) Porous medium region.

The porous medium in the middle region of the receiver represents the reacting hematite powder. All the geometric data are summarized in Table 6.3. The overall length and the diameters are the ones from the real component, whereas the porous medium length was fixed here so that to have a  $L/D$  ratio of 1.5. The materials properties implemented are instead given in Table 6.4. Where

a range of  $T$  was present for the validity of the given formula, the expression was extrapolated outside it as a constant value. Since the reduction reaction is taking place in the porous medium, the free-flow regions deal with basically pure argon in the half near the inlet, and with an Ar-O<sub>2</sub> mixture in the half near the outlet, where oxygen is being transported downstream by the fluid flow after having been released.

Length [mm]	Ext. diameter [mm]	Int. diameter [mm]	Porous length [mm]
300	25	20	30

Table 6.3: Geometric data used in the model.

<b>Alumina (A<sub>2</sub>O<sub>3</sub>)</b> [55] ( $T$ in K)	
$c_{p,Al_2O_3}$ [J g <sup>-1</sup> K <sup>-1</sup> ]	$1.0446 + 1.742 \cdot 10^{-4} \cdot T - 2.796 \cdot 10^{-4} \cdot T^2$ (to 1500°C)
$\rho_{Al_2O_3}$ [kg m <sup>-3</sup> ]	3800
$k_{Al_2O_3}$ [W m <sup>-1</sup> K <sup>-1</sup> ]	$5.5 + 34.5 \cdot e^{-0.0033 \cdot (T-273)}$ (25-1300°C)
<b>Hematite (Fe<sub>2</sub>O<sub>3</sub>)</b>	
$c_{p,Fe_2O_3}$ [J kg <sup>-1</sup> K <sup>-1</sup> ]	937.5
$\rho_{Fe_2O_3}$ [kg m <sup>-3</sup> ]	5240
$k_{Fe_2O_3}$ [W m <sup>-1</sup> K <sup>-1</sup> ]	0.6
$\phi_{Fe_2O_3}$ [-]	0.48
$K_{Fe_2O_3}$ [m <sup>2</sup> ]	$4 \cdot 10^{-12}$
<b>Ar-O<sub>2</sub> mixture</b>	
$c_{p,mix}$ [J kg <sup>-1</sup> K <sup>-1</sup> ]	Mass fraction averaged
$\rho_{mix}$ [kg m <sup>-3</sup> ]	Molar fraction averaged
$k_{mix}$ [W m <sup>-1</sup> K <sup>-1</sup> ]	Molar fraction averaged
$\gamma_{mix}$ [-]	Ratio of mass fraction averaged values
$\mu_{mix}$ [Pa·s]	$\sim \mu_{Ar}(T)$
<b>Argon</b>	
Properties interpolated from NIST data (functions of $T$ )	
<b>Oxygen</b>	
Properties interpolated from NIST data (functions of $T$ )	

Table 6.4: Properties of the materials used in the model.

## 6.3 Physics

### 6.3.1 Models and governing equations

The model was built as a merging of three sub-models, namely a fluid dynamic one, a thermal one and a chemical one, solving respectively for the velocity and pressure fields, for the temperature field and for the reaction kinetics and concentration fields. As concerns the fluid dynamic part, the Brinkman equations were solved for the Darcy velocity and pressure fields inside and outside the porous medium. The flow was considered as incompressible, as the Mach number was abundantly below 0.3, and laminar, since the Reynolds number was far away from the turbulence transition threshold. Gravity was neglected. With these hypotheses, the continuity and momentum equations

solved take the following form [56]:

$$\nabla \cdot (\rho \mathbf{u}) = Q_{\text{br}} \quad (6.4)$$

$$\frac{\rho}{\phi} \frac{\partial \mathbf{u}}{\partial t} = -\nabla p + \nabla \cdot \left[ \frac{1}{\phi} \left\{ \mu(\nabla \mathbf{u} + (\nabla \mathbf{u})^T) - \frac{2}{3} \mu(\nabla \cdot \mathbf{u}) \mathbf{I} \right\} \right] - \left( K^{-1} \mu + \frac{Q_{\text{br}}}{\phi^2} \right) \mathbf{u} + \mathbf{F} \quad (6.5)$$

$Q_{\text{br}}$  represents mass sources or sinks, whereas  $\mathbf{F}$  accounts for eventual other body forces, such as further viscous contributions [56]. As regards the thermal part, the energy equation (Equation 6.6) was solved across the whole domain, with a volume-averaged thermal conductivity  $k_{\text{eff}}$  in the porous medium region, as shown in Equation 6.9 [57]:

$$(\rho c_p)_{\text{eff}} \frac{\partial T}{\partial t} + \rho c_p \mathbf{u} \cdot \nabla T + \nabla \cdot \mathbf{q} = Q \quad (6.6)$$

$$\mathbf{q} = -k_{\text{eff}} \nabla T \quad (6.7)$$

$$(\rho c_p)_{\text{eff}} = (1 - \phi) \rho_p c_{p,p} + \phi \rho_f c_{p,f} \quad (6.8)$$

$$k_{\text{eff}} = (1 - \phi) k_p + \phi k_f \quad (6.9)$$

$(\rho c_p)_{\text{eff}}$  is the effective volumetric heat capacity at constant pressure,  $\mathbf{u}$  is the Darcy velocity field computed through the Brinkman equations,  $Q$  is the eventual heat source or sink,  $\mathbf{q}$  is the thermal flux and  $\phi$  is the porosity of the powder. The only heat sink will be the endothermicity due to the reduction reaction, as will be explained in a while. As concerns the third, chemical part, the transport equation for each chemical species is solved - i.e., for argon and oxygen -, according to the following set of equations [56]:

$$\rho \frac{\partial \omega_i}{\partial t} + \nabla \cdot \mathbf{j}_i + \rho(\mathbf{u} \cdot \nabla) \omega_i = R_i \quad (6.10)$$

$$\mathbf{j}_i = -\rho D_i \nabla \omega_i - \rho \omega_i D_i \frac{\nabla M_n}{M_n} + \rho \omega_i \sum_k \frac{M_i}{M_n} D_k \nabla y_k \quad (6.11)$$

$$M_n = \left( \sum_i \frac{\omega_i}{M_i} \right)^{-1} \quad (6.12)$$

$\omega_i$  is the mass fraction,  $y_i$  is the mole fraction,  $M_i$  is the molar mass of the  $i$  species involved,  $M_n$  is defined as in Equation 6.12,  $\mathbf{j}_i$  is the mass flux of the  $i$  species ( $\text{kg m}^{-2} \text{s}^{-1}$ ), defined as in Equation 6.11,  $D_i$  is the diffusion coefficient for the  $i$  species and  $R_i$  is the source or sink term for the  $i$  species. The diffusion coefficient, being actually a mutual diffusion one inside the binary mixture considered, was set at the same value for argon and oxygen, and was evaluated through Equation 6.13 [58]:

$$D_{\text{ArO}_2} = \frac{3}{16} \frac{(4\pi kT/M_{\text{ArO}_2})^{1/2}}{n\pi\sigma_{\text{ArO}_2}^2 \Omega_D} f_D \quad (6.13)$$

$$M_{\text{ArO}_2} = 2 \left[ (1/M_{\text{Ar}}) + (1/M_{\text{O}_2}) \right]^{-1} \quad (6.14)$$

$k$  is the Boltzmann constant ( $1.38064852 \cdot 10^{-23} \text{ m}^2 \text{ kg s}^{-2} \text{ K}^{-1}$ ),  $M_i$  is the molar mass of the  $i$  species,  $n$  is the number density of molecules in the mixture,  $\sigma_{\text{ArO}_2}$  is a characteristic length ( $\text{\AA}$ ) and  $\Omega_{\text{D}}$  is called the diffusion collision integral (dimensionless).  $f_{\text{D}}$  is a correction term, and was set to unity. In the hypothesis of ideal gas behaviour, the expression becomes the following:

$$D_{\text{ArO}_2} = \frac{0.00266T^{3/2}}{pM_{\text{ArO}_2}^{1/2}\sigma_{\text{ArO}_2}^2\Omega_{\text{D}}} \quad (6.15)$$

The pressure  $p$  is expressed in bar,  $T$  is the absolute temperature and  $D_{\text{ArO}_2}$  is expressed in  $\text{cm}^2 \text{ s}^{-1}$ . The function  $\Omega_{\text{D}}$  takes the following form [58]:

$$\Omega_{\text{D}} = \frac{A}{(T^*)^B} + \frac{C}{e^{DT^*}} + \frac{E}{e^{FT^*}} + \frac{G}{EHT^*} \quad (6.16)$$

$$T^* = \frac{kT}{\epsilon_{\text{ArO}_2}} \quad (6.17)$$

$$A = 1.06036, B = 0.15610, C = 0.19300, D = 0.47635, \\ E = 1.03587, F = 1.52996, G = 1.76474, H = 3.89411$$

The characteristic energy  $\epsilon$  and the characteristic length  $\sigma$  are defined as follows, with the corresponding values assumed for argon and oxygen [58]:

$$\epsilon_{\text{ArO}_2} = (\epsilon_{\text{Ar}}\epsilon_{\text{O}_2})^{1/2} \quad (6.18)$$

$$\sigma_{\text{ArO}_2} = \frac{\sigma_{\text{Ar}} + \sigma_{\text{O}_2}}{2} \quad (6.19)$$

$$\sigma_{\text{Ar}} = 3.542 \text{ \AA}, \frac{\epsilon_{\text{Ar}}}{k} = 93.3 \text{ K},$$

$$\sigma_{\text{O}_2} = 3.467 \text{ \AA}, \frac{\epsilon_{\text{O}_2}}{k} = 106.7 \text{ K}$$

In order to quicken the simulation running, a temperature-averaged mutual diffusion coefficient was evaluated and implemented. Considering a pressure roughly constant and of the order of 1 bar, and a  $T$  range going from 293.15 K to 1800 K, a value around  $1.83 \text{ cm}^2 \text{ s}^{-1}$  was estimated and used. Since the model is transient, a further interface was needed in order to solve for the time dependency. Reminding Equation 5.3 for the temporal conversion function, it can be rearranged in the following way:

$$\alpha(t) = \frac{m_0 - m(t)}{m_0 - m_\infty} \equiv \frac{\tilde{m}(t)}{m_0 - m_\infty} \quad (6.20)$$

With this sign inversion,  $\tilde{m}(t)$  becomes the mass of oxygen released from  $t = 0$  up to time  $t$ . If the cross section at the outlet of the porous medium region is considered, the total oxygen mass flux - advective and diffusive - along the flow direction can be integrated on the surface and in time, to give exactly the integral quantity of interest:

$$\tilde{m}(t) = \int_0^t \left\{ \iint_{A_{\text{out,por}}} j_{\text{x,O}_2,\text{tot}}(t) \text{ d}A \right\} \text{d}t \quad (6.21)$$

In the model,  $\tilde{m}(t)$  is used inside the function  $\alpha(t)$ , on its own used in the differential kinetic function  $f(\alpha)$  by the Jander diffusion model to compute the reaction rate, expressed in terms of  $\text{kg}_{\text{O}_2} \text{ m}^{-3} \text{ s}^{-1}$ . The following ODE in time is solved by the model to find out the quantity  $\tilde{m}(t)$ :

$$\frac{\text{d}\tilde{m}(t)}{\text{d}t} = \iint_{A_{\text{out,por}}} j_{\text{x,O}_2,\text{tot}}(t) \text{ d}A \quad (6.22)$$

The initial value for  $\tilde{m}(t)$  was set to zero (or better, to a negligibly small value in order to avoid numerical issues), whereas its initial first derivative was assessed from the reduction experimental data. Differentiating Equation 6.20, the following value can be estimated:

$$\left. \frac{d\tilde{m}(t)}{dt} \right|_{t=0} = (m_0 - m_\infty) \left. \frac{d\alpha}{dt} \right|_{t=0} \approx 0.47 \frac{g}{s} \quad (6.23)$$

The values for  $m_0$  and  $m_\infty$  were estimated as follows. Considering the volume of the porous region, the volume occupied by the hematite powder was calculated through the porosity, and then its initial mass was evaluated using the hematite density:

$$V_{\text{porous}} = \pi \frac{D_{\text{int}}^2}{4} L \simeq 9425 \text{ mm}^3 \quad (6.24)$$

$$V_{\text{Fe}_2\text{O}_3} = (1 - \phi) V_{\text{porous}} \simeq 4901 \text{ mm}^3 \quad (6.25)$$

$$m_0 = \rho_{\text{Fe}_2\text{O}_3} V_{\text{Fe}_2\text{O}_3} \simeq 25.68 \text{ g} \quad (6.26)$$

Then, supposing to reach a complete reduction of the hematite towards wüstite, from the stoichiometry of Reaction 6.27 the maximum stoichiometric mass of oxygen releasable was estimated. This quantity corresponds exactly to the difference  $m_0 - m_\infty$ :



$$m_{\text{O}_2, \text{max, stoich}} = m_0 - m_\infty \simeq 2.57 \text{ g} \quad (6.28)$$

Boundary and initial conditions imposed in the simulation are described in the following subsection.

### 6.3.2 Boundary and initial conditions

As initial condition for the transient simulation, a uniform temperature of 293.15 K (assumed as the ambient temperature) was imposed in the whole domain, thereby supposing that at the initial time the argon flow rate is fed to the system simultaneously with the exposition of the receiver to the concentrated solar radiation. This assumption should be coherent with the way of proceeding in the future experiments on field, since it would not be desirable to heat up first the powder and then to send a purge gas later, when the material could be already in a certain reduced state. Thus, the transient covers the whole heating up of the system, that takes place simultaneously with the reduction reaction inside the porous medium. The initial conditions in terms of the ODE in time were already pointed out in the previous subsection. As concerns the boundary conditions in space, an argon inlet velocity of  $10 \text{ cm s}^{-1}$  and an outlet pressure of 1 bar (ambient pressure) were imposed, as well as a zero velocity field inside the system at the initial time. As regards the thermal part, several items need to be mentioned: first of all, a zero flux was imposed at the inlet and outlet alumina tube sections and at the outlet fluid section, whereas the argon inlet temperature was fixed at 293.15 K (ambient temperature). Then, natural convection was supposed to subsist on the whole external surface of the cylinder. The correlation for natural convection around a cylinder proposed by Churchill and Chu [59] for the Nusselt number was implemented:

$$h = \frac{k}{D_{\text{ext}}} Nu_{\text{D}} = \frac{k}{D_{\text{ext}}} \left( 0.6 + \frac{0.387 Ra_{\text{D}}^{1/6}}{\left( 1 + \left( \frac{0.559}{Pr} \right)^{9/16} \right)^{8/27}} \right)^2, \quad 10^{-5} \leq Ra_{\text{D}} \leq 10^{12}, \quad \forall Pr \quad (6.29)$$

$$Ra_{\text{D}} = \frac{g\beta\Delta TD^3}{\alpha\nu}, \quad Pr = \frac{\nu}{\alpha} \quad (6.30)$$

$h$  is the natural convection coefficient,  $k$  is the air thermal conductivity,  $Ra$  is the Rayleigh number, defined as in Equation 6.30,  $g$  is the gravitational acceleration,  $\beta$  is the volumetric thermal expansion coefficient for the air,  $\alpha$  and  $\nu$  are the thermal and momentum diffusivities for the air, and  $Pr$  is the Prandtl number for the air. Also a Neumann boundary condition was imposed on the half external surface of the cylinder exposed to the solar concentrator. Here, a gaussian thermal flux distribution was imposed to simulate the radiation concentration near the focus. The thermal flux was imposed by a trial and error procedure in order to obtain a maximum temperature near the focus in the range 1500-1600°C in absence of any reaction (steady, purely thermo-fluid dynamic problem), being this value coherent with the CSP technology used in the reality, that as mentioned before could guarantee a maximum temperature at the focal point of the order of 1800°C in the optimal operating conditions [52]. This assumption could be for sure optimized in the future imposing a temperature distribution matching experimental measures on field. As concerns the third, chemical part, a zero  $O_2$  molar fraction was imposed at the inlet, as well as in the whole domain at the initial time. The *boundary* condition of relevance is the  $O_2$  source inside the porous medium due to the reduction reaction. Coherently with the Jander kinetic model that was selected, the  $O_2$  source - expressed in terms of  $kg_{O_2} m^{-3} s^{-1}$  - was implemented as follows:

$$S_{O_2} = \frac{(m_0 - m_\infty)}{V_{porous}} k(T) f(\alpha) = \frac{3}{2} \frac{(m_0 - m_\infty)}{V_{porous}} k_0 e^{-\frac{E_a}{RT}} \frac{(1 - \alpha)^{2/3}}{1 - (1 - \alpha)^{1/3}} \quad (6.31)$$

Hence, a heat sink due to the endothermicity of the reduction reaction was implemented as further thermochemical boundary condition, considering an enthalpy of reduction around  $478.7 \text{ kJ mol}_{O_2}^{-1}$ :

$$\dot{Q}_{sink} = \frac{\Delta h_{red} \cdot S_{O_2}}{M_{O_2}} \quad (6.32)$$

$\dot{Q}_{sink}$  is here expressed in  $\text{kW m}^{-3}$ , being  $M_{O_2}$  expressed in  $\text{kg mol}^{-1}$ .

## 6.4 Mesh and computational optimization procedures

In order to optimize the computation, a preliminary grid independence study was conducted to find out the optimal mesh size. The space convergence results, shown in Figure 6.3, refer to the time  $t = 1000 \text{ s}$ , where it was ascertained that the time derivatives were large enough and far from the final equilibrium. Figure 6.3a reports the relative error in terms of temperature in the most exposed point of the domain, whereas Figure 6.3b shows the relative error for the quantity  $\frac{d\hat{m}}{dt}$ . The error, assessed taking as reference a sufficiently finer mesh resolution, decreases in both cases in a monotonous fashion. The finest mesh shown in Figure 6.3 was thus selected, since for higher refining the computational times and costs became too large. The final mesh implemented is shown in Figure 6.4. A uniform pattern along the receiver was chosen. Figure 6.4a reports the whole meshing, whereas Figure 6.4b gives a detail of the inlet cross section. In this latter case, prismatic cells can be observed near the inner walls in order to solve for the boundary layer. The time convergence analysis was not performed, since the simulation was run automatically with an adaptive time-stepping scheme.

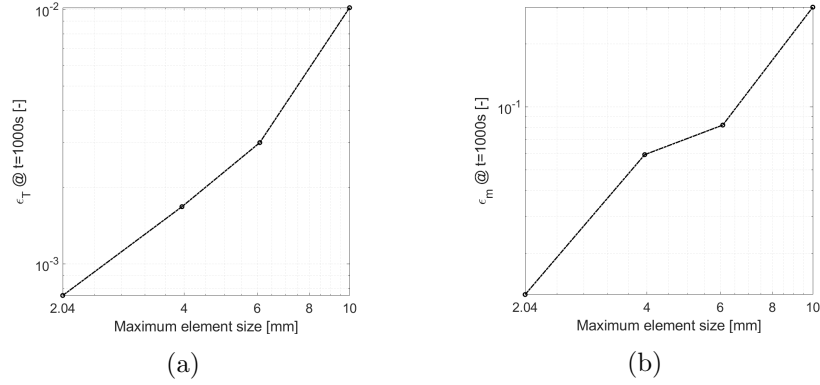


Figure 6.3: Space convergence results after 1000 s in terms of relative errors, respectively (a) for the temperature in the most exposed point and (b) for the oxygen mass flux across the outlet section of the porous medium.

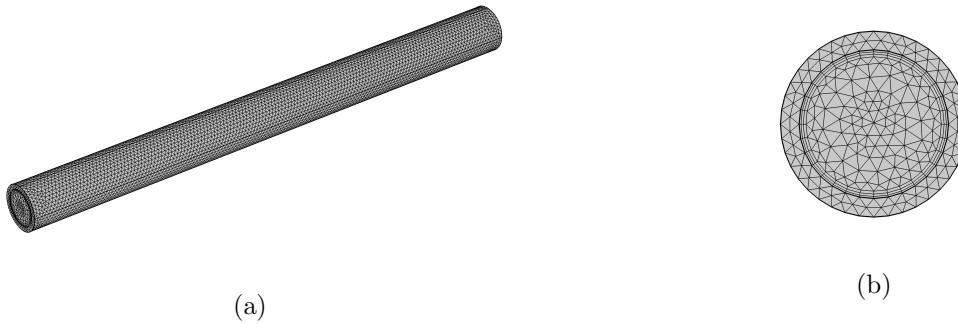


Figure 6.4: Mesh selected for the final simulation: (a) Uniform mesh in the whole domain; (b) Detail of the inlet cross section.

## 6.5 Results and discussion

The transient simulation was run until the conversion function  $\alpha(t)$  reached the unity value, meaning that the reduction was completed (i.e., the maximum amount of available oxygen was released), and this time interval resulted to be around 105 min. Figure 6.5 shows a detail of the velocity field in the porous medium region (left) and the overall pressure field (right) at the final time  $t_{\text{final}}$ . The velocity becomes basically uniform due to the presence of the porous powder, and returns to have a kind of usual profile in the free flow region. A no-slip condition is set on the inner walls. The pressure drop, of the order of 0.3 bar, is as well concentrated in the porous medium.

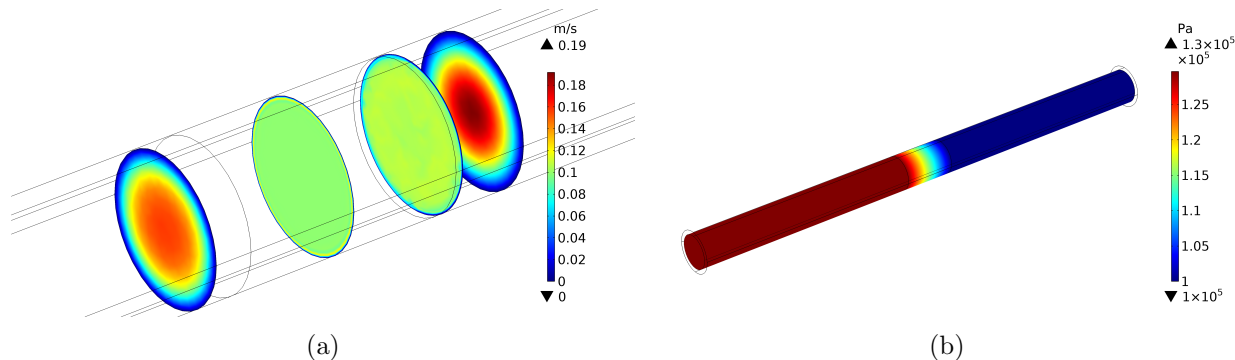


Figure 6.5: (a) Detail of the velocity field in the porous region; (b) Pressure field on the outer surface (the pressure is basically uniform on a given cross section, since gravity effects were neglected).

The temperature field on the outer surface at  $t_{\text{final}}$  is shown in Figure 6.6a. The Gaussian-type distribution can be observed, as a consequence of the Gaussian thermal flux imposed: the highest values of external temperature are reached near the focal point, and then it decreases going towards the edges of the system. The  $T$  profile on the most exposed edge of the receiver is shown in Figure 6.6c. In this latter, it appears clear how the cylinder reaches higher temperatures near the outlet than near the inlet: having the fluid absorbed some thermal power along the path, the heat exchange can proceed up to a lower extent. The highest value reached is around 1770 K (around 1500°C), and it is expected to grow in principle until the steady, purely thermo-fluid dynamic value is reached. The temperature evolution in time in the most exposed point of the receiver is shown in Figure 6.6d: it is clear how it grows very fast at the beginning because of the exposition to the concentrated radiation; then, its first derivative in time decreases suddenly due to the endothermicity of the reduction reaction, before reaching the next region in which it starts to grow again due to the decreasing in the  $\text{O}_2$  releasing, presumably until the steady state value of thermal equilibrium, as said. A representation of the temperature field in the fluid domain is finally given in Figure 6.6b, where the  $T$  distribution on the central cross section is reported at the time  $t_{\text{final}}$ .

Figure 6.7 reports the  $\text{O}_2$  molar fraction field across the whole fluid domain, that is the main output of the model. After 60 s, the oxygen releasing is concentrated in correspondence of the highest temperatures region, as expected from reaction kinetics. The *hot spot* spreads out for larger and larger times, as is shown in Figure 6.7b. Figure 6.7c shows a detail of the molar fraction field at  $t_{\text{final}}$  in form of slices of the fluid domain. The  $\text{O}_2$  concentration becomes uniform downstream to the porous medium. Figure 6.7d reports the evolution in time of the surface-averaged  $\text{O}_2$  molar fraction on the outlet section. The value reached at  $t_{\text{final}}$  is around 0.5%, with a peak in the middle around 2.9%.

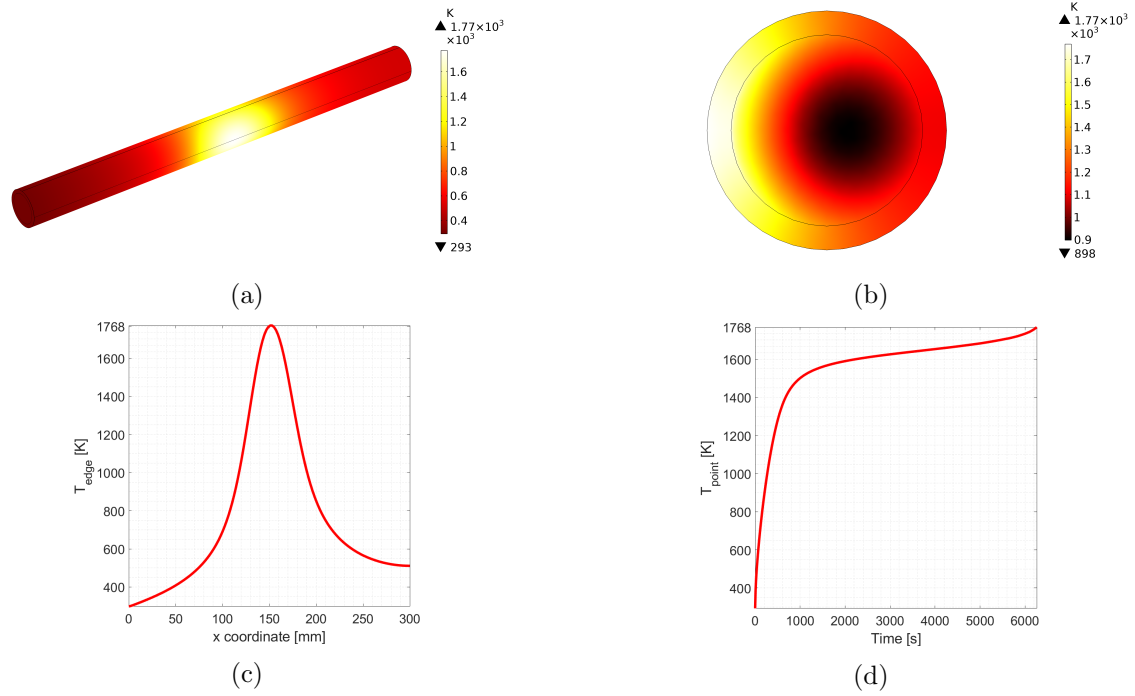


Figure 6.6: (a) Temperature distribution on the outer surface at  $t_{\text{final}}$ ; (b) Temperature distribution on the central cross section at  $t_{\text{final}}$ ; (c) Temperature profile on the most exposed edge of the receiver at  $t_{\text{final}}$ ; (d) Temperature evolution in time in the most exposed point of the receiver.

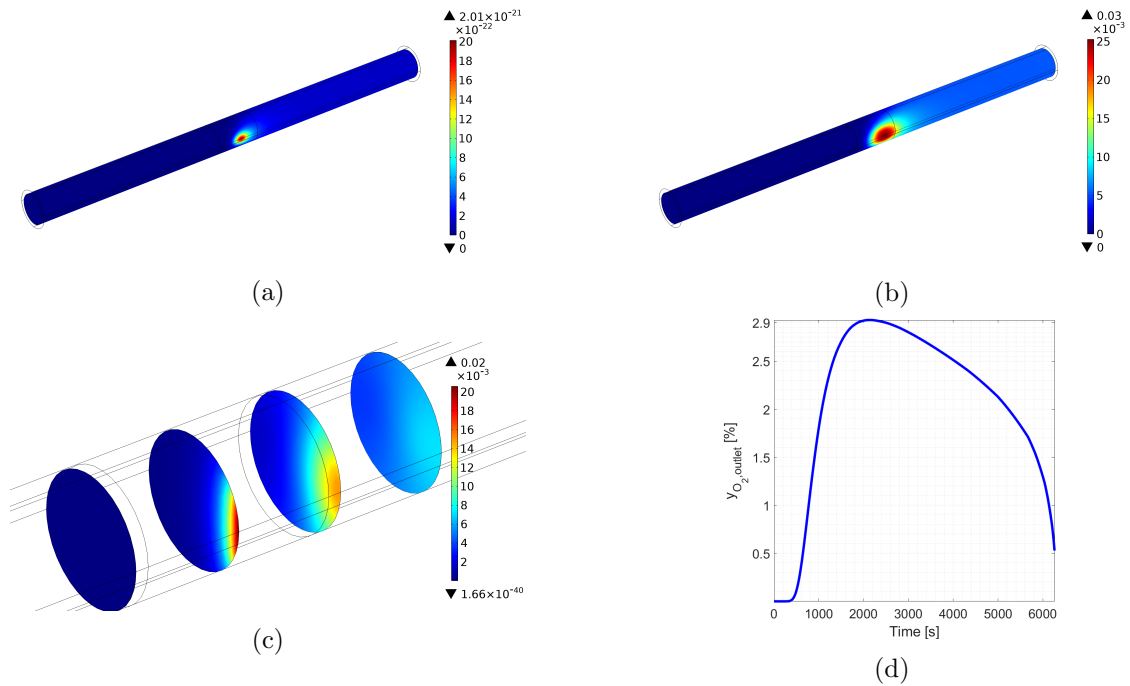


Figure 6.7:  $\text{O}_2$  molar fraction field: (a)  $t = 60$  s; (b)  $t = t_{\text{final}}$ ; (c) Detail of (b); (d) Time evolution of the surface-averaged  $\text{O}_2$  molar fraction on the outlet section.

Kinetic results are finally shown in Figure 6.8. In particular, Figure 6.8a reports the evolution in time of the temporal conversion function  $\alpha(t)$  and  $\tilde{m}(t)$ , that are completely superimposed, being their ratio constant by definition. As imposed, the transient ended when  $\alpha(t)$  reached the unity value, corresponding to a value for  $\tilde{m}(t)$  exactly equal to the maximum amount of oxygen releasable. On the other hand, Figure 6.8b reports the behaviour of the modeled reaction rate and of  $\frac{d\tilde{m}}{dt}$ , again superimposed by definition. The highest rate reached was around  $2.3 \cdot 10^{-4} \text{ s}^{-1}$  after roughly 2000 s. The reaction rate shape is exactly the same as the one shown in Figure 6.7d, as expected. The values obtained here for  $r(t)$  are much lower than the experimental ones obtained through the TGA in test#1. However, they cannot be actually compared in a significant way, firstly because of the different experimental and numerical nature, and secondly because the operating conditions are completely different from each other, e.g. because of the different masses involved and mainly of the inhomogeneous temperatures instead of a controlled and uniform thermal level. In other words, whereas the TGA can be considered as a sort of 0D analysis, the model takes into account a real 3D geometry. In order to have a consistent feedback for evaluating these numerical outcomes, a validation of the model should be properly performed on field through direct experiments with the real CSP system. The validation could be e.g. pursued comparing the real and numerical profiles in time of the  $\text{O}_2$  molar fraction on the outlet cross section (Figure 6.7d).

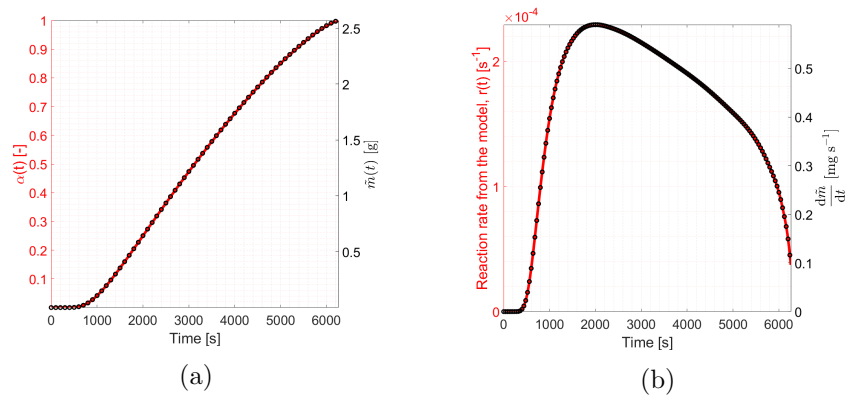


Figure 6.8: Kinetic results from the model: (a) Temporal conversion function  $\alpha(t)$  and  $\tilde{m}(t)$ ; (b) Reaction rate  $r(t)$  and  $\frac{d\tilde{m}}{dt}$ .

## 7 Conclusions

### 7.1 Summarizing

In this analysis, a fairly comprehensive workflow was followed as concerns the thermochemical cycles using cerium oxides and iron oxides. After the literature review, indispensable to have an as much as possible complete idea of the processes analysed, a first experimental step was taken in order to compare the experimental behaviour and performances of cerium oxides and iron oxides samples, in the given operating conditions, among themselves and versus the reference literature. The main items were assessed for both the materials, such as the volumes, the average volume flow rates and mainly the productivities and the production rates in terms of O<sub>2</sub> released in the reduction phase and of CO produced in the oxidation phase. As concerns the cerium oxides, three different samples were compared through a thermogravimetric analysis, and the outcomes seem to be fairly in agree with the literature ones: an average nonstoichiometry  $\Delta\delta$  around 0.049 was estimated, against e.g. the value obtained by Furler et al. [48] around 0.037-0.038, again through a TGA approach. Being these values very close to each other, it seems reasonable to conclude that the present results are reliable. Moreover, an average CO production rate around 0.46 Sml min<sup>-1</sup> g<sup>-1</sup> was achieved, once again in the range proposed by Furler et al. [48]. The average CO productivity amounted to 6.83 Sml g<sup>-1</sup>. As regards the iron oxides samples, the analysis was splitted in three sub-steps: a first one, performing isothermal cycles composed of thermal reduction and air-based oxidation; a second one, performing again isothermal cycles, composed of H<sub>2</sub>-aided reduction and CO<sub>2</sub>-based oxidation; finally a third one, in which an equivalent cycle was built making use of the available data from the previous two tests. In terms of CO yield, a production rate around 0.69 Sml min<sup>-1</sup> g<sup>-1</sup> and a productivity around 20.7 Sml g<sup>-1</sup> were estimated. These better results for the iron oxides case, together with a higher amount of O<sub>2</sub> released and - last but not least - a higher thermochemical efficiency (with the definition adopted herein and the hypotheses done) led to choose the iron oxides for the following numerical step of the workflow. The numerical simulation allowed to visualize and to predict - at least up to a qualitative level - how the cylindrical receiver-reactor object of the study could behave in a real experimental run. The experimental and modeling parts were connected together through a data-fitting procedure making use of the TGA data available, in order to determine a first-approximation model to be used for simulating the real 3D geometry and the multiple physics involved.

### 7.2 Possible further development of the work

The work presented herein could be extended and deepened in several directions. Under the experimental point of view, it could be interesting to perform in a TGA framework the real mixed equivalent cycle with iron oxides presented in Subsection 5.2.2.3, allowing for a more consistent comparison with the results obtained with cerium oxides. It would be interesting as well to conduct a kinetic model assessment both for the cerium oxides results and for the low temperature oxidation step, for both the materials used, and to compare the outcomes with the ones from the available literature. The whole experimental analysis could be moreover extended and reinforced through a full characterization of the materials used (cerium oxides and iron oxides powders), and this could allow also for a more aware material setting in the following numerical simulation. Furthermore, also a parametric study for assessing the effect of the factors of interest such as the operating temperature, the relative molar fractions of the feeding gases and the particle size and structure could allow for a completion of the experimental background, as already done also in the previous literature. Under the numerical modeling point of view, the most natural step should be the validation of the model through direct experimental runs on field making use of the corresponding

real CSP system. Besides this, real measurements and experiments would cancel out the inherent arbitrariness as concerns the operating conditions supposed herein, for instance related to the thermal flux distribution or to the argon volume flow rate imposed. As a further step, the numerical modeling procedure could be extended also to the oxidation phase of the cycle, thereby allowing for a forecast also in terms of fuel productivity.

## References

- [1] *IPCC, 2018: Summary for Policymakers*. In: Global warming of 1.5°C. An IPCC Special Report on the impacts of global warming of 1.5°C above pre-industrial levels and related global greenhouse gas emission pathways, in the context of strengthening the global response to the threat of climate change, sustainable development, and efforts to eradicate poverty V. Masson-Delmotte, P. Zhai, H. O. Portner, D. Roberts, J. Skea, P. R. Shukla, A. Pirani, W. Moufouma-Okia, C. Péan, R. Pidcock, S. Connors, J. B. R. Matthews, Y. Chen, X. Zhou, M. I. Gomis, E. Lonnoy, T. Maycock, M. Tignor, T. Waterfield (eds.). World Meteorological Organization, Geneva, Switzerland, 32 pp.
- [2] Notes from the course "Polygeneration and advanced energy systems" held by prof. M. Santarelli, Politecnico di Torino. Images from slides by prof. A. Lanzini, Politecnico di Torino, a.y. 2019/2020.
- [3] *Advances in carbon capture, utilization and storage*, Zhang et al., Applied Energy 278, 2020.
- [4] *An overview of the solar thermochemical processes for hydrogen and syngas production: Reactors, and facilities*, H.I. Villafán-Vidales, C.A. Arancibia-Bulnes, D. Riveros-Rosas, H. Romero-Paredes, Renewable and Sustainable Energy Reviews 75, 2016.
- [5] *Possible methods for hydrogen production*, M. Balat, Energy Sources, Part A: Recovery, Utilization, and Environmental Effects, 31:39-50, 2008.
- [6] *A review on solar thermal syngas production via redox pair-based water/carbon dioxide splitting thermochemical cycles*, Christos Agrafiotis, Martin Roeb, Christian Sattler, Renewable and Sustainable Energy Reviews 42, 254-285, 2015.
- [7] *Solar coal gasification*, D.W. Gregg, W.R. Aiman, H.H. Otsuki, C.B. Thorsness, Solar Energy 24, 313-321, 1980.
- [8] *Economic analysis of hydrogen production from steam reforming process: A literature review*, Li Kaiwen, Yu Bin and Zhang Tao, Energy Sources, Part B: Economics, Planning, and Policy, 2017.
- [9] *Current status of hydrogen energy*, M. Momirlan and T.N. Veziroglu, Renewable and Sustainable Energy Reviews 6, 141-179, 2002.
- [10] *Dark fermentative biohydrogen production from lignocellulosic biomass: Technological challenges and future prospects*, Juliana Ferreira Soares, Tássia Carla Confortin, Izelmar Todero, Flávio Dias Mayer, Marcio Antonio Mazutti, Renewable and Sustainable Energy Reviews 117, 2020.
- [11] *Flexible Carbon Capture and Utilization technologies in future energy systems and the utilization pathways of captured CO<sub>2</sub>*, H. Mikulčić et al., Renewable and Sustainable Energy Reviews 114, 2019.
- [12] *Carbon-negative emissions: Systemic impacts of biomass conversion. A case study on CO<sub>2</sub> capture and storage options*, Jens Hetland, Ping Yowargana, Sylvain Leduc, Florian Kraxner, International Journal of Greenhouse Gas Control 49, 2016.
- [13] *Screening and techno-economic assessment of biomass based power generation with CCS technologies to meet 2050 CO<sub>2</sub> targets*, A. Bhave et al., Applied Energy 190, 481-489, 2017.

- [14] *CO<sub>2</sub> utilization: Developments in conversion processes*, E. Alper, O. Yuksel Orhan, Petroleum, 2017.
- [15] *CO<sub>2</sub> utilization: Turning greenhouse gas into fuels and valuable products*, M.N. Anwar et al., Journal of Environmental Management 260, 2020.
- [16] *Carbon capture and storage*, Jon Gibbins, Hannah Chalmers, Energy Policy 36, 4317-4322, 2008.
- [17] *Concentrating solar power technology - Principles, developments and applications*, Keith Lovegrove and Wes Stein, 2012.
- [18] *Solar Thermal Electricity Global Outlook 2016*, Full Report.
- [19] IRENA (2020), *Renewable Power Generation Costs in 2019*, International Renewable Energy Agency, Abu Dhabi.
- [20] *REN21 - Renewables 2019 Global Status Report*, Chapter 3, Concentrating Solar Thermal Power, CSP markets.
- [21] Notes from the course "*Technology for renewable energy sources*" held by prof. M. Simonetti, Politecnico di Torino, and prof. John Pye, Australian National University, a.y. 2018/2019.
- [22] *Solar thermal reforming of methane feedstocks for hydrogen and syngas production - A review*, Christos Agrafiotis, Henrik von Storch, Martin Roeb, Christian Sattler, Renewable and Sustainable Energy Reviews 29, 656-682, 2014.
- [23] *Advanced CSP Teaching Materials*, Chapter 2, *Solar Radiation*, Matthias Günther.
- [24] *Advanced CSP Teaching Materials*, Chapter 5, *Parabolic Trough Technology*, Matthias Günther, Michael Joemann, Simon Csambor.
- [25] *Advanced CSP Teaching Materials*, Chapter 6, *Linear Fresnel Technology*, Matthias Günther.
- [26] *High concentration solar collectors*, B. Hoffschmidt, S. Alexopoulos, J. Götsche, M. Sauerborn, O. Kaufhold, Aachen University of Applied Sciences, Jülich, Germany, 2012.
- [27] *Design analysis factors and specifications of solar dish technologies for different systems and applications*, A.Z. Hafez, Ahmed Soliman, K.A. El-Metwally, I.M. Ismail, Renewable and Sustainable Energy Reviews 67, 1019-1036, 2017.
- [28] *Dish systems for CSP*, Joe Coventry, Charles Andracka, Solar Energy 152, 140-170, 2017.
- [29] *Advanced CSP Teaching Materials*, Chapter 7, *Solar Dish Technology*, Matthias Günther, Reza Shahbazfar.
- [30] *A review of solar thermochemical processes*, Deepak Yadav, Rangan Banerjee, Renewable and Sustainable Energy Reviews 54, 497-532, 2016.
- [31] *Likely near-term solar-thermal water splitting technologies*, Christopher Perkins, Alan W. Weimer, International journal of Hydrogen Energy 29, 1587-1599, 2004.
- [32] *Advances and trends in redox materials for solar thermochemical fuel production*, Richard J. Carrillo, Jonathan R. Scheffe, Solar Energy 156, 3-20, 2017.

- [33] *A thermochemical study of ceria: exploiting an old material for new modes of energy conversion and CO<sub>2</sub> mitigation*, William C. Chueh and Sossina M. Haile, Philosophical Transactions Of The Royal Society 368, 3269-3294, 2010.
- [34] *Oxygen exchange materials for solar thermochemical splitting of H<sub>2</sub>O and CO<sub>2</sub>: a review*, Jonathan R. Scheffe and Aldo Steinfeld, Materials Today, 00, 2014.
- [35] *High-Flux Solar-Driven Thermochemical Dissociation of CO<sub>2</sub> and H<sub>2</sub>O Using Nonstoichiometric Ceria*, William C. Chueh, Christoph Falter, Mandy Abbott, Danien Scipio, Philipp Furler, Sossina M. Haile, Aldo Steinfeld, Science 330, 2010.
- [36] *Thermodynamic assessment of non-catalytic Ceria for syngas production by methane reduction and CO<sub>2</sub>+H<sub>2</sub>O oxidation*, A. Bose et al., Materials for Renewable and Sustainable Energy, 2019.
- [37] *Thermochemical hydrogen production from a two-step solar-driven water-splitting cycle based on cerium oxides*, Stéphane Abanades, Gilles Flamant, Solar Energy 80, 1611-1623, 2006.
- [38] *Thermal Reduction of Ceria within an Aerosol Reactor for H<sub>2</sub>O and CO<sub>2</sub> splitting*, J.R. Scheffe, M. Welte, A. Steinfeld, Industrial & Engineering Chemistry Research (I&EC) 53, 2175-2182, 2014.
- [39] *Experimental Demonstration of the Thermochemical Reduction of Ceria in a Solar Aerosol Reactor*, Michael Welte, Rafik Barhoumi, Adrian Zbinden, Jonathan R. Scheffe, Aldo Steinfeld, Industrial & Engineering Chemistry Research (I&EC) 55, 10618-10625, 2016.
- [40] *A thermodynamic study of nonstoichiometric cerium dioxide*, R. J. Panlener, R. N. Blumenthal, J. E. Garnier, The Journal of Physical Chemistry Solids 36, 1213-1222, 1975.
- [41] *CO<sub>2</sub> and H<sub>2</sub>O Splitting for Thermochemical Production of Solar Fuels Using Nonstoichiometric Ceria and Ceria/Zirconia Solid Solutions*, Alex Le Gal, Stéphane Abanades, Gilles Flamant, Energy & Fuels 25, 4836-4845, 2011.
- [42] *Dopant Incorporation in Ceria for Enhanced Water-Splitting Activity during Solar Thermochemical Hydrogen Generation*, Alex Le Gal, Stéphan Abanades, The Journal of Physical Chemistry C 116, 13516-13523, 2012.
- [43] *Experimental solar water thermolysis*, S.Z.Baykara, International Journal of Hydrogen Energy 29,1459-1469, 2004.
- [44] *Solar thermochemical splitting of CO<sub>2</sub> into separate streams of CO and O<sub>2</sub> with high selectivity, stability, conversion, and efficiency*, Daniel Marxer, Philipp Furler, Michael Takacs, Aldo Steinfeld, Energy & Environmental Science, 2017.
- [45] *CO<sub>2</sub> Splitting via Two-Step Solar Thermochemical Cycles with Zn/ZnO and FeO/Fe<sub>3</sub>O<sub>4</sub> Redox Reactions: Thermodynamic Analysis*, M.E. Gálvez, P.G. Loutzenhiser, I. Hischer, A. Steinfeld, Energy & Fuels 22, 3544-3550, 2008.
- [46] *Ceria as a Thermochemical Reaction Medium for Selectively Generating Syngas or Methane from H<sub>2</sub>O and CO<sub>2</sub>*, W.C. Chueh, S.M. Haile, ChemSusChem 2, 735-739, 2009.
- [47] Data sheet of the thermogravimetric analyzer STA 2500 Regulus by NETZSCH.

- [48] *Thermochemical CO<sub>2</sub> splitting via redox cycling of ceria reticulated foam structures with dual-scale porosities*, Philipp Furler, Jonathan Scheffe, Daniel Marxer, Michal Gorbar, Alexander Bonk, Ulrich Vogt, Aldo Steinfeld, Royal Society of Chemistry, Phys. Chem. Chem. Phys. 16, 10503-10511, 2014.
- [49] *Two-step water splitting thermochemical cycle based on iron oxide redox pair for solar hydrogen production*, Patrice Charvin, Stéphane Abanades, Gilles Flamant, Florent Lemort, Energy 32, 1124-1133, 2007.
- [50] *CO<sub>2</sub> valorisation based on Fe<sub>3</sub>O<sub>4</sub>/FeO thermochemical redox reactions using concentrated solar energy*, Stéphane Abanades, Isabel Villafan-Vidales, International Journal of Energy Research, 2012.
- [51] *Specific heat of nonstoichiometric ceria (CeO<sub>y</sub>)*, I. Riess, M. Ricken, J. Noeltling, Solid State Ionics 18 & 19, 725-726, 1986.
- [52] Use and maintenance manual of the solar dish concentrator (manuale di uso e manutenzione del concentratore solare a disco), El.Ma. srl Electronic Machining.
- [53] *Solar electricity via an Air Brayton cycle with an integrated two-step thermochemical cycle for heat storage based on Fe<sub>2</sub>O<sub>3</sub>/Fe<sub>3</sub>O<sub>4</sub> redox reactions: Thermodynamic and kinetic analyses*, H. Evan Bush, Peter G. Loutzenhiser, Solar Energy 174, 617-627, 2018.
- [54] *Reactivity assessment and oxidation kinetic model for CO<sub>2</sub> splitting on Fe-based oxygen carrier*, Azharuddin E. Farooqui, Massimo Santarelli, Jordi Llorca, 2019.
- [55] *Mechanical and physical properties of engineering alumina ceramics*, Pertti Auerkari, Technical Research Center of Finland, 1996.
- [56] COMSOL Multiphysics® 5.4 CFD Module User's Guide.
- [57] COMSOL Multiphysics® 5.4 Heat Transfer Module User's Guide.
- [58] *The properties of gases and liquids*, fifth edition, Bruce E. Poling, John M. Prausnitz, John P. O'Connell, McGRAW-HILL, 2000.
- [59] *Convection heat transfer*, Adrian Bejan, fourth edition, Wiley, 2013.